

University of Windsor

Scholarship at UWindor

Electronic Theses and Dissertations

Theses, Dissertations, and Major Papers

7-7-2020

Modeling the Flow and Heat Transfer in U-bend and Coaxial Borehole Heat Exchangers

Hani Pakoohinejad
University of Windsor

Follow this and additional works at: <https://scholar.uwindsor.ca/etd>

Recommended Citation

Pakoohinejad, Hani, "Modeling the Flow and Heat Transfer in U-bend and Coaxial Borehole Heat Exchangers" (2020). *Electronic Theses and Dissertations*. 8385.
<https://scholar.uwindsor.ca/etd/8385>

This online database contains the full-text of PhD dissertations and Masters' theses of University of Windsor students from 1954 forward. These documents are made available for personal study and research purposes only, in accordance with the Canadian Copyright Act and the Creative Commons license—CC BY-NC-ND (Attribution, Non-Commercial, No Derivative Works). Under this license, works must always be attributed to the copyright holder (original author), cannot be used for any commercial purposes, and may not be altered. Any other use would require the permission of the copyright holder. Students may inquire about withdrawing their dissertation and/or thesis from this database. For additional inquiries, please contact the repository administrator via email (scholarship@uwindsor.ca) or by telephone at 519-253-3000ext. 3208.

**Modeling the Flow and Heat Transfer in U-bend and Coaxial Borehole Heat
Exchangers**

By

Hani Pakoohinejad

A Thesis

Submitted to the Faculty of Graduate Studies
through the Department of Mechanical, Automotive and Materials Engineering
in Partial Fulfillment of the Requirements for
the Degree of Master of Applied Science
at the University of Windsor

Windsor, Ontario, Canada

2020

© 2020 Hani Pakoohinejad

**Modeling the Flow and Heat Transfer in U-bend and Coaxial Borehole Heat
Exchangers**

by

Hani Pakoohinejad

APPROVED BY:

M. Khalid

Department of Electrical and Computer Engineering

J. Defoe

Department of Mechanical, Automotive and Materials Engineering

T. Bolisetti, Co-Advisor

Department of Civil and Environmental Engineering

D. Ting, Co-Advisor

Department of Mechanical, Automotive and Materials Engineering

May 4, 2020

DECLARATION OF CO-AUTHORSHIP/PREVIOUS PUBLICATIONS

I hereby declare that this thesis incorporates material that is result of joint research, as follows:

This thesis studies the flow and heat transfer of U-bend and coaxial borehole heat exchangers that was made possible through a joint research project with Dr. Stanley Reitsma under the supervision of Dr. Tirupatti Bolisetti and Dr. David S-K. Ting. In all cases, the key ideas, primary contributions, experimental designs, data analysis, interpretation, and writing were performed by the author, and the contribution of co-authors was primarily through the provision of data analysis.

I am aware of the University of Windsor Senate Policy on Authorship and I certify that I have properly acknowledged the contribution of other researchers to my thesis, and have obtained written permission from each of the co-author(s) to include the above material(s) in my thesis.

I certify that, with the above qualification, this thesis, and the research to which it refers, is the product of my own work.

This thesis includes three original papers that have been previously published/submitted for publication in peer reviewed journals, as follows:

Thesis Chapter	Publication title/full citation	Publication status*
Chapter 2	Pakoohinejad, H., Bolisetti, T., Reitsma, S., and Ting, D. S-K., Impact of U-bend Curvature Ratio on the Flow and Heat Transfer	To be submitted
Chapter 3	Pakoohinejad, H., Bolisetti, T., Reitsma, S., and Ting, D. S-K., The effects of center-in versus annulus-in flow, inner pipe length, and Reynolds number on the performance of a coaxial heat exchanger	To be submitted

I certify that I have obtained a written permission from the copyright owner(s) to include the above published material(s) in my thesis. I certify that the above material describes work completed during my registration as a graduate student at the University of Windsor.

I declare that, to the best of my knowledge, my thesis does not infringe upon anyone's copyright nor violate any proprietary rights and that any ideas, techniques, quotations, or any other material from the work of other people included in my thesis, published or otherwise, are fully acknowledged in accordance with the standard referencing practices. Furthermore, to the extent that I have included copyrighted material that surpasses the bounds of fair dealing within the meaning of the Canada Copyright Act, I certify that I have obtained a written permission from the copyright owner(s) to include such material(s) in my thesis.

I declare that this is a true copy of my thesis, including any final revisions, as approved by my thesis committee and the Graduate Studies office, and that this thesis has not been submitted for a higher degree to any other University or Institution.

ABSTRACT

The numerical simulation of flow and heat transfer in U-bend and coaxial borehole heat exchangers is carried out using the OpenFOAM CFD solver and post-processed with ParaView. The purpose of this study was to find the minimum pressure loss coefficient with a high total heat transfer. Detailed flow structures and heat transfer characteristics were investigated in three U-bends at Reynolds number of 600 (Dean numbers of 190, 300, 425) and 6×10^4 (Dean number of 1.9×10^4 , 3×10^4 , 4.25×10^4) representing low and high Reynolds numbers. For the flow at $Re = 600$, the increase of Dean number due to the increase of curvature ratio results in a consistent decrease of total pressure loss coefficient up to 9%. At $Re = 6 \times 10^4$, Dean number of 3×10^4 has the minimum total pressure loss coefficient up to 6.9% of drop. The flow at a low Reynolds number has nearly 16 times better total heat transfer due to a higher residence time compared with a high Reynolds number at the exact same Dean number. However, this betterment of heat transfer happens at the cost of 5.8 times higher total pressure loss coefficient. In the coaxial model, the effects of Reynolds numbers of 2×10^3 , 1×10^4 and 2×10^4 show that the increment of Reynolds number reduces the total pressure loss of the system and increases the total heat transfer. At $Re = 2 \times 10^4$, a short ($X/D_h = 0.6$) and a long ($X/D_h = 1.6$) bucket space, a space between the inner pipe and the bottom of the borehole, require a large pumping power due to the increase of the total pressure loss coefficient. Also, no significant improvement in the total heat transfer is achieved as a result of changing the length of the bucket space. Hence, the length of $X/D_h = 1$ provides the most efficient pumping power. This length brings about a minimum total pressure loss up to 15%, meaning that installing the center pipe in a position that causes the least total pressure loss needs to be taken into account. At the Reynolds number of 2×10^4 , also, it was found that the center-in flow provides 5.7% better heat transfer performance with a significance of lower total pressure loss coefficient than the case of annulus-in flow.

DEDICATION

I dedicate this work:

To my family for their sincere love and confidence throughout this endeavour.

In memory of my sweet friends Hamidreza Setareh Kokab, Dr. Samira Bashiri, Zahra Naghibi, Mohammad Abbaspour Ghadi, and Pedram Jadidi who lost their lives in the flight PS752 crash.

ACKNOWLEDGEMENTS

I would like to acknowledge both of my Co-Advisors, Dr. David S.-K. Ting and Dr. Tirupati Bolisetti for their patience, guidance, and wisdom. I have received a great deal of assistance from them. I would like to thank the Turbulence and Energy Lab and all of its students and associates. I acknowledge Dr. Stanley Reitsma and GeoSource Energy Inc. for their support. I thank the support provided by Ontario Centre for Excellence. I also thank Springer, Journal of Experiments in Fluids for the copyright permission.

I would also like to thank my committee members, Dr. Jeff Defoe and Dr. Mohammed Khalid for offering their invaluable expertise on my research.

TABLE OF CONTENTS

DECLARATION OF CO-AUTHORSHIP/PREVIOUS PUBLICATIONS	iii
ABSTRACT.....	v
DEDICATION	vi
ACKNOWLEDGEMENTS	vii
LIST OF TABLES	xi
LIST OF ABBREVIATIONS/SYMBOLS.....	xv
NOMENCLATURE	xvi
CHAPTER 1 – Introduction	1
1.1 Background Information.....	1
1.2 Objectives	1
1.3 Scope of Work	2
1.4 Organization of Thesis.....	2
1.5 References.....	3
CHAPTER 2 - Impact of U-bend Curvature Ratio on the Flow and Heat Flux.....	4
2.1 Introduction.....	4
2.2 Fundamental Concept of Flow in Curved Ducts.....	6
2.3 Numerical Model	7
2.3.1 Model Setup for the Curvature Ratio Effect	7
2.3.2 Governing Equations	9
2.3.3 Boundary Conditions	11
2.4 Validation.....	13
2.5 Results.....	14
2.5.1 Distribution of pressure at $Re = 600$	15
2.5.2 Distribution of pressure at $Re = 6 \times 10^4$	16
2.5.3 Total pressure loss.....	18
2.5.4 Velocity and Dean cell development	19
2.5.5 Vorticity	28

2.5.6 Turbulent Kinetic Energy.....	31
2.5.7 Dean cell development at $Re = 600$	32
2.5.8 Dean cell development at $Re = 6 \times 10^4$	35
2.5.9 Friction distribution	37
2.5.10 Nusselt number and the total heat transfer	40
2.5.11 Reynolds number effects.....	43
2.5.12 U-bend Length	45
2.6 Conclusions.....	46
2.7 References.....	48
 CHAPTER 3 – The effects of center-in versus annulus-in flow, inner pipe length, and Reynolds number on the performance of a coaxial heat exchanger	 51
3.1 Introduction.....	51
3.2 Coaxial Heat Exchanger Model	52
3.3 Numerical Simulation	52
3.3.1 Governing Equations	54
3.3.2 Boundary Conditions	55
3.3.3 Model Domain	57
3.3.4 Model Verification and Validation	57
3.4 Results.....	58
3.4.1 Center-in vs. Annulus-in Flow Directions	58
3.4.2 Bucket space length	68
3.4.3 Reynolds number effects.....	72
3.5 Conclusions.....	76
3.6 References.....	77
 CHAPTER 4 – Conclusions and Future Work	 78
4.1 U-bend borehole heat exchangers:	78
4.2 Coaxial borehole heat exchanger	79
4.3 Future Work.....	80
 APPENDICES	 81
Appendix A.....	81

VITA AUCTORIS	82
----------------------------	-----------

LIST OF TABLES

Table 2.1 Dean and turbulence parameters	9
Table 2.2 Input parameters	9
Table 2.3 Initial and boundary condition parameters type.....	12
Table 2.4 Turbulent parameters	12
Table 2.5 Model conditions of the U-bend based on the change in Reynolds number	43
Table 2.6 U-bend length conditions	45
Table 3.1 Input parameters of the hydrodynamic simulation tests	56
Table 3.2 Initial and boundary conditions parameters	56
Table 3.3 Initial conditions for Realizable k- ω	57

LIST OF FIGURES

CHAPTER 2

Fig. 2.1 Forces contributing to the generation of secondary flow at each cross section of the bend at a specific Reynolds and Dean number	6
Fig. 2.2 Schematic diagram of U-bends with three curvature ratios and downstream	8
Fig. 2.3 Schematic diagram of the fluid domain at $\delta = 0.25$	8
Fig. 2.4 Grid system of the cross section of the computational domain including fluid and pipe.....	8
Fig. 2.5 Pressure coefficient at $\delta = 0.25$ and $Re = 6 \times 10^4$ against mesh sizing at $Z/D = 17.6$ as the reference point	13
Fig. 2.6 Comparison of the experimental (Sudo et al. 2000) and numerical pressure coefficients, $C_p = (p - p_{ref}) / \frac{1}{2} \rho U_{in}^2$, at $Re = 6 \times 10^4$	14
Fig. 2.7 Non-dimensional velocity of the simulated flow by OpenFOAM compared to the experimental test results for $Re = 6 \times 10^4$. [(b) is reprinted with permission from (Sudo et al. 2000), Copyright 2000 by Springer]	14
Fig. 2.8 Pressure coefficient of flow at $Re = 600$ inside the bend with (a) the curvature ratio of 0.1, (b) the curvature ratio of 0.25, and (c) the curvature ratio of 0.5	16
Fig. 2.9 Pressure coefficient of flow at $Re = 6 \times 10^4$ with (a) the curvature ratio of 0.1 and (b) curvature ratio of 0.25, and (c) the curvature ratio of 0.5.	17
Fig. 2.10 Total pressure loss of the U-bend system with the flow at (a) $Re = 6 \times 10^4$ and the flow at (b) $Re = 600$	18
Fig. 2.11 Velocity distribution of flow at $Re = 600$ along the bends with the curvature ratios of 0.1, 0.25, and 0.5 and downstream.....	21
Fig. 2.12 Velocity contours for $Re = 600$ & $De = 190$ ($\delta = 0.1$) at different cross sections. The left hand side of each cross-section is the inner wall and the right hand side is the outer wall of the secondary flow	22
Fig. 2.13 Velocity contours for $Re = 600$ & $De = 425$ ($\delta = 0.25$) at different cross sections. The left hand side of each cross-section is the inner wall and the right hand side is the outer wall of the secondary flow	22
Fig. 2.14 Velocity contours for $Re = 600$ & $De = 425$ ($\delta = 0.5$) at different cross sections. The left hand side of each cross-section is the inner wall and the right hand side is the outer wall of the secondary flow	23
Fig. 2.15 Velocity distribution of flow at $Re = 6 \times 10^4$ along the pipe bends with the curvature ratios of 0.1, 0.25, and 0.1 and downstream. The left hand side is the inner wall and the right hand side is the outer wall.	25
Fig. 2.16 Velocity contours of flow at $Re = 6 \times 10^4$ & $De = 425$ ($\delta = 0.10$) at different cross sections. The left hand side of each cross-section is the inner wall and the right hand side is the outer wall of the secondary flow.....	26
Fig. 2.17 Velocity contours of flow at $Re = 6 \times 10^4$ & $De = 425$ ($\delta = 0.25$) at different cross sections. The left hand side of each cross-section is the inner wall and the right hand side is the outer wall of the secondary flow.....	26

Fig. 2.18 Velocity contours of flow at $Re = 6 \times 10^4$ and $De = 425$ ($\delta = 0.5$) at different cross sections The left hand side of each cross-section is the inner wall and the right hand side is the outer wall of the secondary flow	27
Fig. 2.19 Dimensionless vorticity contours, streamlines, and vector lines of flow at $Re = 600$ for the curvature ratios of 0.1, 0.25, and 0.5	30
Fig. 2.20 Vorticity contours, streamlines, and vector lines of flow at $Re = 6 \times 10^4$ for the curvature ratios of 0.1, 0.25, and 0.5	31
Fig. 2.21 Turbulent kinetic energy of flow at $Re = 6 \times 10^4$ with the curvature ratio of (a) $\delta = 0.5$, (b) $\delta = 0.25$, and (c) $\delta = 0.1$	32
Fig. 2.22 Streamlines of flow at $Re = 600$ along the bend and downstream with the curvature ratio of 0.5	34
Fig. 2.23 Streamlines of flow at $Re = 600$ along the bend and downstream with the curvature ratio of 0.25	35
Fig. 2.24 Streamlines of flow at $Re = 600$ along the bend and downstream with the curvature ratio of 0.1	35
Fig. 2.25 Streamlines of flow at $Re = 6 \times 10^4$ along the bend and downstream with the curvature ratio of 0.5	36
Fig. 2.26 Streamlines of flow at $Re = 6 \times 10^4$ along the bend and downstream with the curvature ratio of 0.1	37
Fig. 2.27 Streamlines of flow at $Re = 6 \times 10^4$ along the bend and downstream with the curvature ratio of 0.1	37
Fig. 2. 28 Comparison of friction coefficient of flow at $Re = 6 \times 10^4$ with the curvature ratios of 0.1, 0.25, and 0.5 along the bend and downstream	38
Fig. 2. 29 Friction coefficient of flow at $Re = 600$ with the curvature ratios of 0.1, 0.25, and 0.5 along the bend and downstream	39
Fig. 2. 30 Friction coefficient of flow at $Re = 6 \times 10^4$ with the curvature ratios of 0.1, 0.25, and 0.5 along the bend and downstream	40
Fig. 2.31 Nusselt number of (a) the flow at $Re = 6 \times 10^4$ and (b) the flow at $Re = 600$ in the bend outer wall and inner wall	41
Fig. 2.32 Total heat transfer of flow at (a) $Re = 6 \times 10^4$ and (b) $Re = 600$ inside of the running fluid	42
Fig. 2.33 The outlet temperature with the variation of Reynolds number	44
Fig. 2.34 Cooling rate and the temperature in the outlet with the variation of Reynolds number	44
Fig. 2.35 Outlet temperature with the variation of Reynolds number	46

CHAPTER 3

Fig. 3.1 Schematic diagram of coaxial heat exchanger, cross sectional view	52
Fig. 3.2 Wedge of the computational grid in axisymmetric plane	53
Fig. 3.3 Temperature against mesh sizing	58
Fig. 3.4 (a) Pressure drop of center-in and annulus-in flows in the inner pipe and the annulus and (b) Total pressure loss coefficient of center-in and annulus-in flows between the inlet and outlet	59

Fig. 3.5 Pressure coefficient ($C_p = p - p_{in} / \frac{1}{2} \rho U_{in}^2$) of the center-in and annulus-in flow models against end cap walls ($Y^* = Y/D_{io}$).....	60
Fig. 3.6 The pressure contours of the center-in and the annulus-in flow at the bottom of the borehole demonstrated in a dimensionless form ($\Delta P / \frac{1}{2} \rho U_{in}^2$).....	61
Fig. 3.7 Dimensionless local pressure gradient contours of the center-in and the annulus-in flow at the bottom of the borehole with respect to the inlet pressure gradient.	61
Fig. 3.8 Pipe wall heat flux against the end cap surface ($Y^* = Y/D_{io}$).....	62
Fig. 3.9 (a) Averaged Heat flux along the pipe and the end cap surfaces for the center-in and annulus-in flow directions. And (b) Total heat flux for the center-in and annulus-in flow directions	63
Fig. 3.10 Total heat transfer in the cases of center-in and annulus-in dimensionless by the inlet enthalpy	63
Fig. 3.11 Nusselt number of the center-in and annulus-in flow (a) on the flat-end cap ($Y^* = Y/D_{io}$) and (b) along the pipe ($X^* = X / X_{max}$)	65
Fig. 3.12 Friction coefficient of center-in and annulus-in flows on the end cap surface ($Y^* = Y/D_{io}$).....	66
Fig. 3.13 Velocity distribution of center-in and annulus-in flow directions at the bottom of the coaxial pipes with flat-end and curved-end caps.	67
Fig. 3.14 Flow streamlines at the bottom of the coaxial BHEs for flat end caps in center-in and annulus-in flow directions.....	67
Fig. 3.15 Normalized vorticity contours of center-in and annulus-in flow directions	68
Fig. 3.16 Turbulent kinetic energy distribution contours of center-in and annulus-in flow directions	68
Fig. 3.17 Schematic diagram of the inner pipe in relation to the bottom of the CBHE (bucket space).....	69
Fig. 3.18 Dimensionless total pressure loss in the coaxial system based on change in the bucket space length.....	70
Fig. 3.19 Wall friction coefficient on the end cap surface ($Y^* = Y/D_{io}$) based on the change in the bucket space length.....	71
Fig. 3.20 Nusselt number against the end cap ($Y^* = Y/D_{io}$) based on the change in the bucket space length	71
Fig. 3.21 Pressure coefficient on the end cap surface ($Y^* = Y/D_{io}$) based on the change in the bucket space length.....	71
Fig. 3.22 Heat flux along (a) the annulus wall and (b) end cap surface ($Y^* = Y/D_{io}$)	73
Fig. 3.23 enthalpy (a) along the pipe ($X^*=X/X_{max}$) and (b) end cap surface ($Y^*=Y/D_{io}$)...	73
Fig. 3.24 Nusselt number along (a) the annulus wall and (b) end cap surface ($Y^*=Y/D_{io}$)	73
Fig. 3.25 Friction coefficient along (a) the annulus wall and (b) the end cap surface	74
Fig. 3.26 Pressure coefficient of three Reynolds numbers against the wall ($X^* = L/D_h$) along the annulus	75
Fig. 3.27 Pressure drop coefficient in the inner pipes and the outer pipes considering three Reynolds numbers.	75
Fig. 3.28 Total pressure loss of the system considering three Reynolds numbers.....	75

LIST OF ABBREVIATIONS/SYMBOLS

BHE	Borehole Heat Exchanger
CBHE	Coaxial Borehole Heat Exchanger
ICW	Inner Curvature Wall
RANS	Reynolds Averaged Navier Stokes

NOMENCLATURE

Symbols

A	Cross sectional area, [m]	S_ε	Dissipation rate source term
C_f	Friction coefficient	T	Temperature, [K]
C_p	Pressure coefficient	U	Velocity, [m · s ⁻¹]
C_μ	Eddy viscosity constant	u'	Root mean square of the velocity fluctuations [m · s ⁻¹]
D	Diameter, [m]	u_{avg}	Mean flow velocity [m · s ⁻¹]
D_e	Dean number		Contribution of the fluctuating dilatation in compressible turbulence to the overall dissipation rate
D_h	Hydraulic diameter, [m]	Y_M	Longitudinal distance along upstream, [m]
G_b	Generation of turbulent kinetic energy due to buoyancy, [J · kg ⁻¹]	Z'	Longitudinal distance along downstream, [m]
G_k	Generation of turbulent kinetic energy due to mean velocity, [J · kg ⁻¹]		
g	Gravitational acceleration, [m · s ⁻¹]		
h	enthalpy		
h_c	Convective heat transfer coefficient [W · m ⁻² · K]		
I	Turbulence intensity		
k	Turbulent kinetic energy, [m ² · s ⁻²]		
l	Turbulence length scale, [m]		
Nu	Nusselt number		
P	Pressure, [Pa]		
P	Internal wetted perimeter, [m]		
R	Radius, [m]		
Re	Reynolds number		
R_c	Radius of curvature [m]		
S_k	Turbulence kinetic energy source term, [J · kg ⁻¹]		

Greek Symbols

δ	Curvature ratio (hydraulic radius/radius of curvature)
ε	Dissipation rate, [m ² · s ⁻³]
θ	Circumferential angle [°]
θ'	Dimensionless outlet temperature
λ	Thermal conductivity, [W · K ⁻¹ · m ⁻¹]
μ	Dynamic viscosity, [Pa · s]
μ_t	Eddy viscosity, [Pa · s]
ν	Kinematic viscosity [m ² · s]
ρ	Fluid density, [kg · m ⁻³]
ϑ	Vector field of the flow velocity
φ	Bend angle [°]

CHAPTER 1 – Introduction

1.1 Background Information

Renewable energy is used to mitigate environmental damages and enhance the accessibility, affordability, security, and the efficiency of the energy use and consumption (Shortall et al. 2015). As a promising renewable energy source, a lot of measures are underway to spur the geothermal energy. Geothermal energy is considered to be a cost effective, reliable, and an environmentally friendly energy source (Alanne and Saari 2006). This underground energy source is harvested conventionally via U-bend borehole heat exchangers. More recently, however, coaxial borehole heat exchangers have been used as an alternative system because they bear the potential of minimizing the borehole thermal resistance (Yavuzturk and Chiasson 2002, and Zarrella et al. 2017) and provide a better thermal performance with their larger heat exchange area (Song et al. 2018 and Holmberg et al. 2016), making a feasible alternative upgrade to the conventional U-bend systems (Raghavan 2016).

1.2 Objectives

This study aims at investigating the performance of U-bend and Coaxial heat exchangers through understanding the following items:

U-bend:

- The impact of the bend curvature for the purpose of reducing the total pressure loss and increasing the heat transfer of flow at the Reynolds number of $Re = 6 \times 10^4$ (Dean numbers of $De = 1.9 \times 10^4, 3 \times 10^4, 4.25 \times 10^4$) and 600 ($De = 190, 300, 425$).
- The effect of variation of Reynolds numbers from $Re = 1 \times 10^4, 2 \times 10^4, 3 \times 10^4, 4 \times 10^4, 5 \times 10^4$, and 6×10^4 , and pipe length ($L = 38.5D, 67.3D$, and $96.2D$) on the outlet temperature.

Coaxial:

- The effects of center-in and annulus-in flow in terms of a lower total pressure loss and higher heat transfer performance.

- The impact of the bucket space, the space between the end of the inner pipe and the borehole end cap, at the Reynolds number of 2×10^4 on the total pressure loss and heat transfer.
- The impacts of Reynolds number of 2×10^3 , 1×10^4 , 2×10^4 on the total pressure loss and heat transfer.

1.3 Scope of Work

This research delves into U-bend and coaxial borehole heat exchangers at a lab scale length. Both U-bend and coaxial models are validated against the experimental tests. In this work, there is a comparative study of flow and heat transfer at $Re = 6 \times 10^4$ and $Re = 600$ with three Dean numbers for each flow due to the three curvature radii (ratio of hydraulic radius to the radius of curvature) of $\delta = 0.1$, 0.25 , and 0.5 for the U-bends to enhance the heat transfer performance and minimize the total pressure losses as no studies regarding curvature ratio impacts on U-bends were found in the literature. Also, in the coaxial model, the center-in and the annulus-in flows, the bucket length at the bottom of the Coaxial Borehole Heat Exchanger known as CBHE, and the impacts of flow and heat transfer at three Reynolds numbers of 2×10^3 , 1×10^4 , and 2×10^4 are studied.

1.4 Organization of Thesis

Following the introduction, the second chapter of this thesis focuses on the flow in a U-bend borehole heat exchanger, conducting the verification and validation procedure, and elucidating the vortical structures and some flow parameters when each of the flow types travels inside the bend. It also delves into the concepts underlying the effect of curvature ratio and how it impacts the total pressure loss and heat transfer. Then two parameters including the change in Reynolds numbers, and the length of the U-bend system on the amount temperature in the outlet of the U-bend system is focused.

The third chapter of this thesis provides a preliminary study with regards to coaxial BHE, trying to find an efficient center-in or annulus-in flow direction, the bucket space lengths, and Reynolds number in terms of lower total pressure loss and higher heat transfer.

1.5 References

- Alanne, K., and A. Saari. 2006. "Distributed Energy Generation and Sustainable Development." *Renewable and Sustainable Energy Reviews* 10(6): 539–58.
- Holmberg, H., J. Acuña, E. Næss, and O. K. Sønju. 2016. "Thermal Evaluation of Coaxial Deep Borehole Heat Exchangers." *Renewable Energy* 97: 65–76.
- Raghavan, N. 2016. "Numerical and Experimental Design of Coaxial Shallow Geothermal Energy Systems."
- Shortall, R., B. Davidsdottir, and G. Axelsson. 2015. "Geothermal Energy for Sustainable Development: A Review of Sustainability Impacts and Assessment Frameworks." *Renewable and Sustainable Energy Reviews* 44: 391–406.
- Song, X., G., Wang, Y., Shi, R., Li, Zh., Xu, R., Zheng, Y., Wang, J., Li. 2018. "Numerical Analysis of Heat Extraction Performance of a Deep Coaxial Borehole Heat Exchanger Geothermal System." *Energy* 164: 1298–1310.
- Yavuzturk, C., and A. D. Chiasson. 2002. "Performance Analysis of U-Tube, Concentric Tube, and Standing Column Well Ground Heat Exchangers Using a System Simulation Approach." *ASHRAE Transactions; Atlanta* 108: 925.
- Zarrella, A., G. Emmi, and M. De Carli. 2017. "A Simulation-Based Analysis of Variable Flow Pumping in Ground Source Heat Pump Systems with Different Types of Borehole Heat Exchangers: A Case Study." *Energy Conversion and Management* 131: 135–50.

CHAPTER 2 - Impact of U-bend Curvature Ratio on the Flow and Heat Transfer

2.1 Introduction

Geothermal energy is a renewable and sustainable energy source (Younis et al. 2010), which is yet to be fully exploited for mitigating climate change. Noting its promise, significant advances in low-temperature geothermal borehole heat exchangers have been made recently, however, there is still a lack of a complete understanding of the underlying fluid flow and heat transfer (Lyu et al. 2017 and Beier et al. 2014). U-bend heat exchangers have been the most common elements in the ground source heat pump systems.

The study of U-bend borehole heat exchangers covers many areas, from thermal response (Maestre et al. 2015), heat extraction performance of different downhole heat exchangers (Song et al. 2017), to providing an estimation for a short and long term periods of operation (Biglarian, et al. 2017). Kalpakli, et al. (2016) reviewed the turbulent flows in curved pipes from their historical perspective to the most recent advances regardless of their applications. The review by Javadi et al. (2019), however, focused on the performance of ground heat exchangers considering the geometry, pipe material, fluid carrier, and the subjects associated with ground heat exchanger's depth and its effects on the flow and heat transfer. Kummert et al. (2007) mainly focused on the geothermal heat pump systems and how much heat pumps impact the required length of the geothermal heat exchanger. They found that absorption heat pump systems require a shorter borehole length than the compression heat pump systems, and the required borehole length varies depending on geological locations. Chung and Choi (2012) studied the heat pump unit with the flow rate change, and concluded that the heat transfer rate per unit length also increases with the increase in flow rate.

Noorani et al. (2013) conducted a direct numerical simulation in one straight and two curved pipes. They demonstrated the effects of curvature ratio and Reynolds number on shear stress and Dean vortices. For the laminar forced convection, Choi and Zhang (2012) it was found that the averaged Nusselt number is enhanced with an increase in Reynolds and Prandtl numbers. Akbarinia (2008) also studied the nanofluids added to the running fluid inside a curved duct. It was found that the nano-fluid does not have a

noticeable effect on the secondary flow. It does, however, affect the axial velocity, Nusselt number, skin friction coefficient and the fluid temperature, in a way that the appearance of maximum axial velocity near the pipe wall, causes a decrease of temperature. Also, the Nusselt number and the skin friction increase as a result of increasing the buoyancy forces.

Sudo et al. (1998) carried out an experiment on a 90-degree pipe bend with a curvature ratio of 0.25 (the ratio of the hydraulic diameter and the radius of curvature) through which steady state turbulent air flows. They showed the flow development including the formation and evolution of Dean vortices. Their study has served as a reference for numerical verification for Dutta et al. (2016), who verified the curvature effect. Also, Kim et al. (2014) studied the flow of Sudo et al's 90-degree bend. The results showed that the intensity of the secondary eddies reaches their maximum value when the flow is at the bend exit and reduces to about 10% of the maximum value at 10D downstream of the bend exit.

Later, Sudo et al. (2000) performed their experiment on a 180-degree bend at otherwise the same flow conditions of their previous work. Based on this experimental work, Cvetkovski et al. (2015) performed a CFD study to show that, for the studied conditions, there is a decrease of heat transfer with an increase of Dean number. At a specific and low Reynolds number of $Re = 2000$, the Dean number increment reduces the wall flux in both the curved duct as well as the upstream and downstream. However, when increasing the Reynolds number, and at each specific Reynolds number, namely $Re = 5000$, the wall flux starts increasing in the curved duct with an increase of Dean number, although the upstream and downstream continue a reducing trend of wall flux at an enhanced Dean number. Also, Cvetkovski et al. (2014) numerically showed that a higher turbulence level associated with the increase in flow velocity does not significantly enhance the heat transfer; suggesting a balance between the turbulence level and resident time needed for heat transfer to materialize.

To minimize the costs associated with the installation and material, it is important to understand the effect of the bend curvature on the performance of the BHE system. This is the reason for selecting different curvature ratios that result in different borehole

diameters. The knowledge regarding the impact of curvature ratio provides an insight into enhancing the BHE performance at an efficient borehole diameter.

In the present paper, it is aimed to observe how the hydrodynamic and thermal parameters of flow are impacted by the curvature ratio variations in the U-bend with different curvature radii at the $Re = 600$ and $Re = 6 \times 10^4$. Finally, the effect of Reynolds numbers from $Re = 1 \times 10^4$ to 6×10^4 inside the U-bend system, and the pipe lengths of $L = 38.5D$, $67.3D$, and $96.2D$ (4m, 7m, and 10m), on the outlet temperature of the U-bend system is discussed.

2.2 Fundamental Concept of Flow in Curved Ducts

The phenomenon of flow in curved pipes, regardless of the bend angle or the pipe configuration, is that as the fluid travels in a curved duct, a secondary flow motion may be generated which makes up counter-rotating vortices. This curvature related phenomenon shown in Fig. 2.1, brings with it centrifugal forces due to the curve, and it is basically accompanied by a transverse pressure gradient and an increase in pressure inside the outer half of the bend (Kalpakli 2012) so as to balance the centrifugal force. Study of the Secondary flow in bend pipes traces back to the 1920s when Dean delineated the flow behavior inside curved pipes theoretically (Dean 1927 and Dean 1928). Dean theoretically showed the generation of vortical structures inside the bend. He used a perturbation procedure through passing Poiseuille flow from a straight to a curved pipe. Since then, this became an interesting subject for academic research.

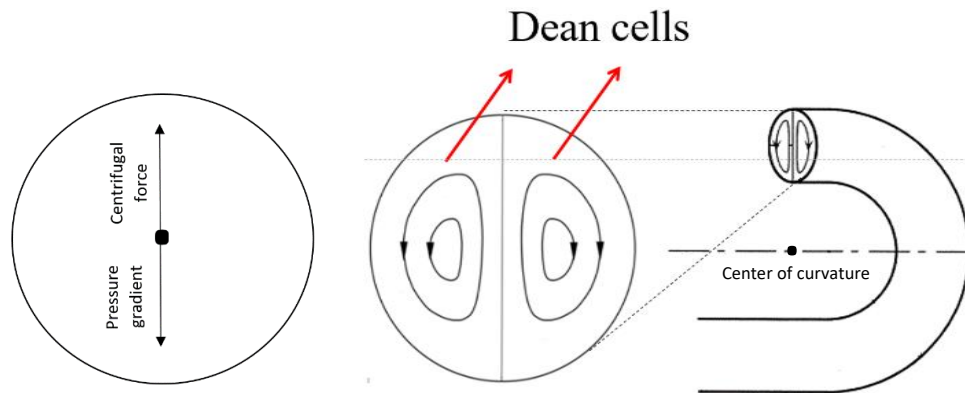


Fig. 2.1 Forces contributing to the generation of secondary flow at each cross section of the bend at a specific Reynolds and Dean number

2.3 Numerical Model

In a numerical simulation, the OpenFOAM v.5 has been used to solve the Reynolds-Averaged Navier-Stokes (RANS) equations of a steady incompressible flow running inside the U-bend. Comparing the results of the numerical simulation provides validation for the experimental test by Sudo et al. (2000). The convergence criteria of all governing equations are set as 10^{-6} . And the "semi-implicit method for pressure-linked equation" (SIMPLE) algorithms are used as the Navier-Stokes and energy equations solvers.

2.3.1 Model Setup for the Curvature Ratio Effect

Three 3D geometries were created with three curvature ratios (δ) as tabulated in Table 2.1. The schematic diagram of the three models is shown in Fig. 2.2, and the fluid dimensions shown in Fig. 2.3. As it is shown in this figure, all dimensions including upstream and downstream, radius of curvature, and diameters remain constant. The hydraulic diameter of the experimental test is $D = 104$ mm with the upstream and downstream length of $100D$ and $40D$, respectively (Sudo et al., 2000). The U-bend curvature radii are, 104mm, 208 mm, and 520mm. So this provides the curvature ratio of 0.5, 0.25, and 0.1 based on $\delta = \frac{D_h}{2R_c}$. Considering two Reynolds number of 600 and 6×10^4 and three curvature ratios of 0.5, 0.25, and 0.1, the simulations are conducted on six Dean numbers based on $De = Re \times \sqrt{\delta}$. The circulating fluid inside the U-bend is assumed to be steady during the simulations in accordance with the experimental test. Thermo-physical properties of the fluid carrier and the pipes are given in Table 2.2 as there is conjugate heat transfer. To verify the procedure, mesh independency test was carried out with an incremental mesh refinement. The fluid grid zones and the appropriateness of y^+ were checked in accordance with (Gao et al. 2018) grid system verification approach. Fig. 2.4 shows a cross sectional slice of the computational fluid domain that is biased toward the outer wall of the pipe with the pipe thickness of 0.23cm. Although the flow is symmetrical in the bend cross sections, the full domain of the pipe and fluid is simulated to observe if the flow is still symmetrical in the downstream.

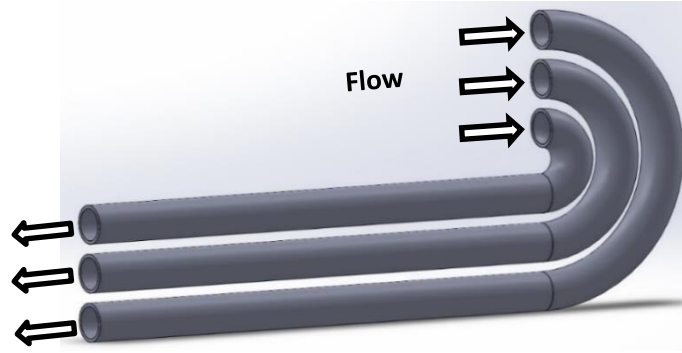


Fig. 2.2 Schematic diagram of U-bends with three curvature ratios and downstream

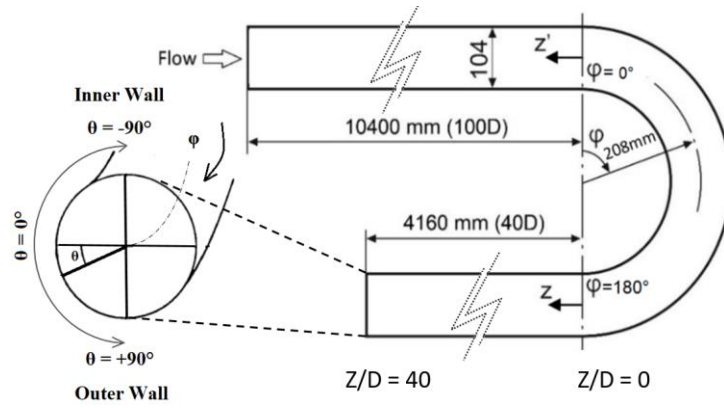


Fig. 2.3 Schematic diagram of the fluid domain at $\delta = 0.25$

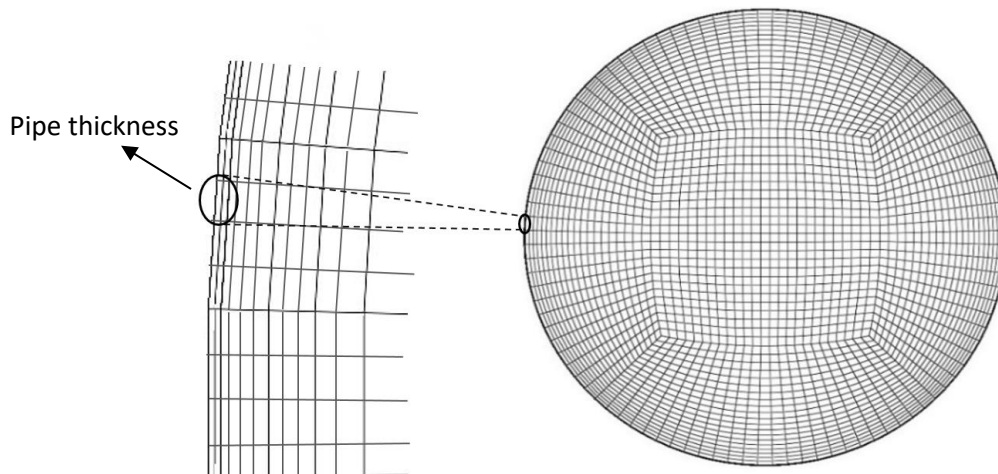


Fig. 2.4 Grid system of the cross section of the computational domain including fluid and pipe

Table 2.1 Dean and turbulence parameters

Pipe Diameter (mm)	Radius of Curvature (mm)	Curvature Ratio	Reynolds Number	Dean Number
104	520	0.10	6×10^4	1.9×10^4
	208	0.25		3×10^4
	104	0.50		4.25×10^4
	520	0.10	600	190
	208	0.25		300
	104	0.50		425

Table 2.2 Input parameters

Material	Density (kg/m ³)	Specific Heat (J/kg·K)	Thermal Conductivity (W/m·K)	Dynamic Viscosity (P)	Inlet Velocity (m/s)
Water	997.8	4076.4	0.60475	9.8×10^{-4}	5.7×10^{-1} 5.7×10^{-3}
HDPE	950	2500	0.33	-	-

2.3.2 Governing Equations

Mass Conservation

Mass conservation or continuity equation for a steady flow can be expressed as

$$\vec{\nabla} \cdot \vec{\vartheta} = 0 \quad (3.1)$$

where $\vec{\vartheta}$ is the velocity vector.

Momentum Conservation

The Navier-Stokes equations for the studied incompressible flow is

$$(\vec{\vartheta} \cdot \nabla) \vec{\vartheta} = -\frac{1}{\rho} \nabla p + \nabla \cdot (\nu \nabla \vec{\vartheta}) + \vec{g} \quad (3.2)$$

where p is the pressure, ν is the kinematic viscosity, and \vec{g} is the external body force (gravitational acceleration).

Energy Conservation

The energy equation for the fluid can be expressed as

$$\begin{aligned} \frac{\partial(\rho E)}{\partial t} + \frac{\partial(\rho \vartheta_i E)}{\partial x_i} &= \frac{\partial}{\partial x_j} \left(k_{eff} \frac{\partial T}{\partial x_j} + \vartheta_i (\tau_{ij})_{eff} \right) \\ (\tau_{ij})_{eff} &= \mu_{eff} \left(\frac{\partial u_j}{\partial x_i} + \frac{\partial u_i}{\partial x_j} \right) - \frac{2}{3} \mu_{eff} \frac{\partial u_k}{\partial x_k} \delta_{ij} \\ k_{eff} &= k + \frac{c_p \mu_t}{Pr_t} \end{aligned} \quad (3.3)$$

where E is the total transported energy, k_{eff} is the effective thermal conductivity, $(\tau_{ij})_{eff}$ is the deviatoric stress tensor, and T is the temperature.

The balance of energy for the pipe is expressed as

$$\nabla \cdot (k_s \cdot \nabla T_s) = 0 \quad (3.4)$$

where k_s is the thermal conductivity of the solid part, and T_s is the temperature of the solid part.

Transport Equations for the Realizable k- ε model

The transport equations for the realizable k- ε model as per (Ramadan 2016)

$$\frac{\partial}{\partial t} (\rho k) + \frac{\partial}{\partial x_j} (\rho k u_j) = \frac{\partial}{\partial x_j} \left[\left(\mu + \frac{\mu_t}{\sigma_k} \right) \frac{\partial k}{\partial x_j} \right] + G_k + G_b - \rho \varepsilon - Y_M + S_k \quad (3.5)$$

$$\frac{\partial}{\partial t} (\rho \varepsilon) + \frac{\partial}{\partial x_j} (\rho \varepsilon u_j) = \frac{\partial}{\partial x_j} \left[\left(\mu + \frac{\mu_t}{\sigma_\varepsilon} \right) \frac{\partial \varepsilon}{\partial x_j} \right] + \rho C_1 S \varepsilon - \rho C_2 \frac{\varepsilon^2}{k + \sqrt{\nu \varepsilon}} + C_{1\varepsilon} \frac{\varepsilon}{k} C_{3\varepsilon} G_b + S_\varepsilon \quad (3.6)$$

where G_k is the turbulence kinetic energy generation due to the mean velocity gradient, G_b is the turbulence kinetic energy generation due to buoyancy, Y_M is the fluctuating dilatation in compressible turbulence to the overall dissipation rate, S is the source term, and the

empirical values are C_1 equal to 1.44, C_2 equal to 1.9, σ_ε equal to 1.0, and σ_k is equal to 1.2.

2.3.3 Boundary Conditions

According to Table 2.3, the velocity in the inlet is fixedValue, which is a fixed value constraint. The velocity on the pipe-fluid interface is set to noSlip boundary condition which applies the fixedValue constraint of zero velocity, and it is zeroGradient at the outlet port. This boundary condition sets a zero-gradient of a specific parameter from the patch internal field to the patch faces. Also, OutletInlet boundary condition provides a generic inflow with the outflow when there is reverse flow. A specific wall function is set for each turbulent parameter in the fluid-pipe interfaces. Turbulence properties of Realizable k and ε (realizableKE) are calculated based on the following equations and Table 2.4. The reason for selecting realizable k- ε is because of the large and adverse gradients inside the bend, it also improves the performance of rotation, recirculation, and streamline curvature. To conjugate the heat transfer, the temperature of the pipe-fluid interface is set to Compressible::turbulentTemperatureCoupledBaffleMixed. The inlet temperature is 300 K and the temperature of the outer wall of the pipe is set to be constant and equal to 275 K. The flow is assumed to enter the pipe inlet at the velocity of 0.57m/s for the flow at $Re = 6 \times 10^4$, and 0.0057 m/s for the flow at $Re = 600$. The case considered is under the pipe-fluid type, the outlet patches are set to zeroGradient for the velocity, k, and ε , and the temperature.

Reynolds Number,

$$Re = \frac{\text{Inertia Forces}}{\text{Viscous Forces}} = \frac{\rho U D_h}{\mu} \quad (3.7)$$

where ρ is the density of the fluid, U is the velocity in the inlet, D_h is the pipe hydraulic diameter, and μ is the dynamic viscosity of the fluid.

The turbulent kinetic energy,

$$k = \frac{3}{2} (UI)^2 \quad (3.9)$$

where U is the velocity in the inlet, and I is the turbulent intensity that is set as 1% in the inlet.

The empirical constant used in for turbulent flow,

$$\varepsilon = (C_\mu)^{3/4} \frac{k^{3/2}}{l} \quad (3.10)$$

where $C_\mu \cong 0.009$. The turbulent length scale of the large energy eddies in the inlet is set as:

$$l = 0.5D_h \quad (3.11)$$

The turbulent viscosity,

$$\frac{\mu_t}{\mu} = (C_\mu)\rho \frac{k^2}{\mu\varepsilon} \quad (3.12)$$

Table 2.3 Initial and boundary condition parameters type

	inlet	outlet	pipe_fluid_interface	pipewall
U	fixedValue	zeroGradient	noSlip	-
p	zeroGradient	fixedValue	zeroGradient	-
T	fixedValue	OutletInlet	Compressible::turbulentTempera tureCoupledBaffleMixed	fixedValue
ε	fixedValue	zeroGradient	epsilonWallFunction	-
k	fixedValue	zeroGradient	kqRWallFunction	-

Table 2.4 Turbulent parameters

Reynolds	6×10^4
Turbulence Intensity (%)	1
Turbulent Kinetic Energy (m^2/s^2)	5×10^{-5}
Turbulent Dissipation (m^2/s^3)	5.9×10^{-6}
Turbulence Viscosity Ratio	9.8×10^{-7}
Turbulence Length Scale (m)	0.007

2.4 Validation

Fig. 2.5 shows the mesh independency graph from a coarse mesh to the optimum fine mesh. Considering the measured referenced pressure, it was observed that regardless of the Reynolds number, 3.0×10^6 , 3.6×10^6 , and 3.9×10^6 mesh elements are adequate in terms of solution convergence and accuracy and yet not overly computational expensive for the curvature ratios of 0.5, 0.25, and 0.1 respectively.

The validation of the numerical simulation is carried out by comparing the numerical results with the experimental test ($\delta = 0.25$). The wall pressures are plotted against the experimental data of Sudo et al. (2000) at five circumferential angles of $\theta = 0^\circ$, $\pm 45^\circ$, $\pm 90^\circ$, at various cross sections inside the bend and downstream. Fig. 2.6 shows the comparison of both numerical results and the experimental pressures of a referenced point in one diagram. The results show that the numerical pressure coefficients have the maximum of 3.7% deviation from the experimental values. Also, Fig. 2.7 shows the velocity distribution of flow through the U-bend pipe in contrast with Sudo's experimental test results. The simulation and the experimental test contours show a good compliance with the maximum deviation of 1%.

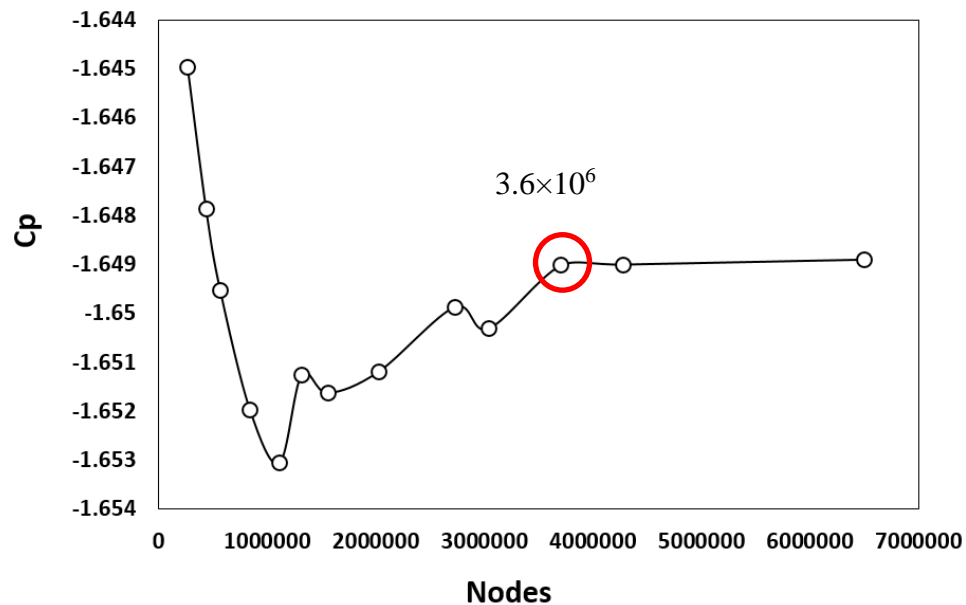


Fig. 2.5 Pressure coefficient at $\delta = 0.25$ and $Re = 6 \times 10^4$ against mesh sizing at $Z/D = 17.6$ as the reference point

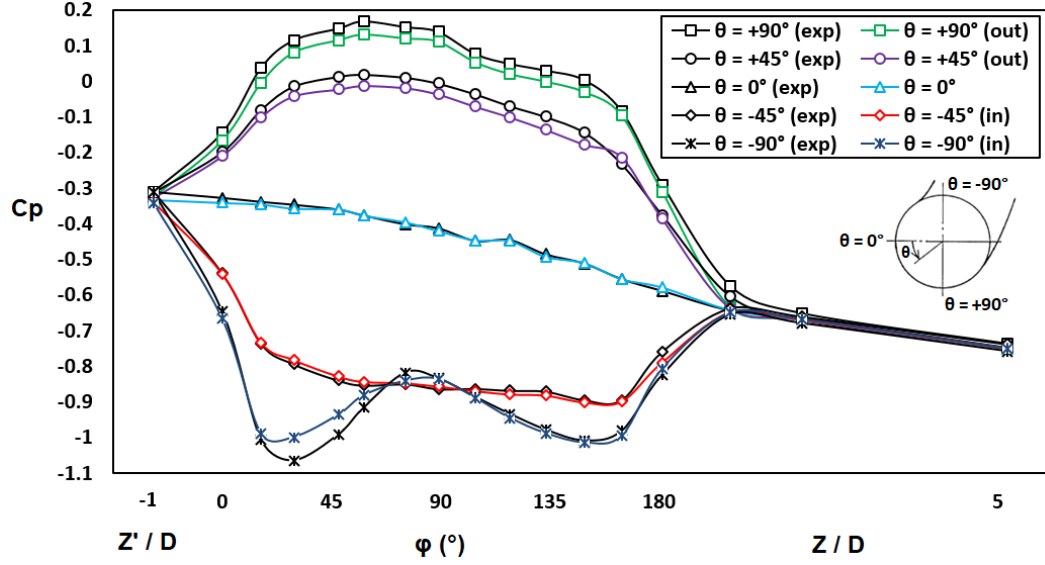


Fig. 2.6 Comparison of the experimental (Sudo et al. 2000) and numerical pressure coefficients, $C_p = \frac{p - p_{ref}}{\frac{1}{2}\rho U_0^2}$, at $Re = 6 \times 10^4$

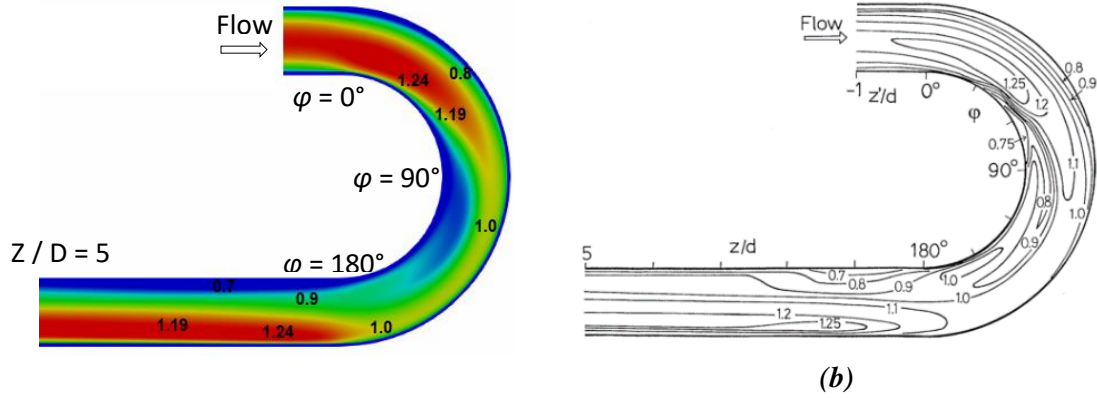


Fig. 2.7 Non-dimensional velocity of the simulated flow by OpenFOAM compared to the experimental test results for $Re = 6 \times 10^4$. [(b) is reprinted with permission from (Sudo et al. 2000), Copyright 2000 by Springer]

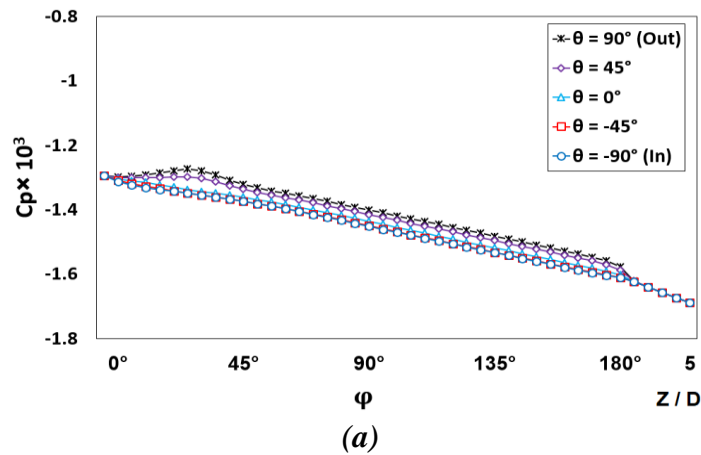
2.5 Results

The results concerning the change of Dean number due to the change in the curvature ratio shows that for the flow at $Re = 600$, there is a more varied pressure distribution with larger magnitudes and smaller total pressure loss when increasing the Dean number. This reduction of total pressure loss continues up to a point where further increase in curvature ratio does not reduce the amount of total pressure loss. However,

since the increase of Dean number causes a lower total pressure loss and lower heat transfer at the same time, when selecting the bend curvature ratio, a balance between Dean number and the total pressure loss based on the required heat transfer needs to be considered. For the flow at $Re = 6 \times 10^4$, among the three curvature ratios of 0.1, 0.25, and 0.5, it is found that although the heat transfer of the flow decreases with the increase of Dean number, the total pressure loss of the U-bend system with the curvature ratio of 0.25 is the lowest, which makes the bend curvature of 0.25 a better option for the U-bend system in terms of flow, because the lower total pressure loss coefficient contributes to a lower pumping power. However, these results need to be tied with heat transfer to have a better judgement about a proper bend curvature that is being studied later in this chapter.

2.5.1 Distribution of pressure at $Re = 600$

Fig. 2.8 shows the pressure distribution of flow at $Re = 600$ inside the U-bends of three Dean numbers. As the flow travels inside the bend, the pressure gradient is formed in the outward region of the bend (between the centerline and the outer wall) to balance the centrifugal force. Hence, the fluid is directed toward the outer side of the bend, creating a large pressure near and on the outer wall and a lower pressure on the inner wall. It is also observed that the variations of pressure distribution are enhanced at a higher Dean number due to an increase in the bend curvature ratio. When the flow enters the downstream, the slope of pressure drop of the three pipes has equal trends, but they have different values because they are affected by different curvature ratios.



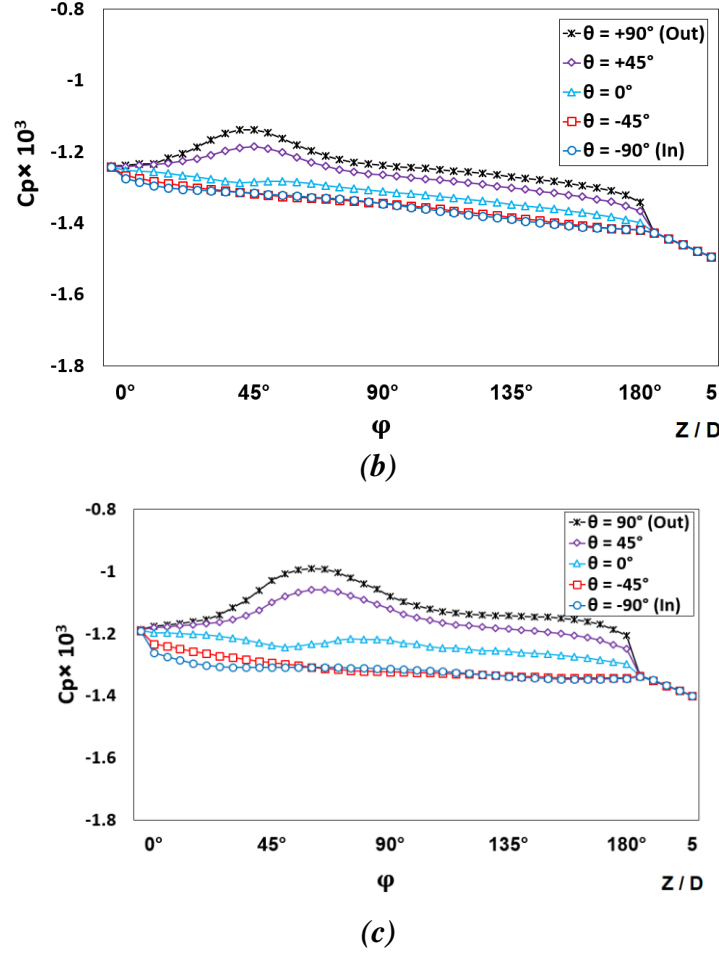
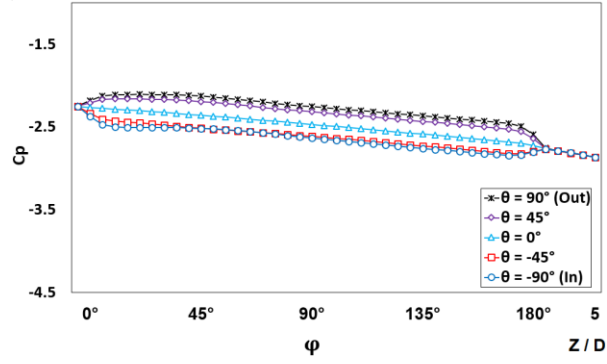


Fig. 2.8 Pressure coefficient of flow at $Re = 600$ inside the bend with (a) the curvature ratio of 0.1, (b) the curvature ratio of 0.25 , and (c) the curvature ratio of 0.5

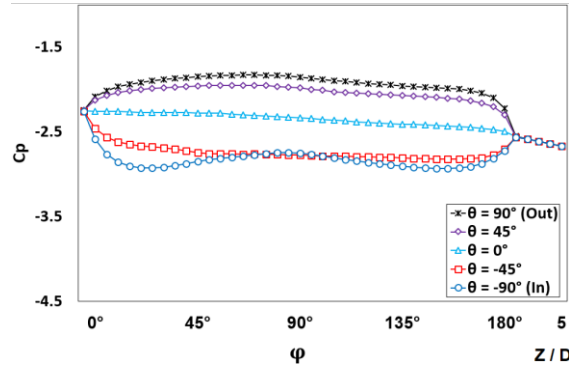
2.5.2 Distribution of pressure at $Re = 6 \times 10^4$

Fig. 2.9 shows the pressure distribution of flow in the bend and some downstream distances. When the fluid enters the U-bend, the uniformity of pressure is disturbed. In a way that the pressure in the outer wall increases and the pressure in the inner wall decreases. The increase of Dean number causes a larger variation of pressure. As a result, the curvature ratio of $\delta = 0.5$ has a wider distribution of pressure. This is basically due to the fact that the pressure gradient that is generated to balance the centrifugal force is so large that deflects the growth of pressure toward the inner wall. The result is that the pressure in the inner wall is lower than the pressure in the outer wall. Soon after the fluid

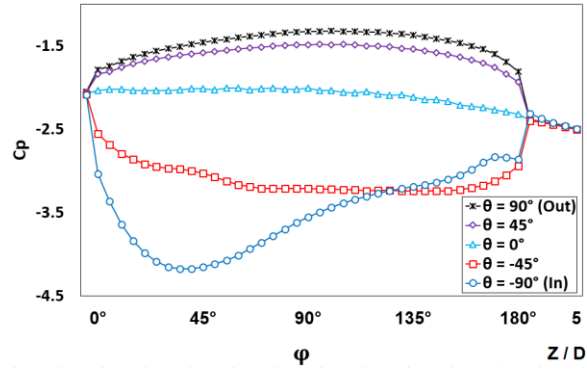
flows into the downstream, the pressure variations are alleviated and there is a uniform trend until the outlet.



(a)



(b)



(c)

Fig. 2.9 Pressure coefficient of flow at $Re = 6 \times 10^4$ with (a) the curvature ratio of 0.1 and (b) curvature ratio of 0.25, and (c) the curvature ratio of 0.5.

2.5.3 Total pressure loss

In this study, Eq. 2.13 has been defined to calculate the total pressure loss of the U-bend system. The results of the total pressure loss calculations for the three curvature ratios are demonstrated in Fig. 2.10. The comparison among the curvature ratios of 0.1, 0.25, and 0.5 when the flow is at $Re = 6 \times 10^4$ shows that the largest ($\delta = 0.5$) and the smallest ($\delta = 0.1$) bend curvatures of the studied cases have higher total pressure losses than the bend curvature of $\delta = 0.25$. That is to say, the increase of the bend curvature from 0.1 to 0.25 reduces the total pressure losses by 6.9% and the reduction of the bend curvature from 0.5 to 0.25 reduces the total pressure loss of the system by 3%. As a result, the curvature ratio must be focused when designing a U-bend system.

For the flow at $Re = 600$, however, the increase of the bend curvature ratio results in a consistent decrease of total pressure losses. From the curvature ratio of $\delta = 0.1$ to $\delta = 0.25$, the total pressure loss is decreased by 6.9% and from the curvature ratio of $\delta = 0.25$ to $\delta = 0.5$, the total pressure loss is reduced by 2.1%. This means that the consistent increase of curvature ratio reduces the amount of total pressure loss which seems to be reducing up to a certain point.

Considering the calculations, the total pressure loss conclusions, must be tied with the heat transfer of the U-bend systems to have a good judgement about the most efficient curvature ratio. The heat transfer will later be discussed in this chapter.

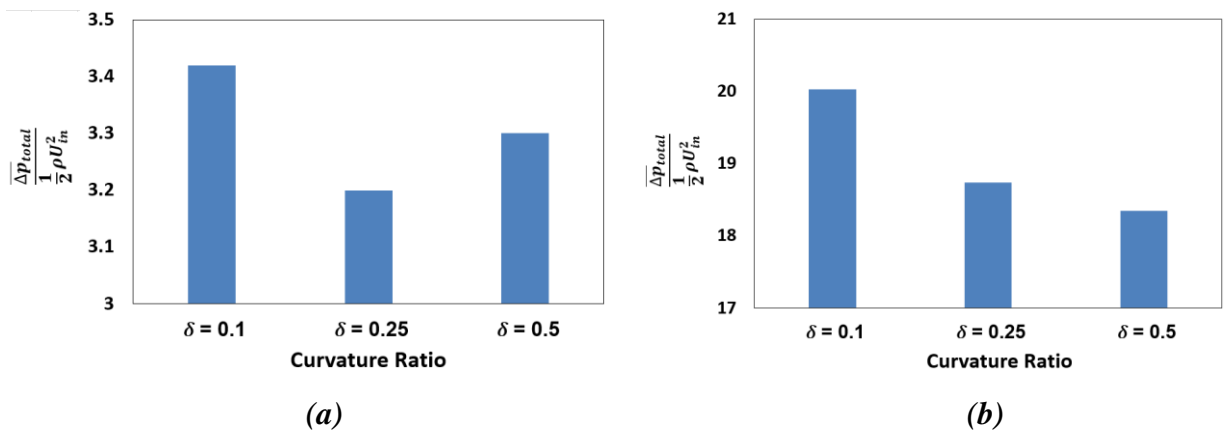


Fig. 2.10 Total pressure loss of the U-bend system with the flow at (a) $Re = 6 \times 10^4$ and the flow at (b) $Re = 600$

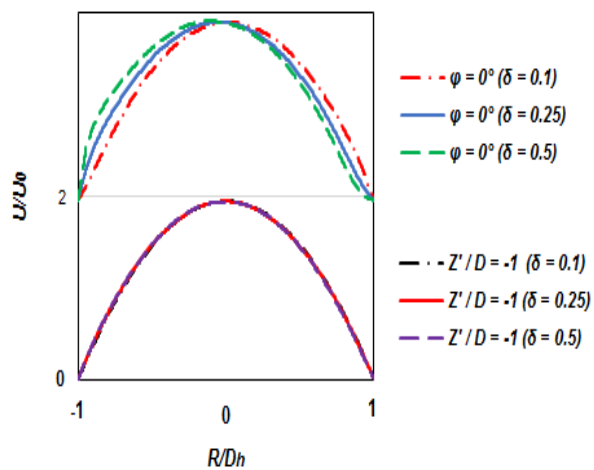
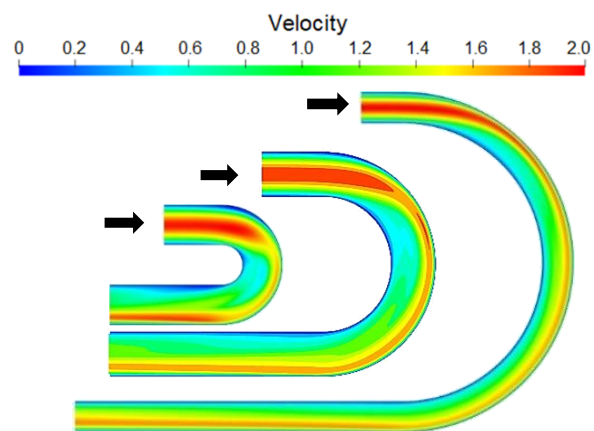
$$\text{Mass Flow Average of Total Pressure: } \bar{p}_t^M = \left(\frac{\rho}{m}\right) \int_A p_t (\vec{u} \cdot \vec{n}) dA \quad (2.13)$$

where p_t is the total pressure, M is the mass flow, A denotes the area of both inlet and outlet, \vec{u} is the velocity vector, \vec{n} is the unit vector that is normal to surface, and ρ is the density of the running fluid.

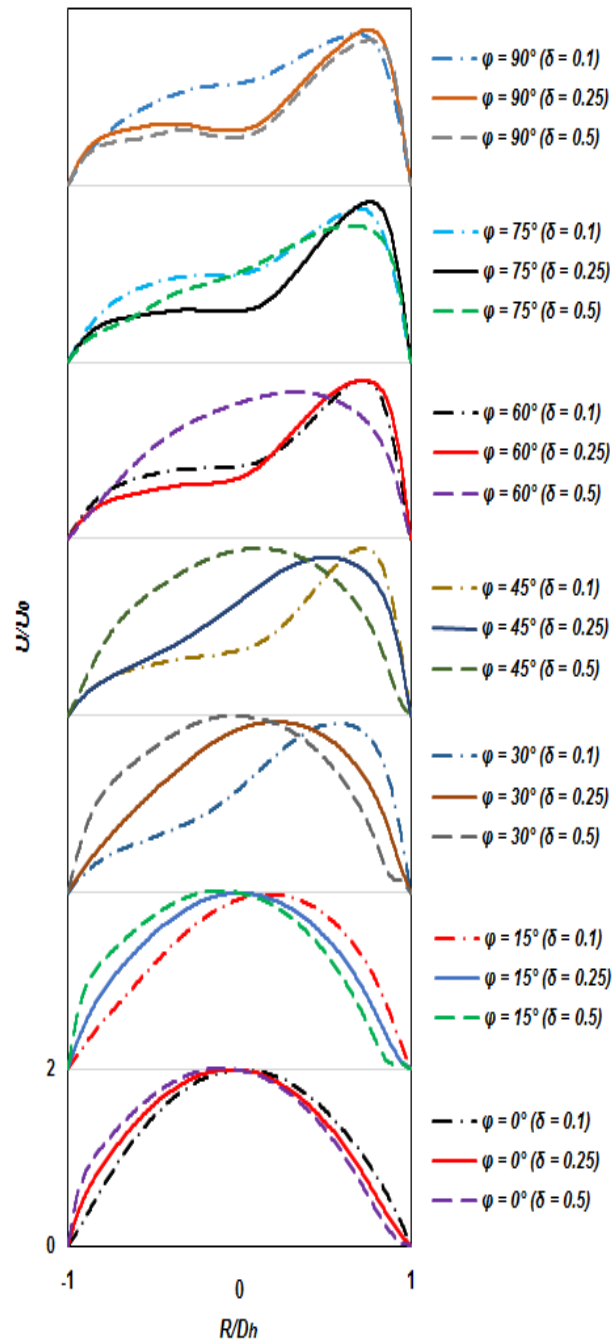
2.5.4 Velocity and Dean cell development

The velocity evolution of the three curvature ratios of flow at $Re = 600$ inside the U-bend is shown in Fig. 2.11. Also, Fig. 2.12, 2.13, and 2.14 show the velocity contours of the flow inside the U-bend with the curvature ratios of 0.1, 0.25, and 0.5, respectively. Similarly, the velocity evolution of the three curvature ratios of the flow at $Re = 6 \times 10^4$ is demonstrated in Fig. 2.15, with the contours of the lowest to the highest curvature ratios as per Fig. 2.16, 2.17, and 2.18. The left and right hand side of each figure is the inner curvature wall and the outer curvature wall respectively. Also, the normalized velocity of every single graph is within the scale of 0 to 2.

As shown in Fig. 2.11-a, when the fully developed laminar flow is introduced to the bend inlet, a small velocity deflection occurs toward the inner curvature wall, in a way that the velocity displacement is larger in a higher Dean number. Shortly after the fluid travels inside the bend, the generated centrifugal force impacts the incoming flow, resulting in a large pressure gradient in the space between the centerline and the outer wall to balance the centrifugal force. As a result, the momentum of flow is directed toward the outward region (Fig. 2.11-b). But this move occurs faster in lower Dean numbers due the lower curvature ratio of the bend. Also, the large flow momentum near the outer wall moves toward the inner wall, making two velocity peaks on both sides and a valley in the middle (Fig. 2.11-c). This valley abates when the fluid momentum in the inner half of the secondary flow is driven to the center, making the smallest flow momentum in the inward wall (Fig. 2.11-d).



(a)



(b)

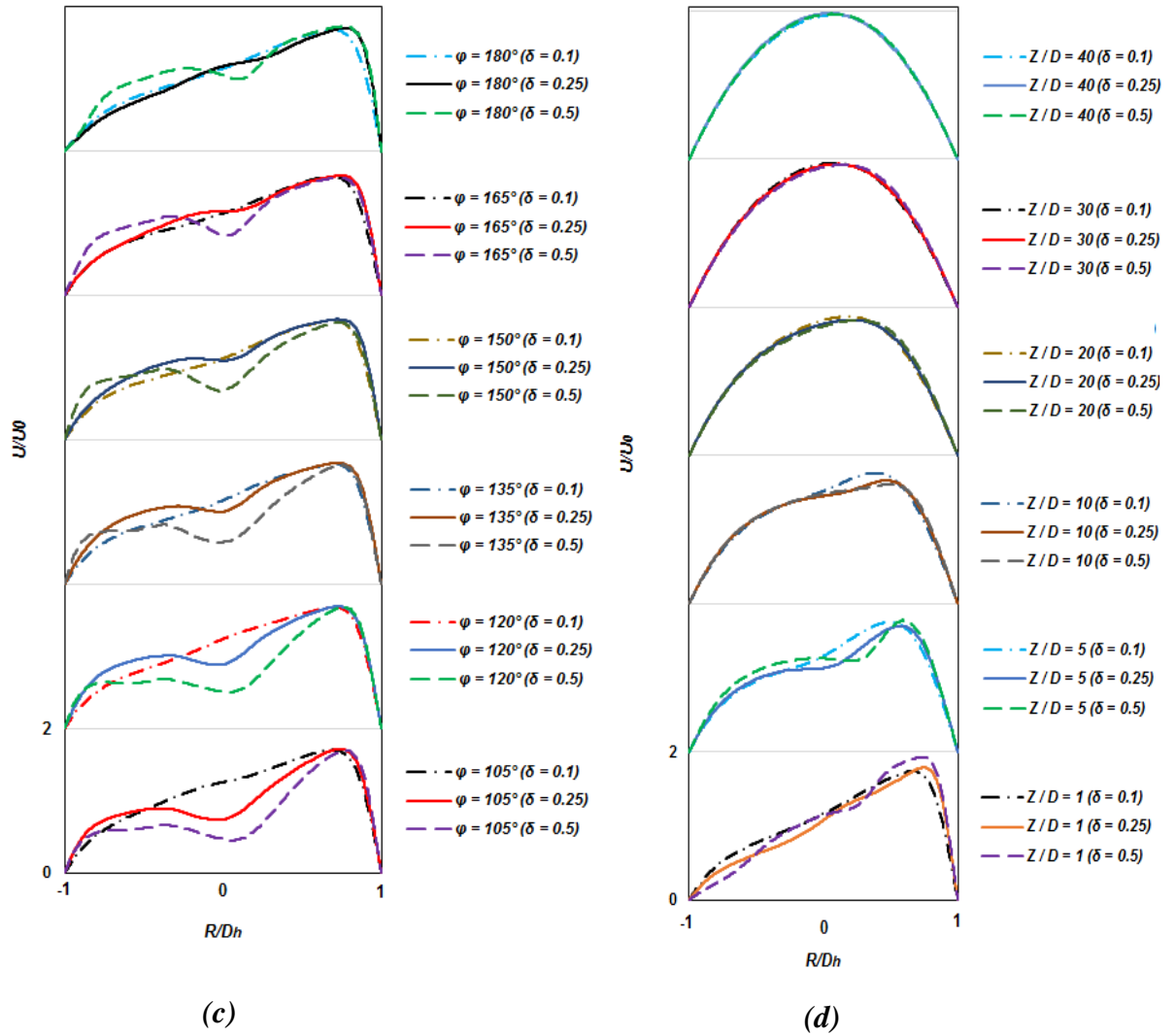
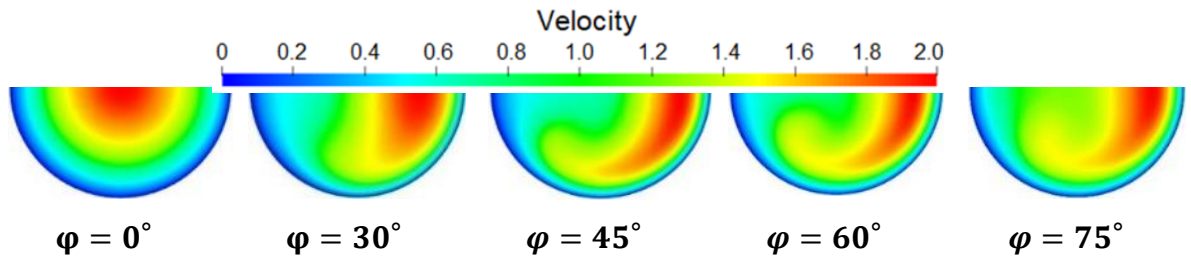


Fig. 2.11 Velocity distribution of flow at $Re = 600$ along the bends with the curvature ratios of 0.1, 0.25, and 0.5 and downstream



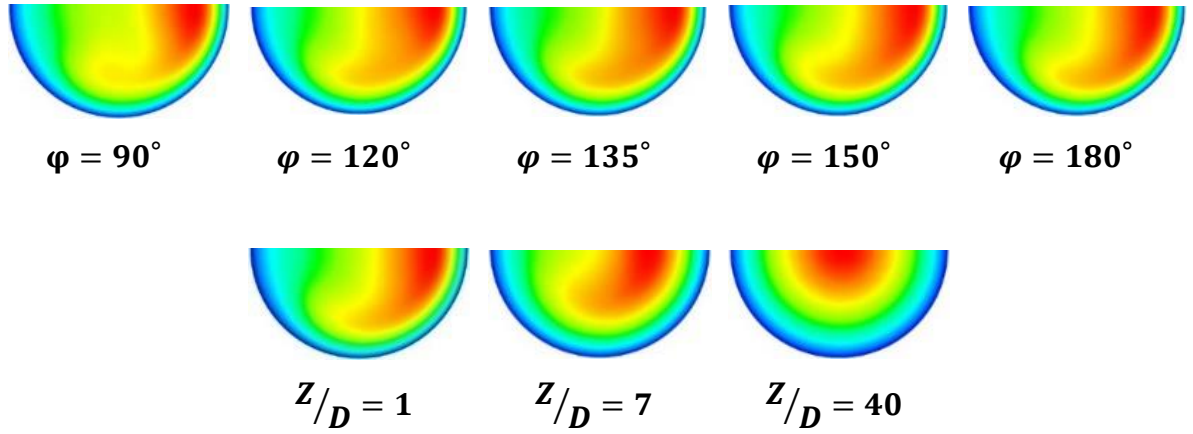


Fig. 2.12 Velocity contours for $Re = 600$ & $De = 190$ ($\delta = 0.1$) at different cross sections. The left hand side of each cross-section is the inner wall and the right hand side is the outer wall of the secondary flow

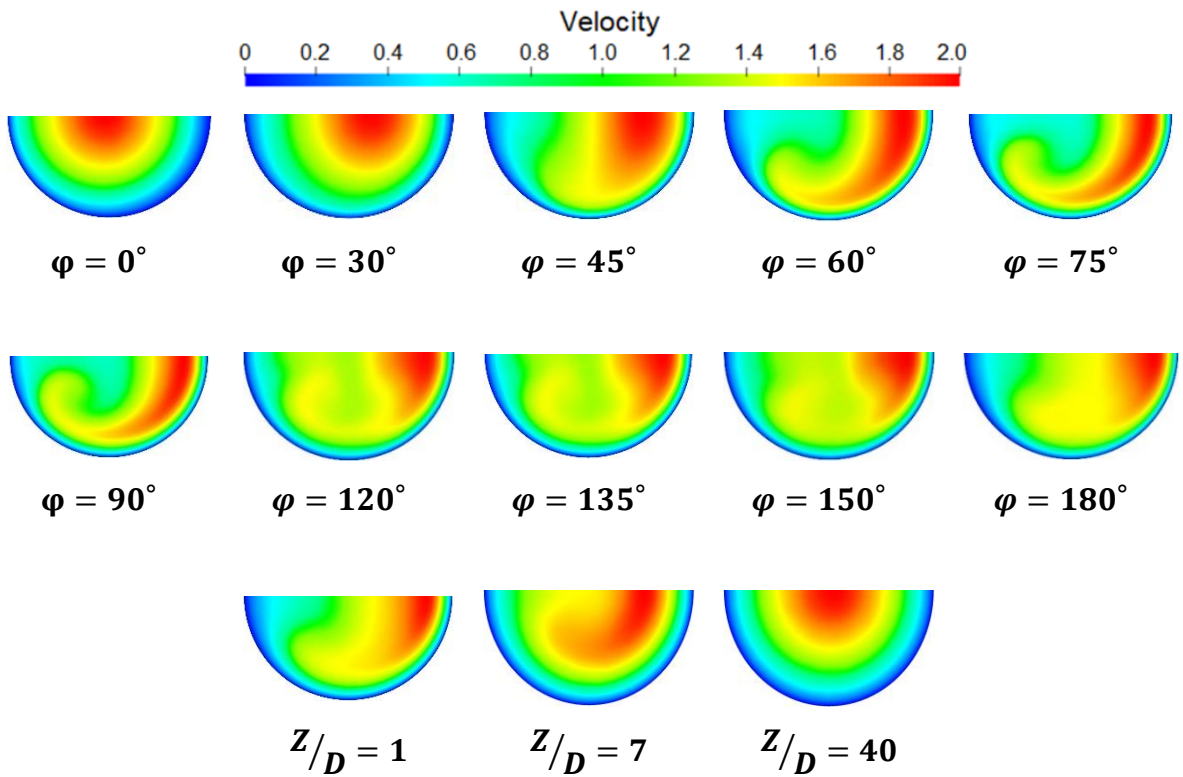


Fig. 2.13 Velocity contours for $Re = 600$ & $De = 425$ ($\delta = 0.25$) at different cross sections. The left hand side of each cross-section is the inner wall and the right hand side is the outer wall of the secondary flow

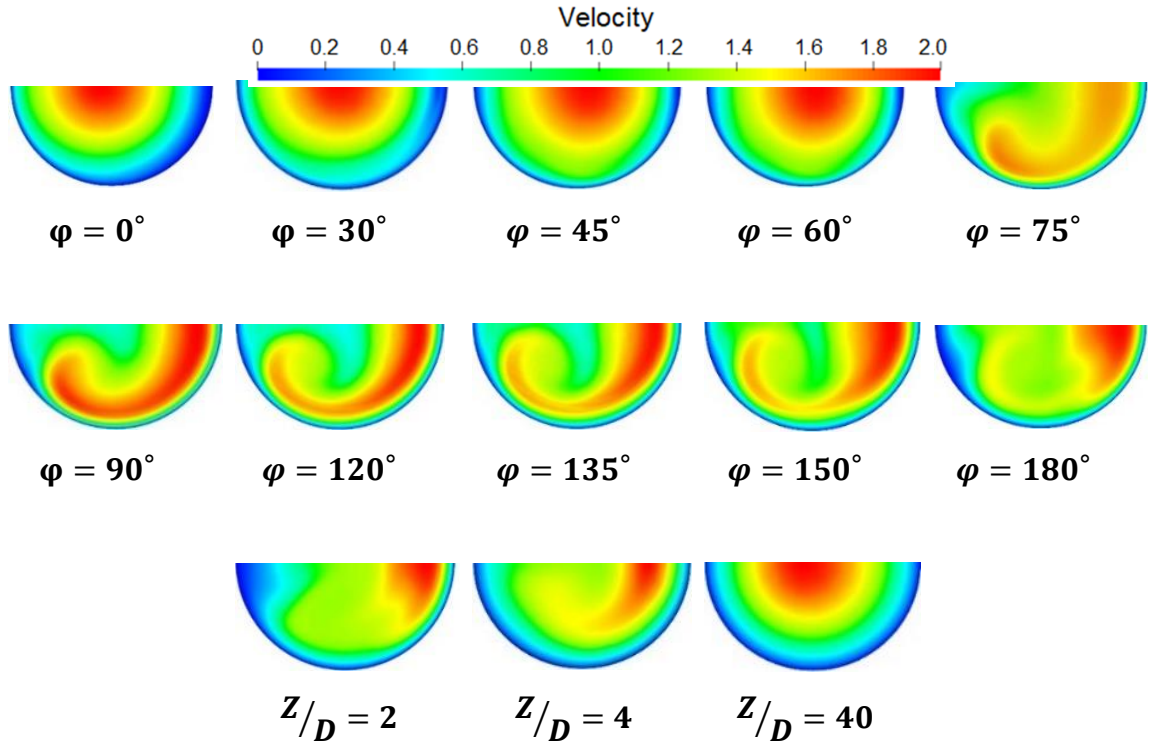
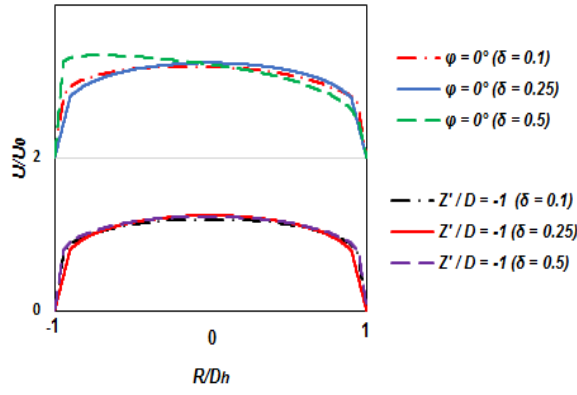
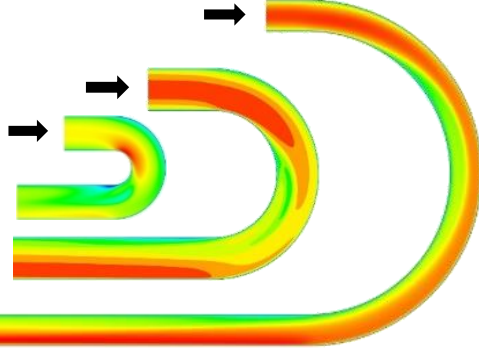
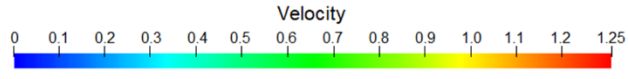
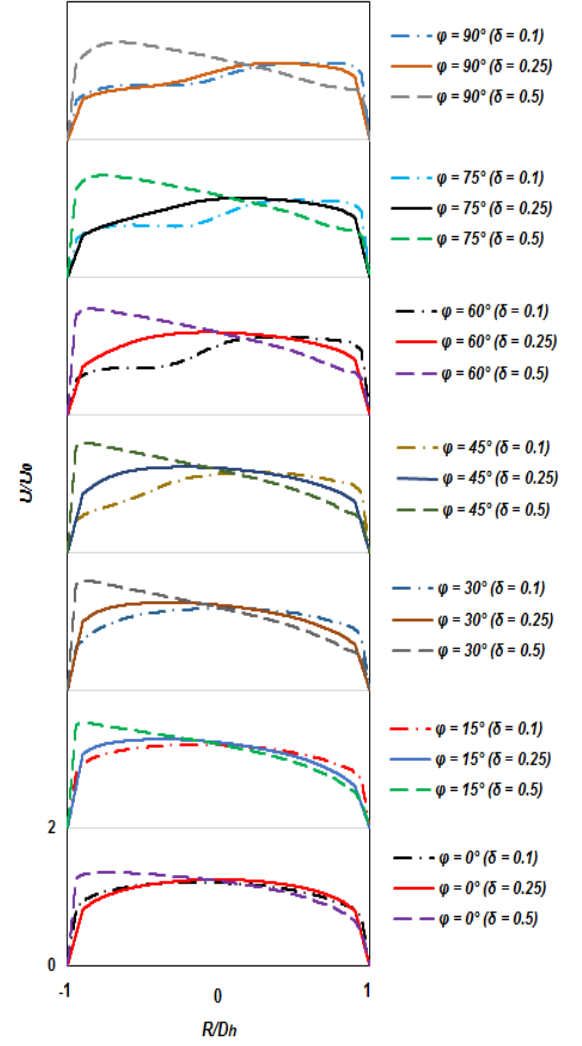


Fig. 2.14 Velocity contours for $Re = 600$ & $De = 425$ ($\delta=0.5$) at different cross sections. The left hand side of each cross-section is the inner wall and the right hand side is the outer wall of the secondary flow

When the fully developed flow at $Re = 6 \times 10^4$ enters the bend inlet (Fig. 2.15-a), there is a large shift of fluid momentum toward the inner wall due to the rapid and large formation of pressure gradient to balance the centrifugal force (Fig. 2.15-b). This momentum displacement is stronger with longer durability with the curvature ratio augmentation until the fluid flows to the second half of the bend. Also, the fluid momentum displacement toward the outer wall occurs quicker within the first half with the reduction of the bend curvature. Once the fluid momentum in the inward region moves from the circumference to the outer wall with the larger curvature ratio (i.e. $\delta = 0.5$), the velocity peak in the inward region depreciates (Fig. 2.15-c), but still does not decay thoroughly until the fluid flows through the downstream. As a result, a valley starts to grow in the space between both halves which delays the recovery of flow in the downstream (Fig. 2.15-d).



(a)



(b)

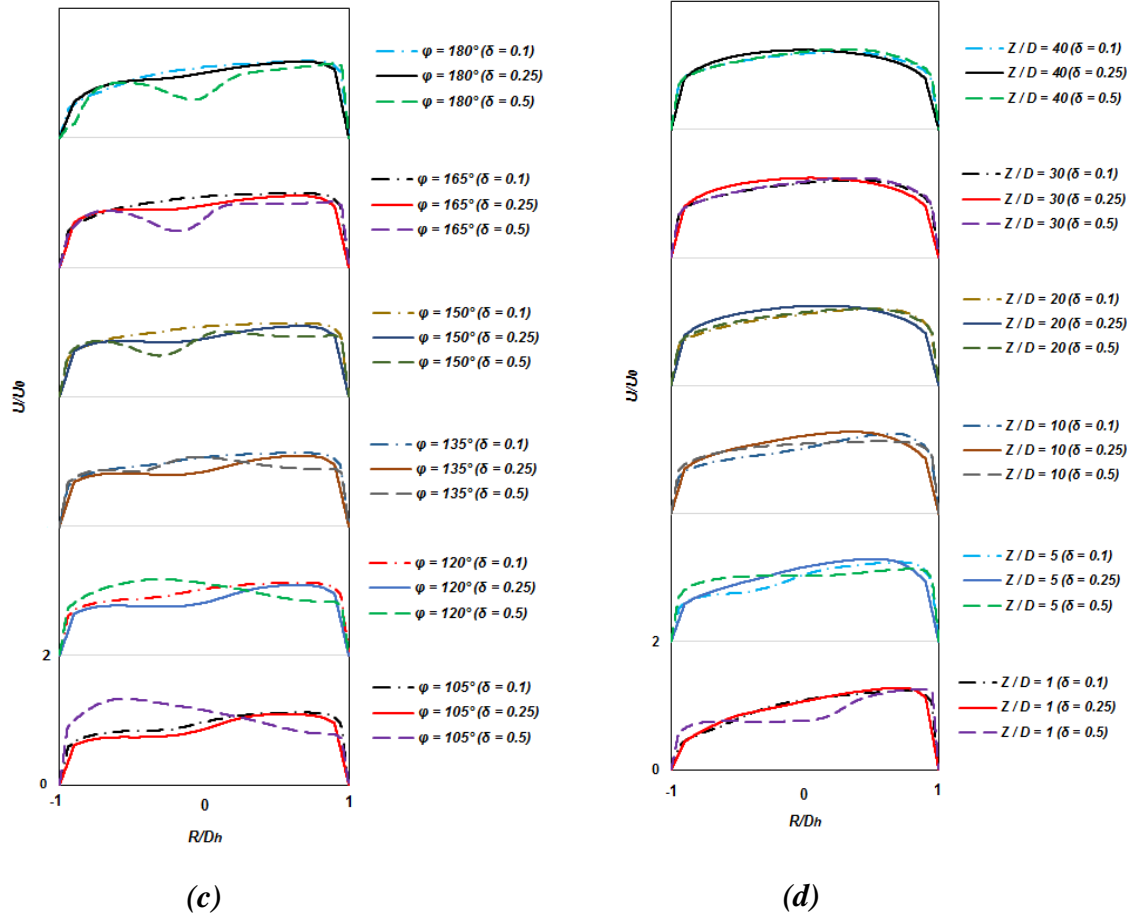
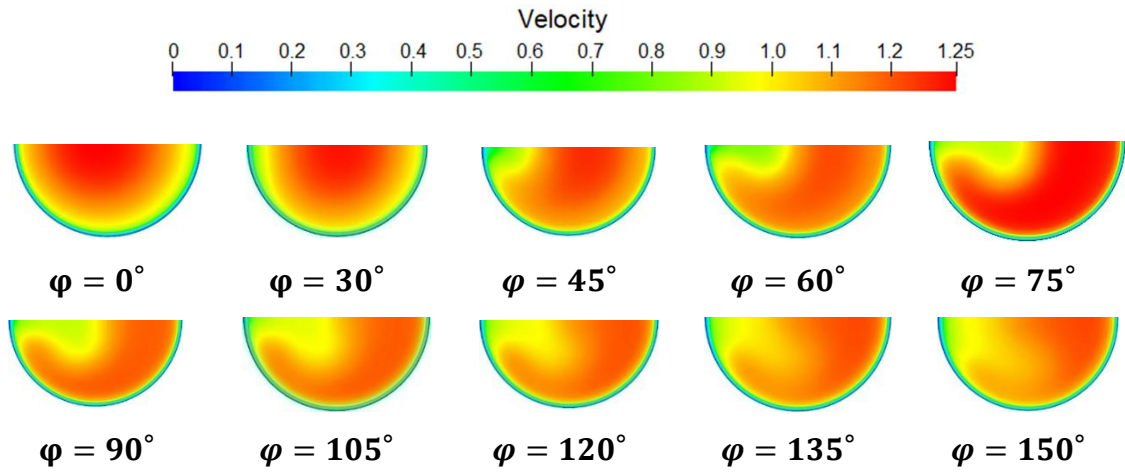


Fig. 2.15 Velocity distribution of flow at $Re = 6 \times 10^4$ along the pipe bends with the curvature ratios of 0.1, 0.25, and 0.1 and downstream. The left hand side is the inner wall and the right hand side is the outer wall.



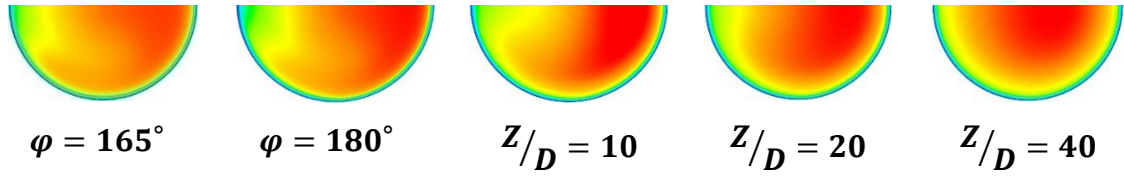


Fig. 2.16 Velocity contours of flow at $Re = 6 \times 10^4$ & $De = 425$ ($\delta = 0.10$) at different cross sections. The left hand side of each cross-section is the inner wall and the right hand side is the outer wall of the secondary flow

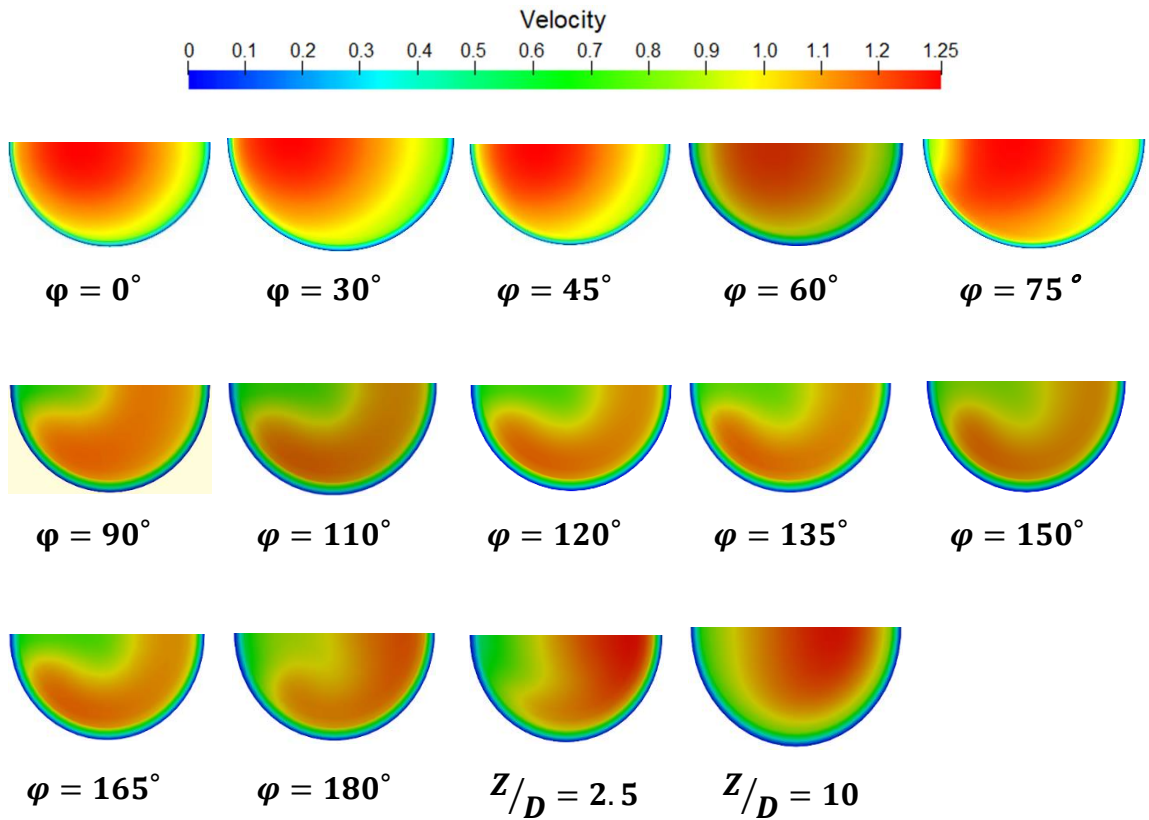


Fig. 2.17 Velocity contours of flow at $Re = 6 \times 10^4$ & $De = 425$ ($\delta = 0.25$) at different cross sections. The left hand side of each cross-section is the inner wall and the right hand side is the outer wall of the secondary flow

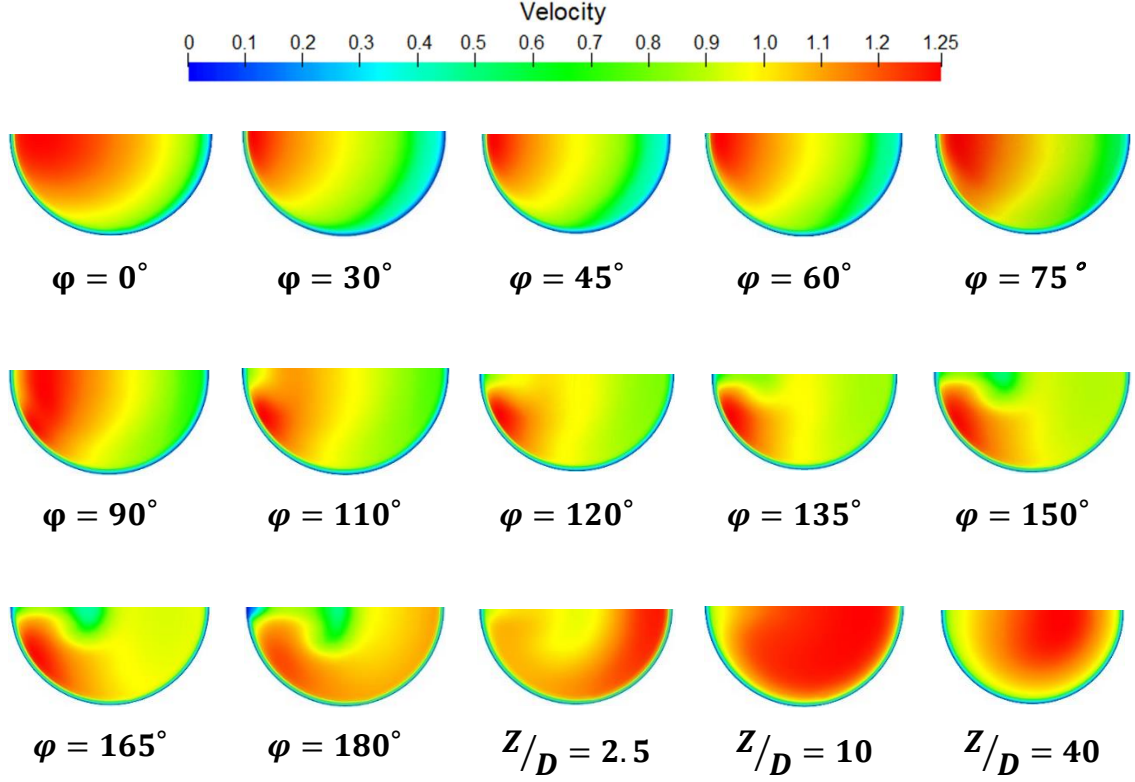


Fig. 2.18 Velocity contours of flow at $Re = 6 \times 10^4$ and $De = 425$ ($\delta = 0.5$) at different cross sections The left hand side of each cross-section is the inner wall and the right hand side is the outer wall of the secondary flow

The velocity at the bend and downstream cross sections are shown in Fig. 2.12, 2.13, and 2.14 which represent the flow at $Re = 600$ and Fig. 2.16, 2.17, and 2.18 that show the development of fluid velocity at $Re = 6 \times 10^4$. As per the law of conservation of energy, it can be inferred that when the fluid velocity increases as a result of centrifugal force and pressure gradient interactions at a constant mass flow rate (due to a constant fluid density), the increase of kinetic energy of the fluid must be coming from the pressure. As a result, the pressures go down at those spots where there is increased velocity (pressure distribution already discussed at Fig. 2.8 and 2.9).

In both flow models, the velocity change procedure in the case with a sharper bend occurs slower with more variations. This may be due to the fact that the evolution of velocity within a curved passage takes more effect from the traveled length than the

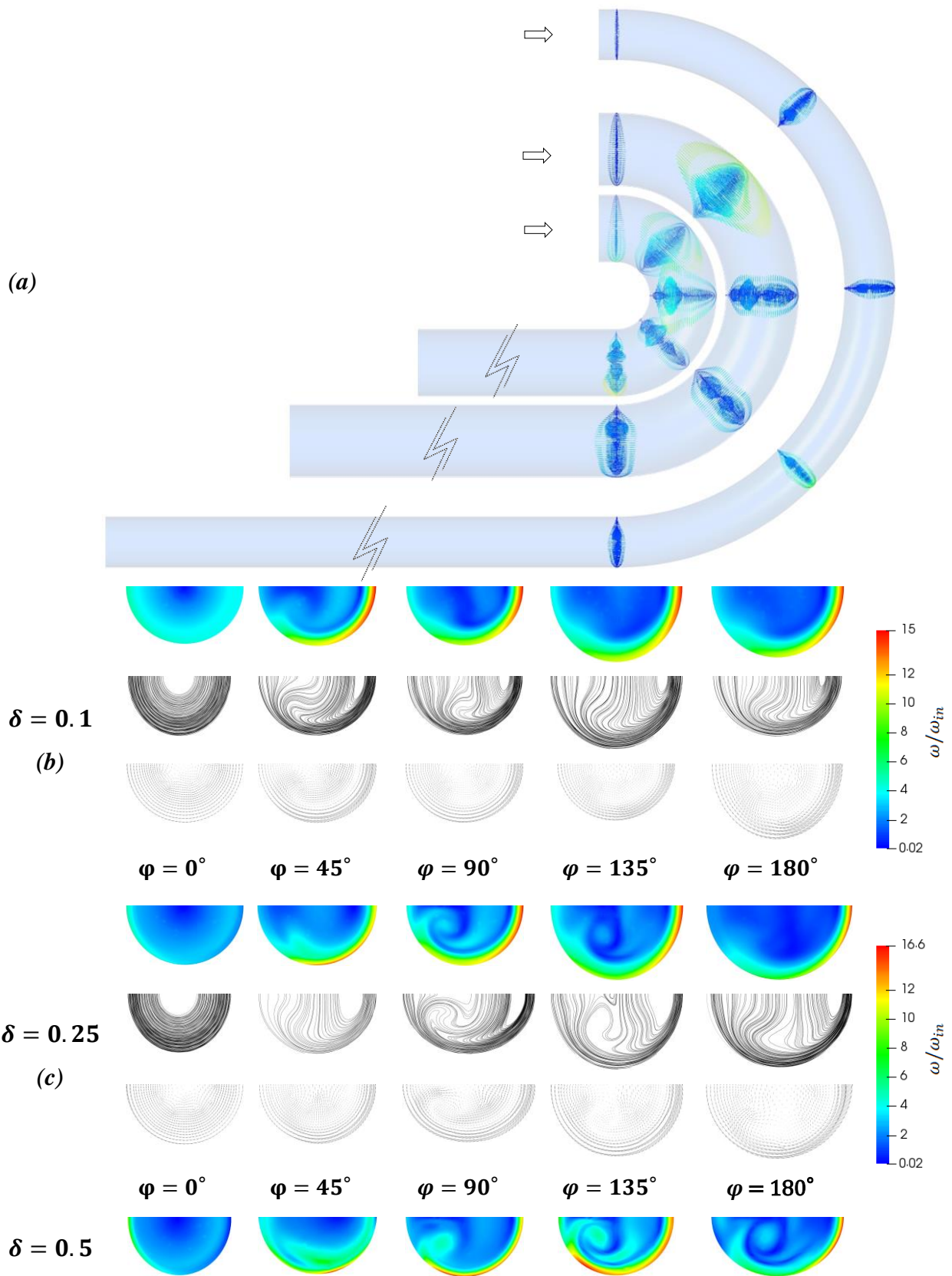
traveled angle. When the Reynolds number of the flow is 600, the recovering rate of velocity to its parabolic form within the hydraulic diameter of the downstream becomes slower as the curvature ratio increases. In the flow at $Re = 6 \times 10^4$, however, the velocity in $\delta = 0.25$ is recovered faster than other two simulated models in the downstream.

2.5.5 Vorticity

Fig. 2.19 and 2.20 show the vorticity contours and the normal vorticity vectors of flow inside the bend with the three curvatures. In ParaView, the vorticity is specified with creating a velocity field, then creating a Warp by Scalar at a specified location that we want to demonstrate the vorticity, and finally computing Derivatives with selecting the output vector type as vorticity and the output sensor type as Strain.

As per Fig. 2.19-a, the normal vectors of vorticity at the symmetry planes of the bend with the bend angles of 0° , 45° , 90° , 135° , and 180° in the three bends shows that when the fluid is introduced to the bend, the normal vorticity increases near the wall. Soon after running inside the bend, the normal vorticity increases near the outer wall. For the curvature ratios of 0.1 and 0.25, the normal vectors of vorticity grow in the middle and in the vicinity of the outer wall until the fluid exits the bend. However, for the curvature ratio of 0.5 (a sharp curvature) there is a reduction of vorticity near the outer wall with an increase adjacent to the inner wall near $\varphi = 90^\circ$ of the bend. In the second half of the bend, normal vectors of vorticity have almost equal values in each cross section, but as the running fluid approaches the bend exit, the vorticity near the outer wall increases more than the inner wall.

Observing the vorticity magnitude as per Fig. 2.19-b, 2.19-c, and 2.19-d, shows that the maximum vorticity occurs in the outer wall. The vorticity magnitude rises near the axis of symmetry. This generated vorticity is particularly noticeable when increasing the curvature ratio of the bend. It is also observed that the vorticity begins to rise at the initial bend angles when increasing the Dean number. Also, the vorticity becomes maximum in the second half of the bend, and lasts longer in a more curved bend.



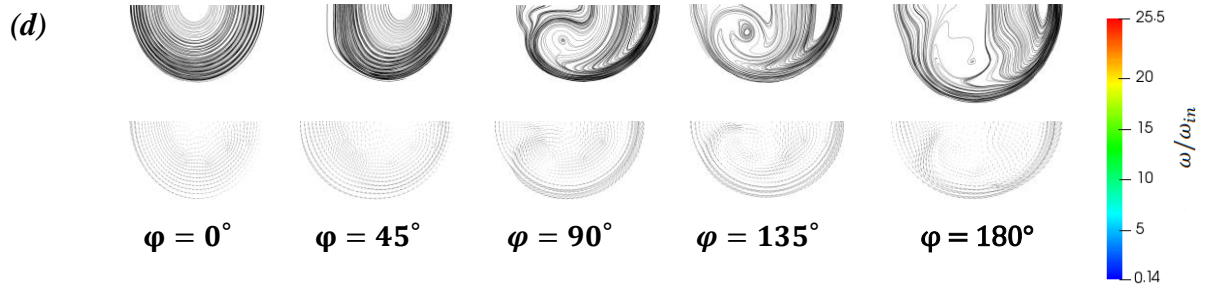
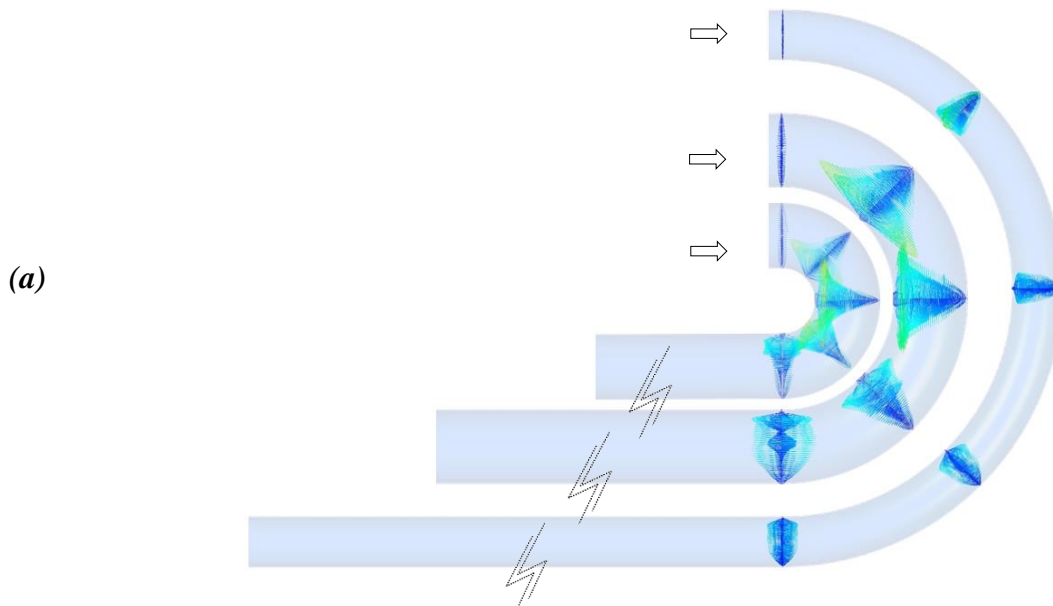


Fig. 2.19 Dimensionless vorticity contours, streamlines, and vector lines of flow at $Re = 600$ for the curvature ratios of 0.1, 0.25, and 0.5

The normal vectors of vorticity and the vorticity contours of flow at $Re = 6 \times 10^4$ with the three curvature ratios are shown in Fig. 2.20. As per Fig. 2.20-a, for all the three curvature ratios, the normal vectors of vorticity is very large near the inner wall all through the bend. As the flow travels into the bend, the normal vorticity gradually is enhanced near the outer wall until the flow exits the bend.

In Fig. 2.20-b, 2.20-c, and 2.20-d it is observed that a large magnitude of vorticity occurs in the inner wall and grows toward the axis of symmetry in the first 90 degrees of the bend. In the second half of the bend, the vorticity moves toward the inner wall as the flow approaches the bend exit, and increases in magnitude in the inner wall. Also, the effect of curvature enhances the vorticity magnitude and its longevity, however, delays the onset of vorticity formation.



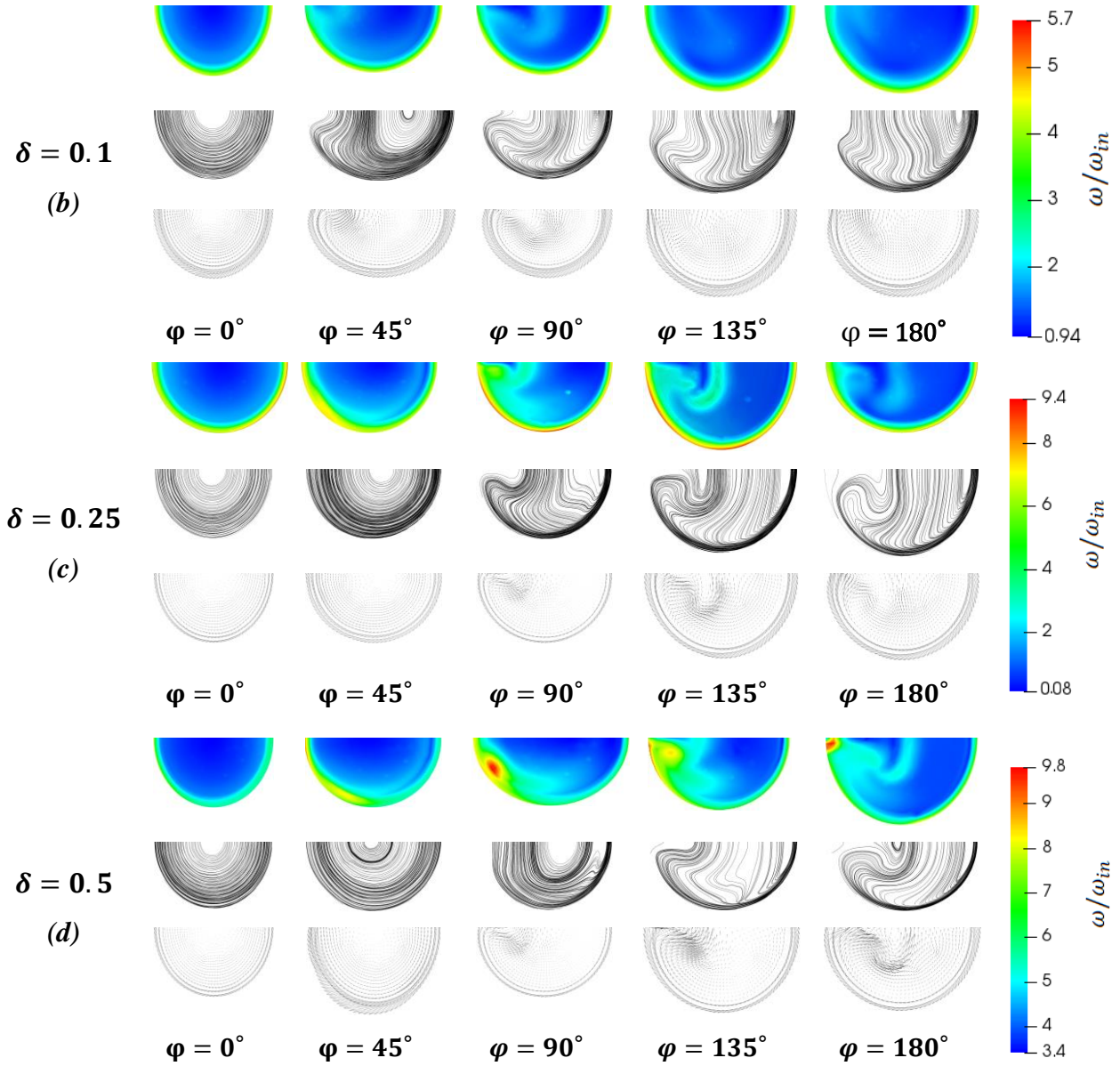


Fig. 2.20 Vorticity contours, streamlines, and vector lines of flow at $Re = 6 \times 10^4$ for the curvature ratios of 0.1, 0.25, and 0.5

2.5.6 Turbulent Kinetic Energy

Fig. 2.21 shows the turbulent kinetic energy of flow at $Re = 6 \times 10^4$ for the three curvature ratios of 0.1, 0.25, and 0.5. It is observed that the bend curvature increases the turbulent kinetic energy and a sharper bend results in a larger magnitude of turbulent kinetic energy. In all the cases, there is a reduction of turbulent kinetic energy in the initial distances of the inner wall and an enhancement of it in the outer wall. The delay in the

generation and dissipation of it inside the bend compared with the velocity and vorticity which demonstrate the same trend shows that the development of velocity, vorticity, and turbulent kinetic energy do not depend on the bend angle (φ), but the traveled path of the bend ($P = R_c \times \varphi$).

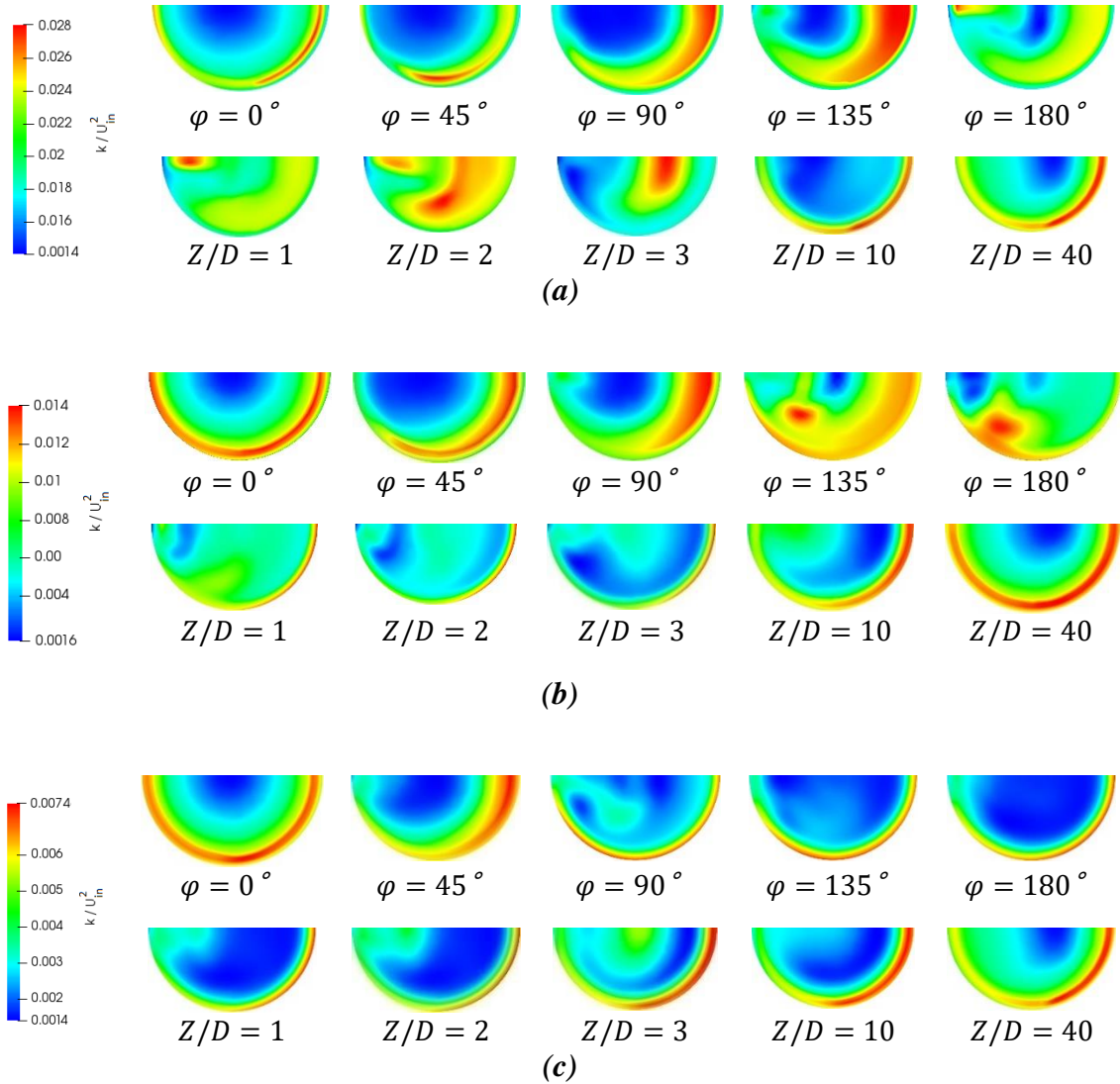


Fig. 2.21 Turbulent kinetic energy of flow at $Re = 6 \times 10^4$ with the curvature ratio of (a) $\delta = 0.5$, (b) $\delta = 0.25$, and (c) $\delta = 0.1$

2.5.7 Dean cell development at $Re = 600$

In curved pipes, the secondary flow motion is generated in the plane perpendicular to the incoming flow. This phenomenon known as Dean cells is due to the generation of the centrifugal forces that shift the axial fluid flow toward the wall of the curve (Noorani

et al. 2013) and deflect the fluid due to its interaction with the pressure gradient. These motions that make up counter rotating vortices, spin from the inner wall to the outer wall in relation to the vertical axis that crosses from the diameter of the plane (See Fig. 2.1).

In the bend with the curvature ratio of 0.5 shown in Fig. 2.22, after the base cell generation, that is inherent to all bends, the split-base, central base, and inner wall cells start to shape up in the second half of the bend, making four Dean cells at each semi-circular plane. Although the central and inner wall cells disappear before the bend outlet, the base bend and the split-base cell flow into the downstream. Inside the downstream one small cell shapes up and depreciates quickly at about the bottom center at $Z/D = 0.01$. Also the central and the inner wall cells are recovered and depreciated from $Z/D = 0.2$ to 1 and $Z/D = 3.2$ to 5.3 respectively.

For the curvature ratio of 0.25 in Fig. 2.23, the onset of Dean cells occur once the flow enters the bend, and make up vortices known as base cell which circles at the entire secondary flow domain and develops. The core of the base cell is about the mid-half of the circulation domain that gradually moves toward the inner wall. Before the 90-degree bend, a pair of kidney shaped vortices called the base-split cell, starts to grow due to the emergence of an additional pressure gradient in the lower part of the domain near the skin. Once the base-split cell is thoroughly created, another pair of vortices is generated at about the center of the secondary flow domain. Right after the formation of the third Dean cell, the fourth pair of vortices named inner wall cell shapes up from about $\varphi = 85^\circ$ because of the boundary layer separation.

At the second half of the bend, the inner wall cell begins to depreciate and then the central cell and the base-split cell start disappearing respectively. In the bend outlet, both sets of cells are thoroughly disappeared, so there is only the base cell which is still in the downstream. Here in the downstream, as the base cells become smaller in size along the pipe, it moves toward the center of the secondary flow domain.

As per Fig. 2.24, for the curvature ratio of 0.1, the Dean cell development starts with the base cell. This cell splits and makes a temporary split-base along with a temporary central cell in the first half of the bend and then disappears by the bend angle of 90° . The

Dean cell is located in the inward region and does not change its position (except some minor displacements particularly while Dean cell splitting takes place). Also, another split-base cell shortly emerges and disappears in the initial downstream distances.

The decay of the cells in all the three cases of flow at $Re = 600$ occur at nearly similar downstream locations, this decay occurs almost equally on each side of both secondary flow domains at each flow cross section.

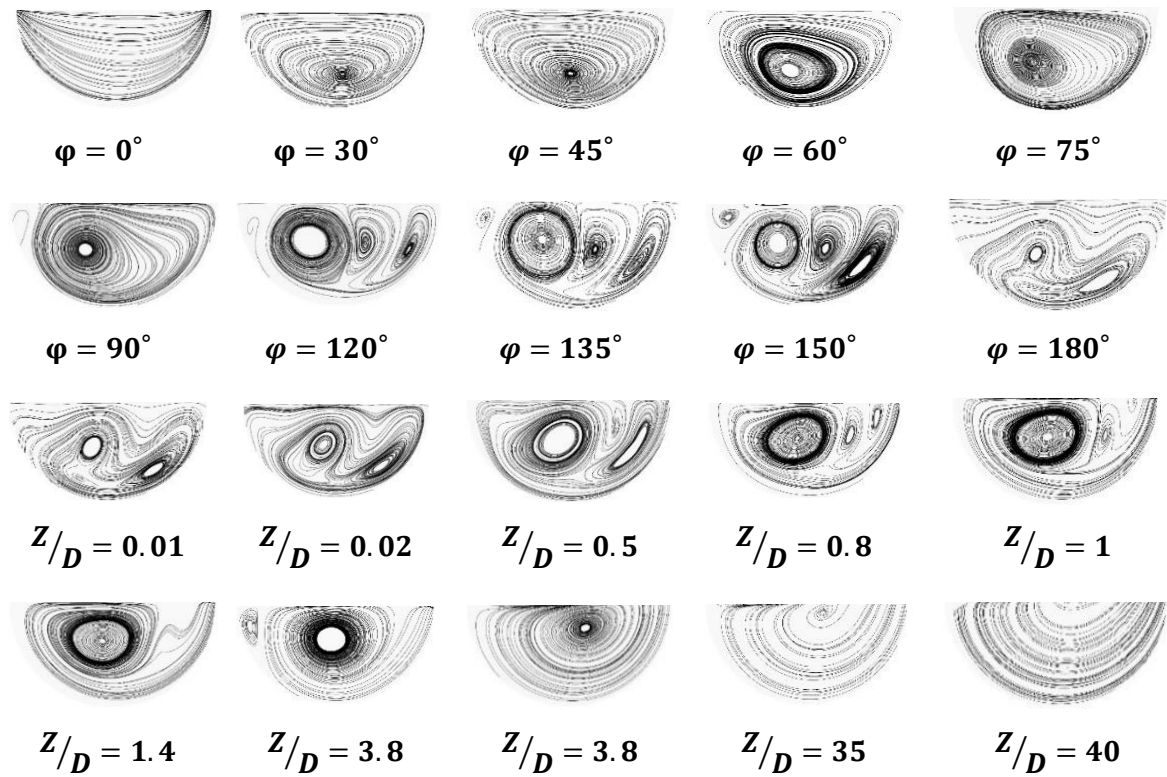
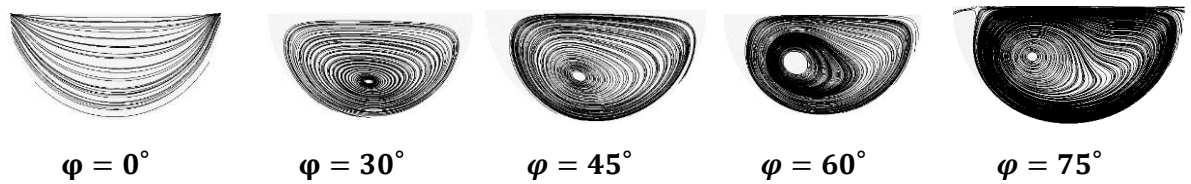


Fig. 2.22 Streamlines of flow at $Re = 600$ along the bend and downstream with the curvature ratio of 0.5



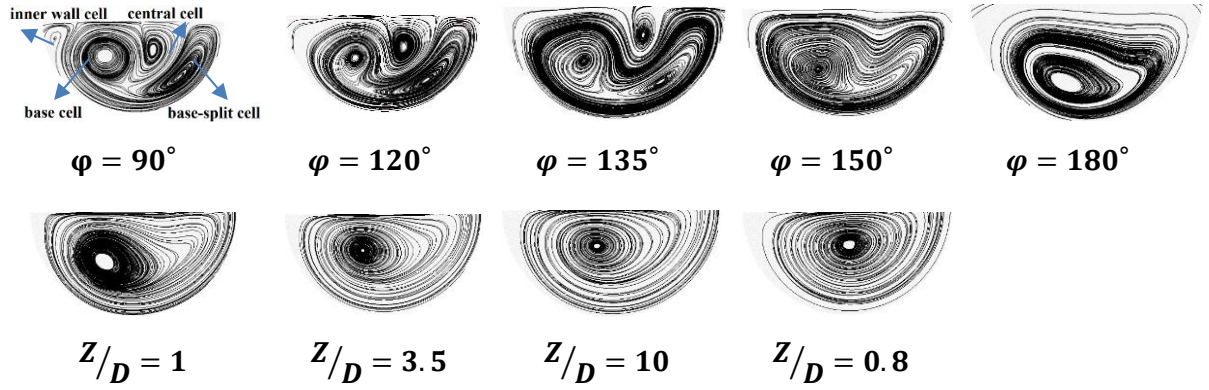


Fig. 2.23 Streamlines of flow at $Re = 600$ along the bend and downstream with the curvature ratio of 0.25

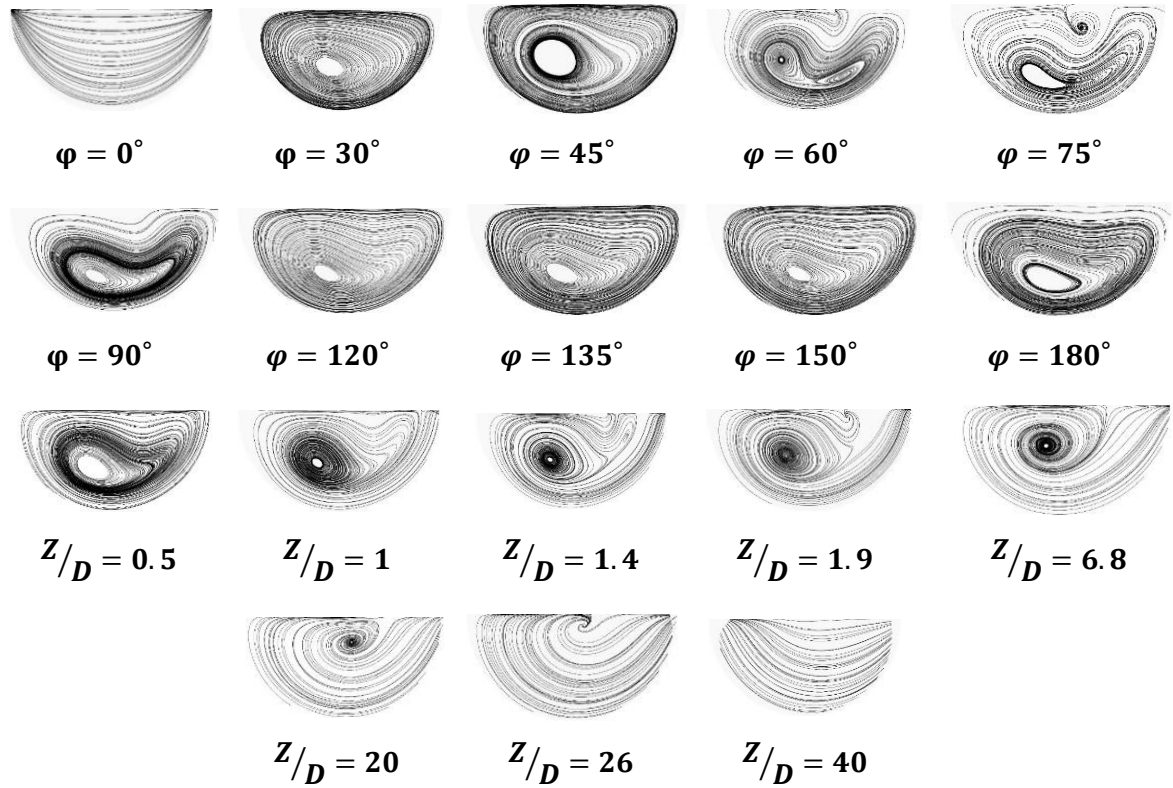


Fig. 2.24 Streamlines of flow at $Re = 600$ along the bend and downstream with the curvature ratio of 0.1

2.5.8 Dean cell development at $Re = 6 \times 10^4$

As per Fig. 2.25, at the curvature ratio of 0.5, the augmentation of curvature ratio prevents the central and the base-split cell to shape up because a sharp bend creates a very

large pressure gradient that makes no local imbalance between the centrifugal forces and radial pressure gradient in the center. As a result, only the base Dean cell is created from the bend entrance which lasts till the flow runs into downstream. When the curvature ratio is decreased to 0.25 and 0.1 (Fig. 2.26 & 2.27), both central and base-split cells are created due to the reason discussed earlier. However, they demonstrate different behaviors as the flow runs from the bend outlet through downstream. For the curvature ratio of 0.25, all disappeared vortices are regenerated in the downstream whereas for $\delta = 0.1$, Dean cells do not regenerate. As a result, only the base Dean cell runs into the downstream.

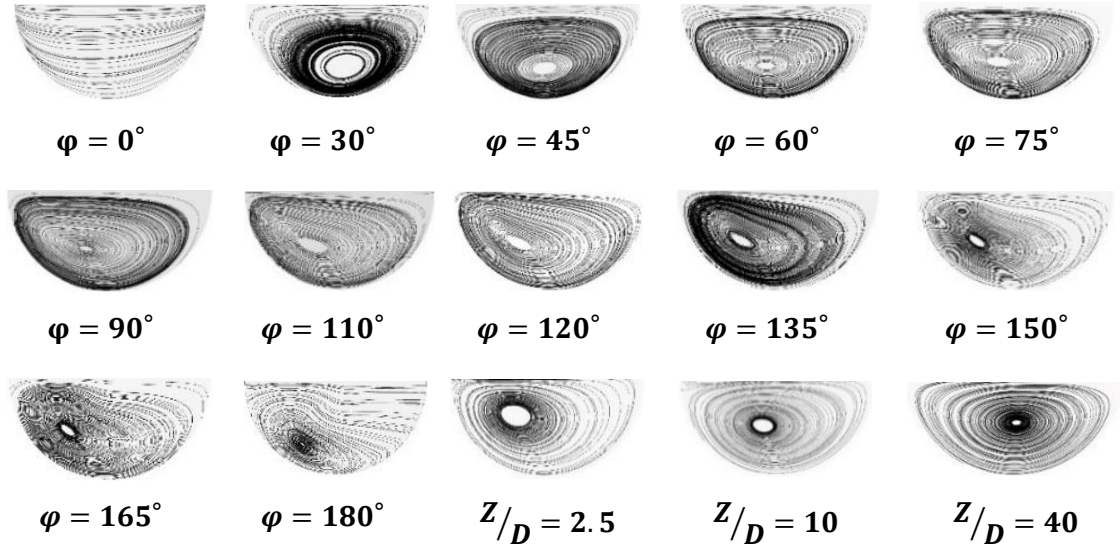
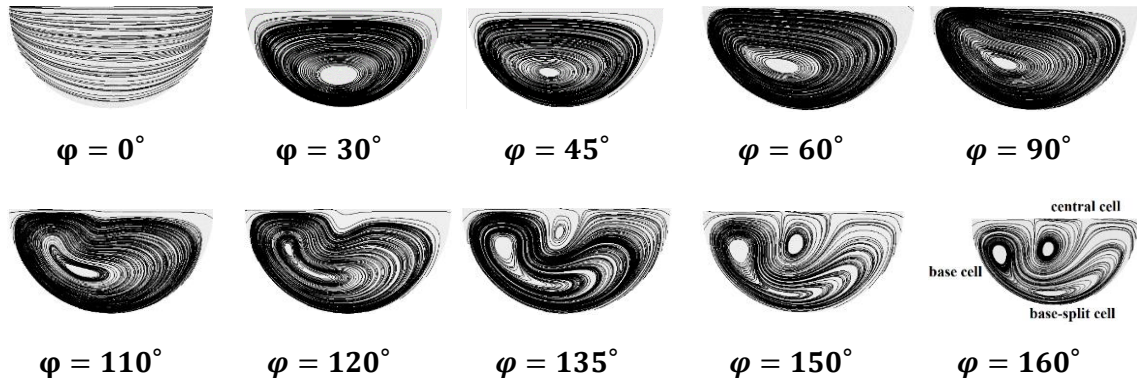


Fig. 2.25 Streamlines of flow at $Re = 6 \times 10^4$ along the bend and downstream with the curvature ratio of 0.5



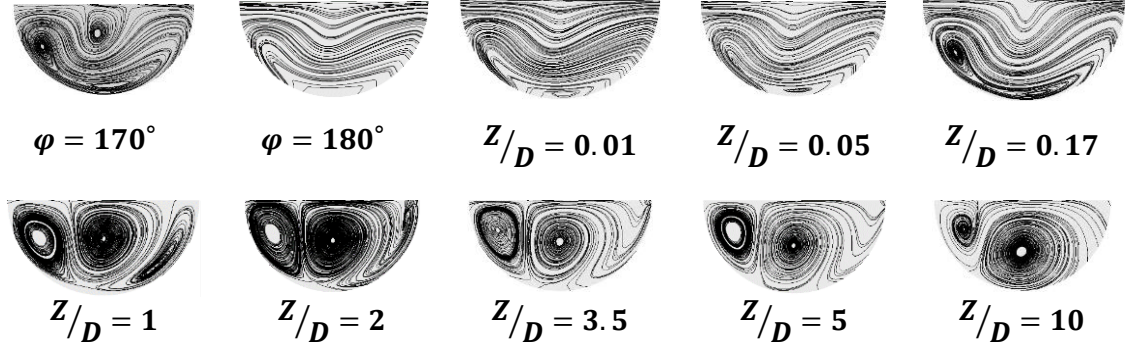


Fig. 2.26 Streamlines of flow at $Re = 6 \times 10^4$ along the bend and downstream with the curvature ratio of 0.1

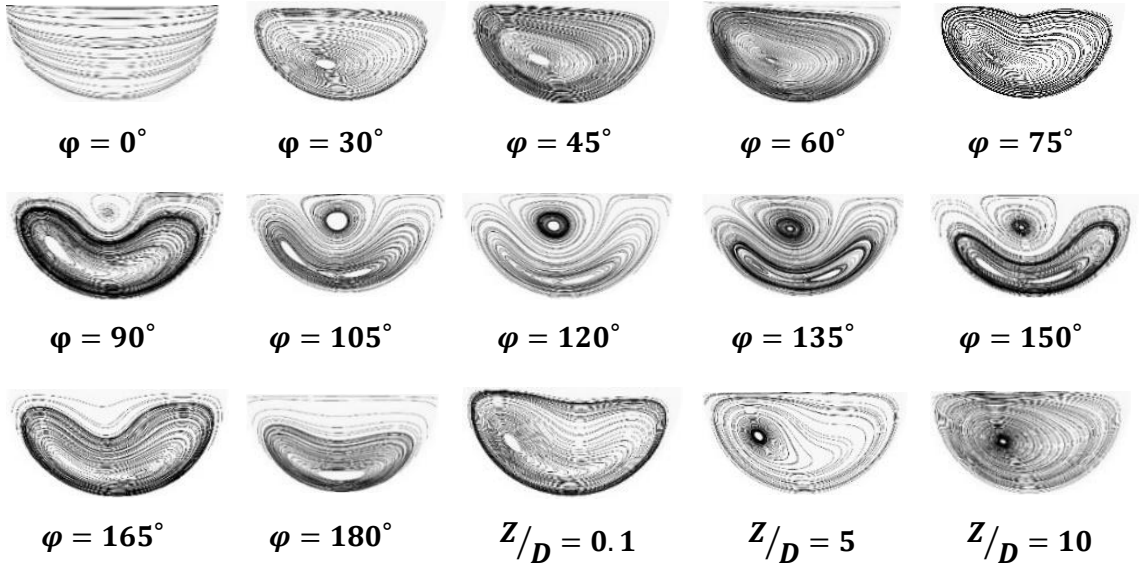


Fig. 2.27 Streamlines of flow at $Re = 6 \times 10^4$ along the bend and downstream with the curvature ratio of 0.1

2.5.9 Friction distribution

Knowing the fact that the pressure gradient is formed to balance the generated centrifugal force inside the U-bend, the regions of low and high pressures are created on each side of the peak of pressure gradient. Then the fluid with the high momentum and as a result, the velocity peak is deflected toward the low pressure region. It is observed that the increase or decrease of velocity in the vicinity of the walls impact the wall shear force and thus the friction coefficient directly. Having both flows of $Re = 600$ in Fig. 2.28 and

$Re = 6 \times 10^4$ in Fig. 2.29 into perspective, it is found that the friction magnitude on the surface of the secondary flow affects the U-bend with the increase of Dean number, that is to say, the augmentation of the curvature ratio intensifies variations of friction through the U-bend. The change in Dean Number of both flows ($Re = 600$ & $Re = 6 \times 10^4$) has an effect on the magnitude of shear rates, and there are some longitudinal displacements at some points, but no alterations on the overall pattern of friction occur.

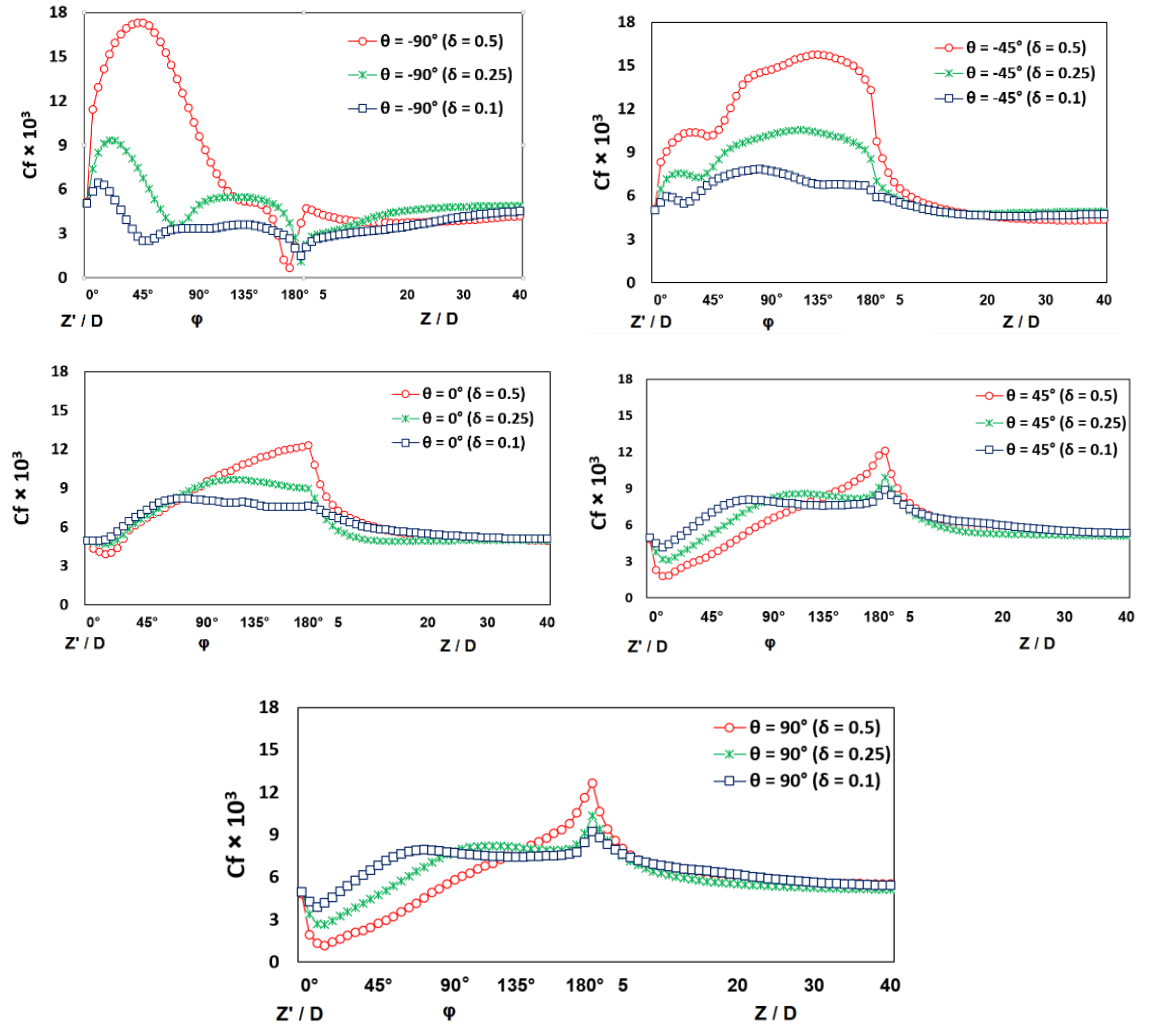


Fig. 2. 28 Comparison of friction coefficient of flow at $Re = 6 \times 10^4$ with the curvature ratios of 0.1, 0.25, and 0.5 along the bend and downstream

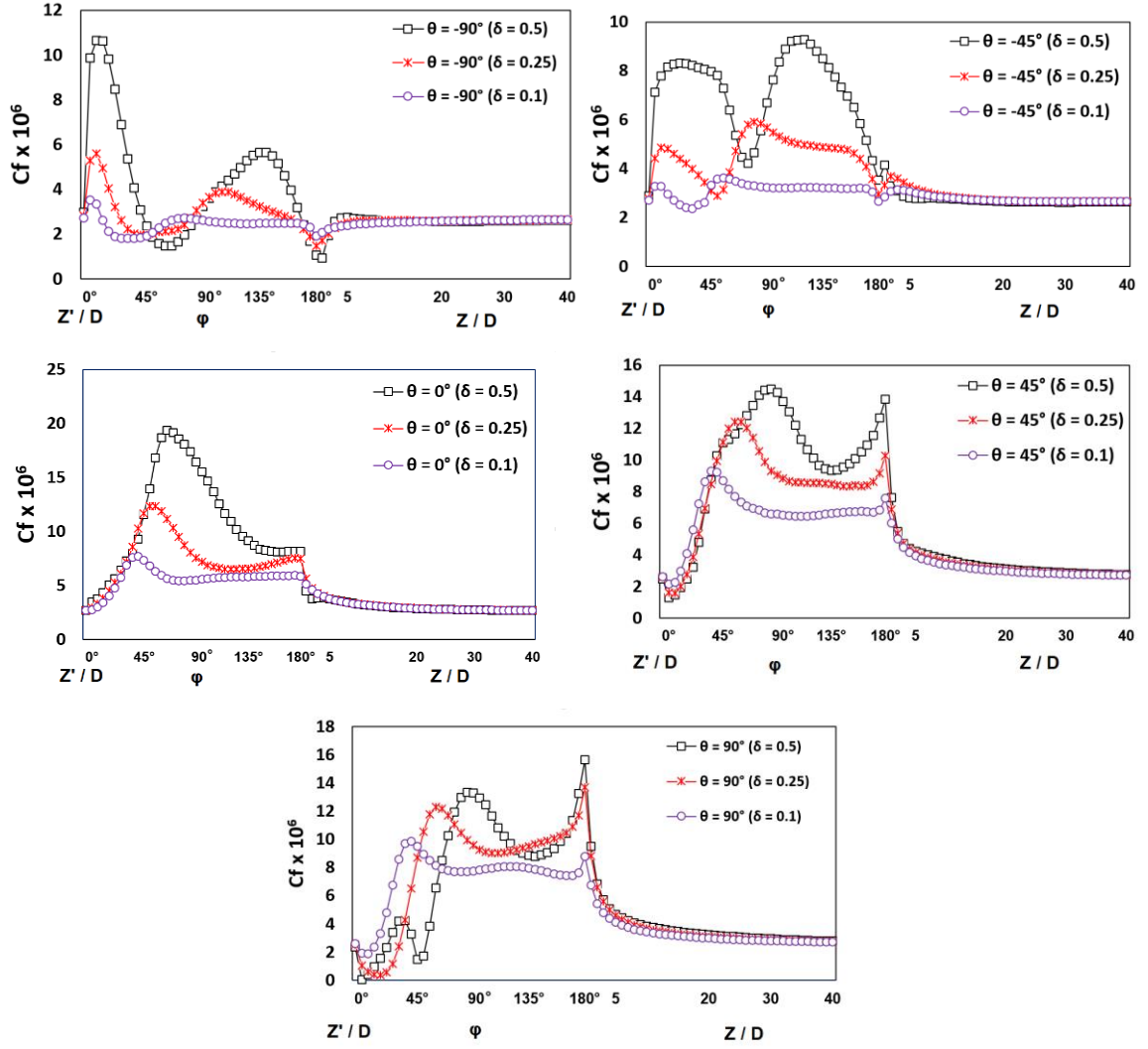
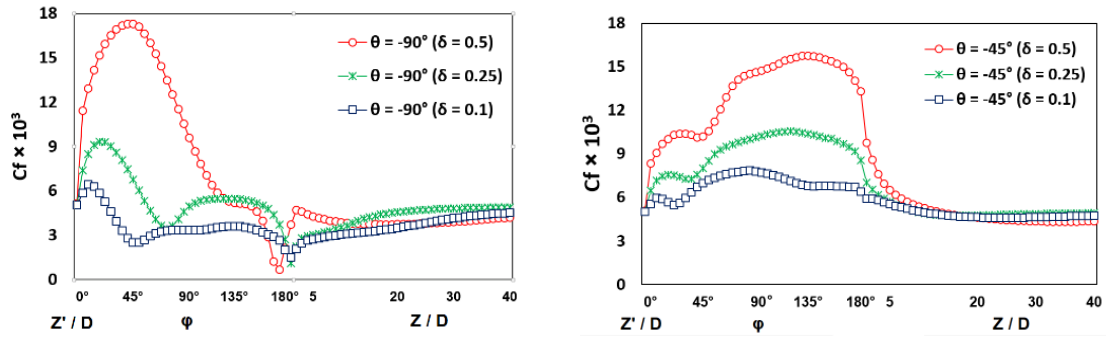


Fig. 2. 29 Friction coefficient of flow at $Re = 600$ with the curvature ratios of 0.1, 0.25, and 0.5 along the bend and downstream



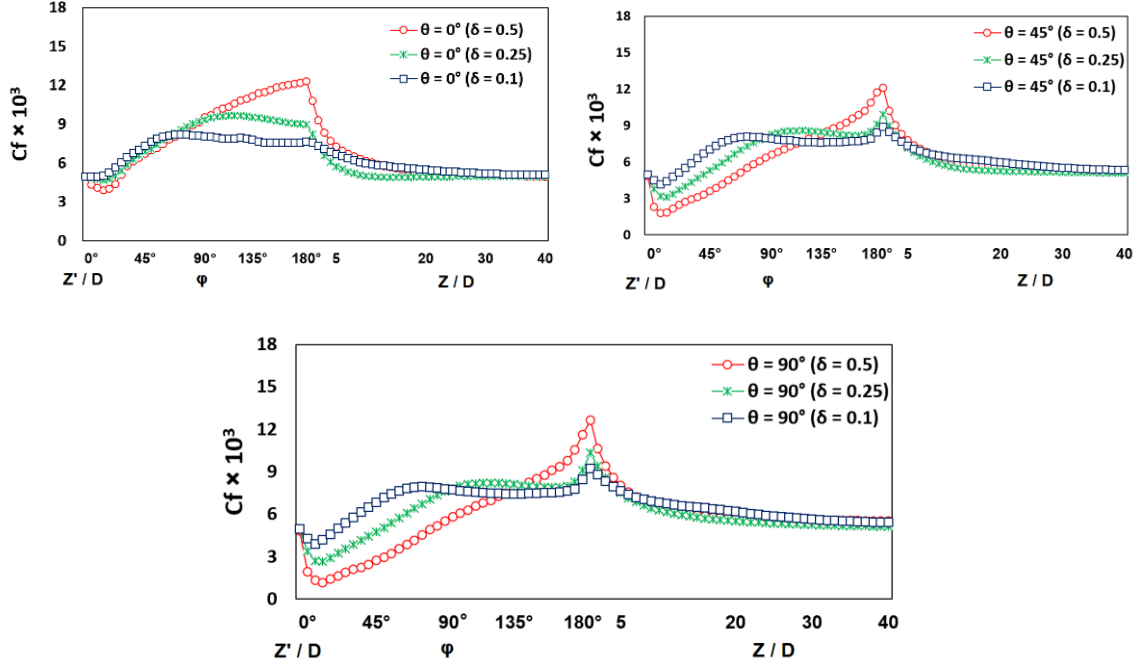


Fig. 2.30 Friction coefficient of flow at $Re = 6 \times 10^4$ with the curvature ratios of 0.1, 0.25, and 0.5 along the bend and downstream

2.5.10 Nusselt number and the total heat transfer

Considering the Nusselt number that is calculated based on the below function, it was observed that for the Reynolds number of 6×10^4 (Fig. 2.31-a), on an increase of Dean number, there is a prominent increase of Nusselt number in the inner wall of the bend as the peak of the fluid velocity is formed in the inner region. In the outer wall of the bend, however, the Nusselt number of the larger Dean number is smaller because of the deflection of the fluid momentum toward the inner wall which results in a lower velocity of the fluid in the outer region. Little before the flow goes past the 90-degree-bend, the Nusselt number of the highest curvature ratio increases as the flow starts gaining momentum near the outer wall.

In Fig 2.31-b which shows the Nusselt number of flow at $Re = 600$, unlike a high Reynolds number flow, no significant variation of Nusselt number occurs in the inner wall without regard to the change in the curvature ratio of the bend. However, the outer wall experiences a high Reynolds number, basically due to the shift of flow momentum toward the outer wall. Also, the Nusselt number in the outer wall increases when increasing Dean number.

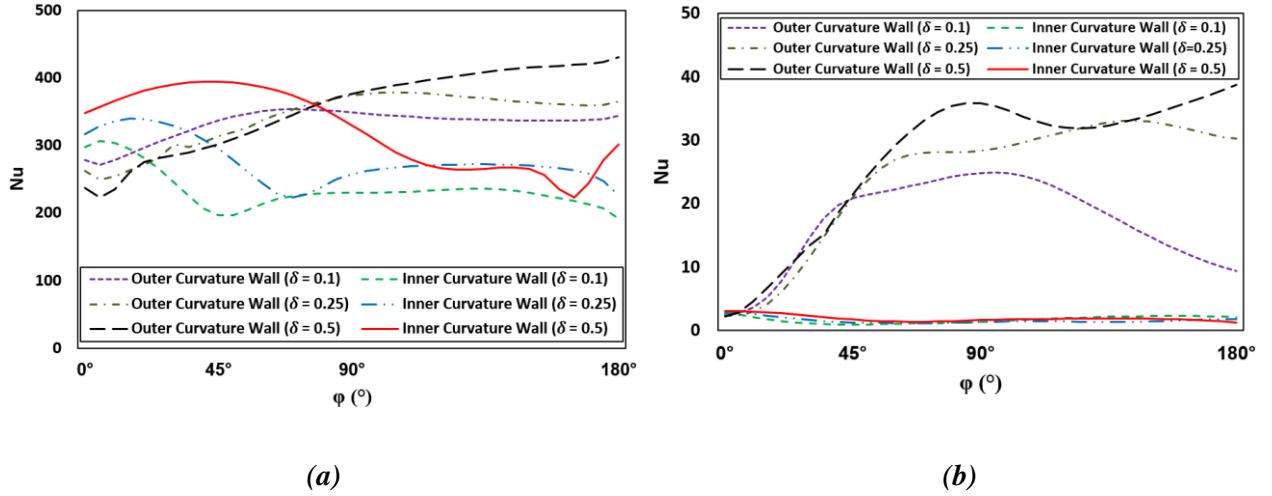


Fig. 2.31 Nusselt number of (a) the flow at $Re = 6 \times 10^4$ and (b) the flow at $Re = 600$ in the bend outer wall and inner wall

The total enthalpy of both flows ($Re = 6 \times 10^4$ and $Re = 600$) with the three curvature ratios in the U-bend system is shown in Fig. 2.32. The total enthalpy which is determined by the ratio of the total heat transfer rate and the heat transfer rate in the inlet, shows the dimensionless total heat transfer with respect to the heat transfer in the inlet. The results show that at a low Reynolds number, there is a larger heat transfer because when the Reynolds number is low, there is more residence time. Also, a comparison between the three curvature ratios shows that a smaller curvature ratio, results in a larger heat transfer, due to the fact that the bend with a smaller curvature ratio has more surface to travel inside the bend than a sharper bend. In the studied cases, for the Reynolds number of $Re = 6 \times 10^4$, when the curvature ratio of the bend is increased from 0.1 to 0.25, the total heat transfer is decreased by 8.1% and when the curvature ratio of the bend is increased from 0.25 to 0.5, the total heat transfer is decreased by 2.2%. Also, for the Reynolds number of $Re = 600$, when the curvature ratio is increased from 0.1 to 0.25, the total heat transfer is reduced by 3.6%, and when the curvature ratio is increased from 0.25 to 0.5, the overall heat transfer is reduced by 0.66%.

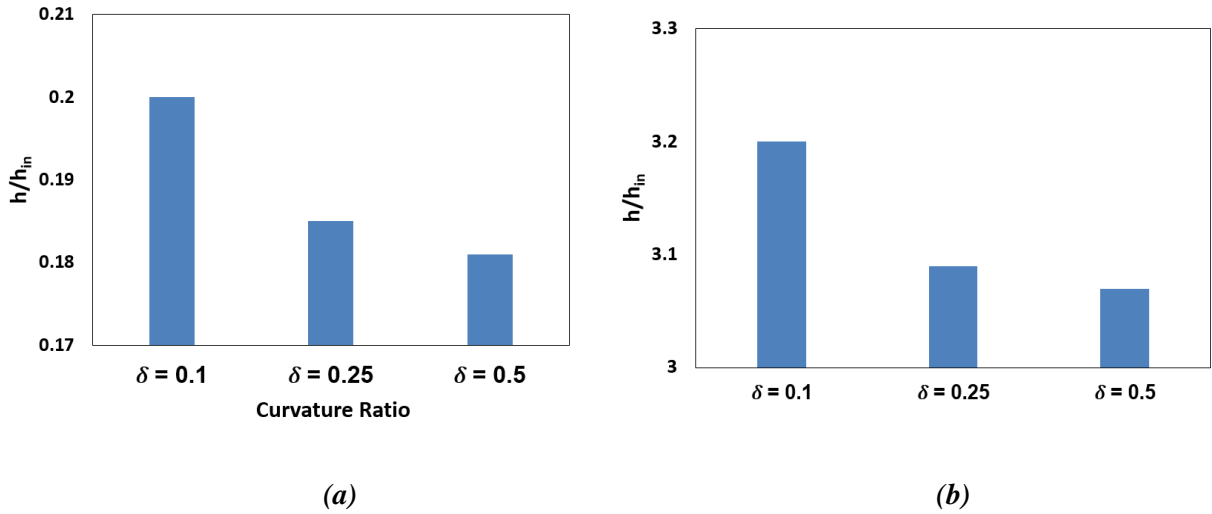


Fig. 2.32 Total heat transfer of flow at (a) $Re = 6 \times 10^4$ and (b) $Re = 600$ inside of the running fluid

With regard to the fact that the enhancement of Dean number leads to a drop of heat transfer, considering the total pressure loss of the U-bend system can be a good factor in designing the bend curvature. At $Re = 6 \times 10^4$, although $\delta = 0.1$ has the higher heat transfer, it has a low total pressure loss. $\delta = 0.5$ (sharpest bend), also, has a high total pressure loss, but the heat transfer is low. Meanwhile, for $\delta = 0.25$, even though the heat transfer is not as high as the $\delta = 0.1$ (8.1% lower), it has the lowest total pressure loss (up to 6.9%) among all the simulated cases, which makes it the right bend curvature.

For $Re = 600$, the increase of the bend curvature ratio brings about a 9% of lower total pressure loss and 4.3% of lower heat transfer. Hence, due to the existence of a desirable and undesirable phenomenon at the same time, studying other parameters which that make a specific bend curvature a better option need to be taken into consideration which is part of the future work of this study.

```

htc
{
    type          heatTransferCoeff;
    libs          ("libfieldFunctionObjects.so");
    field          T;
    patches        ("pipe_fluid_interface.*");
    htcModel       fixed;
    TRef           300;
}

```

2.5.11 Reynolds number effects

The overall conclusion of the effect of Reynolds number shows that the outlet temperature of the fluid decreases, and at higher Reynolds number, the outlet temperature takes less effect from the Reynolds number augmentation while there is a counter impact when enhancing the pipe length which is being discussed below.

The outlet temperature contours of flow at Reynolds numbers of 1×10^4 , 2×10^4 , 3×10^4 , 4×10^4 , 5×10^4 , and 6×10^4 which correspond to the Dean numbers of 0.5×10^4 , 1.0×10^4 , 1.5×10^4 , 2.0×10^4 , 2.5×10^4 , and 3.0×10^4 are shown in Fig. 2.31 and tabulated in Table 2.5.

Table 2.5 Model conditions of the U-bend system based on the change in Reynolds number

	Initial temperature (K)	Velocity (m/s)	Reynolds number	Dean number
Model 1	300	0.10	1.0×10^4	0.5×10^4
Model 2		0.19	2.0×10^4	1.0×10^4
Model 3		0.29	3.0×10^4	1.5×10^4
Model 4		0.39	4.0×10^4	2.0×10^4
Model 5		0.48	5.0×10^4	2.5×10^4
Model 6		0.58	6.0×10^4	3.0×10^4

Fig. 2.33 shows the temperature variations when increasing the Reynolds number at the heating mode of operation, where θ' is the dimensionless temperature, T_h is hottest temperature, T_c is the coldest temperature, and T_a is the ambient temperature. The fluid temperature is set to 300K in the inlet. This figure shows that the increase of Reynolds number from $Re = 1 \times 10^4$ to $Re = 6 \times 10^4$, reduces the temperature of fluid in the outlet from 318.2 K to 304.5 K. Meanwhile, the temperature is less affected by the change in Reynolds number. Also, the flow at a higher Reynolds number brings about heated fluid at the circumference of the pipe cross sections. Due to the fact that the flow is restricted by the bend and a recirculation happens at the bend exit, the fluid does not have a uniform distribution of temperature (Lyu et al. 2017).

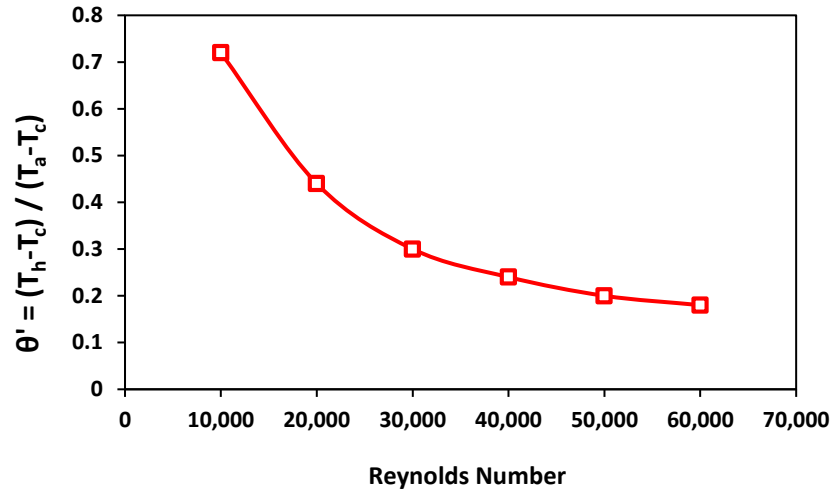


Fig. 2.33 The outlet temperature with the variation of Reynolds number

Reynolds numbers of $Re = 1 \times 10^4$, 2×10^4 , 3×10^4 , 4×10^4 , 5×10^4 , and 6×10^4 in the cooling mode of operation are also shown in Fig. 2.34. The initial temperature of the running fluid is 300K in the U-bend and the ambient temperature is 275K which makes equal the temperature difference compared with the heating mode. Having both heating and cooling modes into perspective, it is found that the heating mode of the U-bend has more impact on the outlet temperature of the running fluid than the cooling mode.

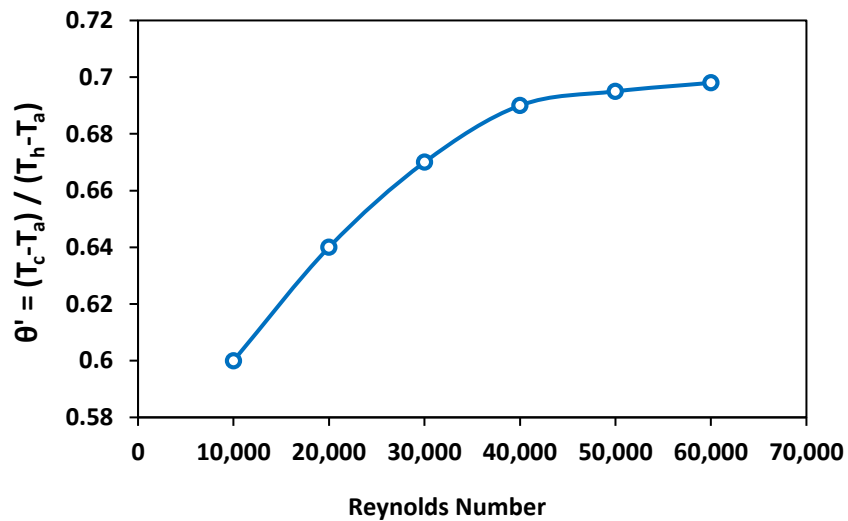


Fig. 2.34 Cooling rate and the temperature in the outlet with the variation of Reynolds number

2.5.12 U-bend Length

The outlet temperature contours of flow is demonstrated in Fig 2.35 which shows the fluid at the specific Reynolds number of 2×10^4 and the U-bend length of 4 m (38.5D), 7 m (67.3D), and 10 m (96.2D) as per Table 2.6. In Fig. 2.35, there is an overall increase of temperature when increasing the pipe length.

Table 2.6 U-bend length conditions

	U-bend length (m)	Initial temperature (K)	Initial Velocity (m/s)	Reynolds number	Dean number
Case 1	4m (38.5D _h)				
Case 2	7m (67.3D _h)	300	0.20	2.0×10^4	1.0×10^4
Case 3	10m (96.2D _h)				

With a comparative view on a number of Reynolds numbers and the overall outlet temperature at downstream lengths of 4 m (38.5D), 7 m (67.3D), and 10 m (96.2D), it is observed that the temperature of the fluid in the outlet increases at each specific Reynolds number when the pipe length increases (see Fig. 2.35). It is also inferred that a larger Reynolds number reduces the outlet temperature under the boundary conditions tabulated above. In this study, the outlet temperature is approximately increased by about 1.7 K/m.

As the heat extraction rate takes effect from the length of the U-bend system, it would be better to use a long U-bend heat exchanger. However, this brings with it higher installation costs and more pumping power. Hence, more research is required to overcome the costs associated with material use and installation for the purpose of shortening borehole length, which would be a part of the future work of this thesis.

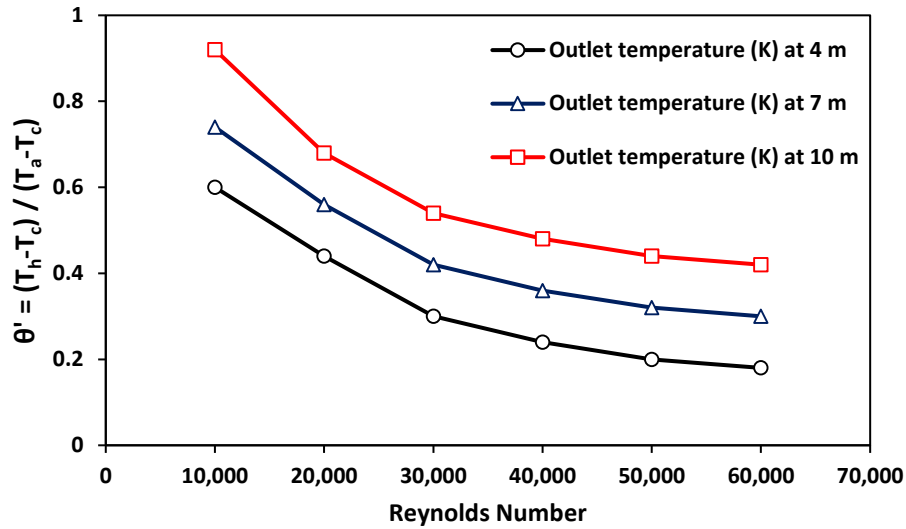


Fig. 2.35 Outlet temperature with the variation of Reynolds number

2.6 Conclusions

Curvature ratio effects:

The variations of pressure distribution are enhanced at a higher Dean number due to an increase in the bend curvature ratio. This is basically due to the fact that the pressure gradient that is generated to balance the centrifugal force is so large that the direction and the rate of pressure is deviated and increased toward the inner wall. The result is that the pressure in the inner wall becomes lower and the pressure in the outer wall becomes higher. Soon after the fluid flows into the downstream, the pressure variations are alleviated with a uniform trend until the outlet.

For the flow at $Re = 600$, however, the increase of the bend curvature ratio results in a consistent decrease of total pressure losses. This means that the consistent increase of curvature ratio reduces the amount of total pressure loss to a certain point.

At $Re = 6 \times 10^4$, there is a Dean number from which further increase or decrease of the curvature ratio, increases the total pressure loss. As a result, the curvature ratio must be regarded as an important parameter to study when designing a U-bend system.

Shortly after the fully developed flow at $Re = 600$ travels inside the bend, the generated centrifugal force impacts the incoming flow, resulting in a large pressure gradient in the space between the centerline and the outer wall to balance the centrifugal force. As a result, the momentum of flow is directed toward the outward region.

When the fully developed flow at $Re = 6 \times 10^4$ enters the bend inlet, there is a large shift of fluid momentum toward the inner wall due to the rapid and large formation of pressure gradient to balance the centrifugal force. This momentum displacement is stronger with longer durability with the curvature ratio augmentation until the fluid flows to the second half of the bend.

The shift of fluid momentum and the increase of velocity near the inner wall or the outer wall impacts the wall shear rates, normal vorticity, and the heat transfer coefficient directly, as a result, the friction coefficients, vorticity, and the Nusselt number increase on the walls where there is an increase of velocity.

The flow at a low Reynolds number has a better total heat transfer due to a higher residence time. However, this betterment of heat transfer happens at the cost of a high total pressure loss. Also, selecting the right bend curvature can contribute to improving the performance of the U-bend system.

Reynolds number and U-bend length:

The increase of Reynold number (Dean number) decreases the outlet temperature. Also, at high Reynolds number, the outlet temperature takes less effect from the Reynolds number augmentation.

In the heating mode of operation, the increase in the U-bend length increases the temperature in the outlet of the U-bend system as well as the amount of heat that is

extracted. However, the outlet temperature is decreased when increasing the Reynolds number and that results in the enhancement of the heating rate.

2.7 References

- Akbarinia, A. 2008. "Impacts of Nanofluid Flow on Skin Friction Factor and Nusselt Number in Curved Tubes with Constant Mass Flow." *International Journal of Heat and Fluid Flow* 29(1): 229–41.
- Beier, R. A., J. Acuña, P. Mogensen, and B. Palm. 2014. "Transient Heat Transfer in a Coaxial Borehole Heat Exchanger." *Geothermics* 51: 470–82.
- Biglarian, H., M. Abbaspour, and M. H. Saidi. 2017. "A Numerical Model for Transient Simulation of Borehole Heat Exchangers." *Renewable Energy* 104: 224–37.
- Choi, J., and Y. Zhang. 2012. "Numerical Simulation of Laminar Forced Convection Heat Transfer of Al₂O₃–Water Nanofluid in a Pipe with Return Bend." *International Journal of Thermal Sciences* 55: 90–102.
- Chung, J. T., and J. Min Choi. 2012. "Design and Performance Study of the Ground-Coupled Heat Pump System with an Operating Parameter." *Renewable Energy* 42: 118–24.
- Cvetkovski, Christopher G., Stanley Reitsma, Tirupati Bolisetti, and David S. K. Ting. 2015. "Heat Transfer in a U-Bend Pipe: Dean Number versus Reynolds Number." *Sustainable Energy Technologies and Assessments* 11: 148–58.
- Cvetkovski, C. G., S. Reitsma, T. Bolisetti, and D. S.-K. Ting. 2014. "Ground Source Heat Pumps: Should We Use Single U-Bend or Coaxial Ground Exchanger Loops?" *International Journal of Environmental Studies* 71(6): 828–39.
- Dean, W. R., "Note on the motion of fluid in a curved pipe," *The London, Edinburgh, and Dublin Philosophical Magazine and Journal of Science*, vol. 4, pp. 208-223, 1927.
- Dean, W. R., "LXXII. The stream-line motion of fluid in a curved pipe (Second paper)," *The London, Edinburgh, and Dublin Philosophical Magazine and Journal of Science*, vol. 5, pp. 673-695, 1928.

- Dutta, P., S. Kumar Saha, N. Nandi, and N. Pal. 2016. "Numerical Study on Flow Separation in 90° Pipe Bend under High Reynolds Number by K- ϵ Modelling." *Engineering Science and Technology, an International Journal* 19(2): 904–10.
- Gao, X., H. Zhang, J. Liu, B. Sun, and Y. Tian. 2018. "Numerical Investigation of Flow in a Vertical Pipe Inlet/Outlet with a Horizontal Anti-Vortex Plate: Effect of Diversion Orifices Height and Divergence Angle." *Engineering Applications of Computational Fluid Mechanics* 12(1): 182–94.
- Javadi, H., S. S. Mousavi Ajarostaghi, M. A. Rosen, and M. Pourfallah. 2019. "Performance of Ground Heat Exchangers: A Comprehensive Review of Recent Advances." *Energy* 178: 207–33.
- Kalpakli Vester, A., R. Örlü, and P. Henrik Alfredsson. 2016. "Turbulent Flows in Curved Pipes: Recent Advances in Experiments and Simulations." *Applied Mechanics Reviews* 68(5): 050802-050802–25.
- Kalpakli, A. 2012. "Experimental Study of Turbulent Flows through Pipe Bends." <http://urn.kb.se/resolve?urn=urn:nbn:se:kth:diva-93316> (August 8, 2019).
- "K-Epsilon — SimScale Documentation." <https://www.simscale.com/docs/content/simulation/model/turbulenceModel/kEpsilon.html> (December 2, 2019).
- Kim, J., M. Yadav, and S. Kim. 2014. "Characteristics of Secondary Flow Induced by 90-Degree Elbow in Turbulent Pipe Flow." *Engineering Applications of Computational Fluid Mechanics* 8(2): 229–39.
- Kummert, M., M. Bernier, A. Costa, and J. Paris. 2007. "A Comparison between Geothermal Absorption and Compression Heat Pumps for Space Conditioning." *International Journal of Environmental Studies* 64(4): 467–87.
- Lyu, Z., X. Song, G. Li, X. Hu, Y. Shi, Zh. Xu. 2017. "Numerical Analysis of Characteristics of a Single U-Tube Downhole Heat Exchanger in the Borehole for Geothermal Wells." *Energy* 125: 186–96.
- Maestre, I. R., F. J. González Gallero, P. Álvarez Gómez, and L. Pérez-Lombard. 2015. "A New RC and G-Function Hybrid Model to Simulate Vertical Ground Heat Exchangers." *Renewable Energy* 78: 631–42.

- Noorani, A., G. K. El Khoury, and P. Schlatter. 2013. "Evolution of Turbulence Characteristics from Straight to Curved Pipes." *International Journal of Heat and Fluid Flow* 41: 16–26.
- Ramadan, A. S. 2016 "Parametric Study of Vertical Ground Loop Heat Exchangers for Ground Source Heat Pump Systems."
- Song, X., Y. Shi, G. Li, R. Yang, Zh. Xu, R. Zheng, G. Wang, Z. Lyu. 2017. "Heat Extraction Performance Simulation for Various Configurations of a Downhole Heat Exchanger Geothermal System." *Energy* 141: 1489–1503.
- Sudo, K., M. Sumida, and H. Hibara. 1998. "Experimental Investigation on Turbulent Flow in a Circular-Sectioned 90-Degree Bend." *Experiments in Fluids* 25(1): 42–49.
- Sudo, K., M. Sumida, and H. Hibara. 2000. "Experimental Investigation on Turbulent Flow through a Circular-Sectioned 180° Bend." *Experiments in Fluids* 28(1): 51–57.
- Younis, M., T. Bolisetti, and D. S.-K. Ting. 2010. "Ground Source Heat Pump Systems: Current Status." *International Journal of Environmental Studies* 67(3): 405–15.

CHAPTER 3 – The effects of center-in versus annulus-in flow, bucket space length, and Reynolds number on the performance of coaxial heat exchangers

3.1 Introduction

Geothermal heat exchanger is a promising technology which can help mitigating the climate change challenge (Van der Zwaan and Dalla Longa 2019). Particularly in recent years, the coaxial configuration is gaining significant attention. This coaxial configuration promises consequential improvement in the performance of the borehole heat exchanger. Specifically, some studies (Cvetkovski et al. 2014 and Song et al. 2018) indicate that coaxial borehole heat exchanger (CBHE) can lead to better heat transfer and less total pressure loss compared to its conventional counterpart, U-bend heat exchanger. For cooling applications where heat is injected into the ground, Iry and Rafee (2019) found that an inner-outer diameter ratio of 0.65 resulted in the best thermal performance for the range of conditions they studied. This concurred with an earlier study by Yekoladio et al. (2013), who discovered that a diameter ratio of 0.65 led to the lowest pressure drop. It should be noted that the optimal diameter ratio is a function of parameters such as pipe length and inner pipe conductivity. The inner pipe conductivity becomes progressively more important as the length of the conduit increases. Considerable thermal short-circuiting can occur when the pipe is long (Zanchini et al., 2010). Therefore, for better performance it is important to keep the inner pipe conductivity low for long borehole (Pan et al., 2019).

Li et al (2020), carried out a numerical test, and studied the effects of different types of inner pipes. One finding was that when the thermal conductivity of the inner pipe is small, there will be a small heat loss. Also, the heat transfer is improved when enhancing the thermal conductivity of the inner pipe in the case of annulus-in flow.

In the present study, it is aimed to observe the center-in and annulus-in flow effects on equal hydraulic diameters to provide a better understanding about pipe flow and heat transfer performance. Also, the effects of bucket space height (the distance between the center pipe and the bottom of CBHE) is studied. Finally, the impacts of Reynolds numbers of 2×10^3 , 1×10^3 , and 2×10^4 on the performance of the system is presented and discussed.

3.2 Coaxial Heat Exchanger Model

Fig. 3.1 shows the laboratory-scale experimental model of Gordon et al (2018). The pipe material is hdpe with a thermal conductivity of $0.33 \text{ W/(m} \cdot \text{K)}$ and a specific heat of $2500 \text{ J/(kg} \cdot \text{K)}$. The borehole length is 4 m long. The inner diameter of the outer pipe is 5.54 cm with a pipe thickness of 0.23 cm and a hydraulic diameter of 2.54 cm. The 3.97 m long inner pipe has an inner diameter (hydraulic diameter) of 2.54 cm and a thickness of 0.23 cm. The temperature of the borehole wall is assumed to be constant ($T = 291.75\text{K}$).

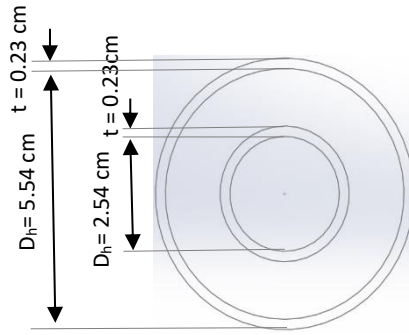


Fig. 3.1 Schematic diagram of coaxial heat exchanger, cross sectional view

3.3 Numerical Simulation

As it is shown in Fig. 3.2, an axisymmetric wedge along the pipe has been developed by two planes along the axis. In case of 2D pipes, the rotation angle must be less than 5 degrees with the thickness of one cell as per (Wedge n.d.). In this study, the specified wedge has a two-degree rotation. The developed wedge consists of the inner pipe, outer pipe, fluid inside the inner pipe, fluid inside the annulus, and the bucket space. Quadrilateral meshing was selected with thin biases near the pipe-fluid walls.

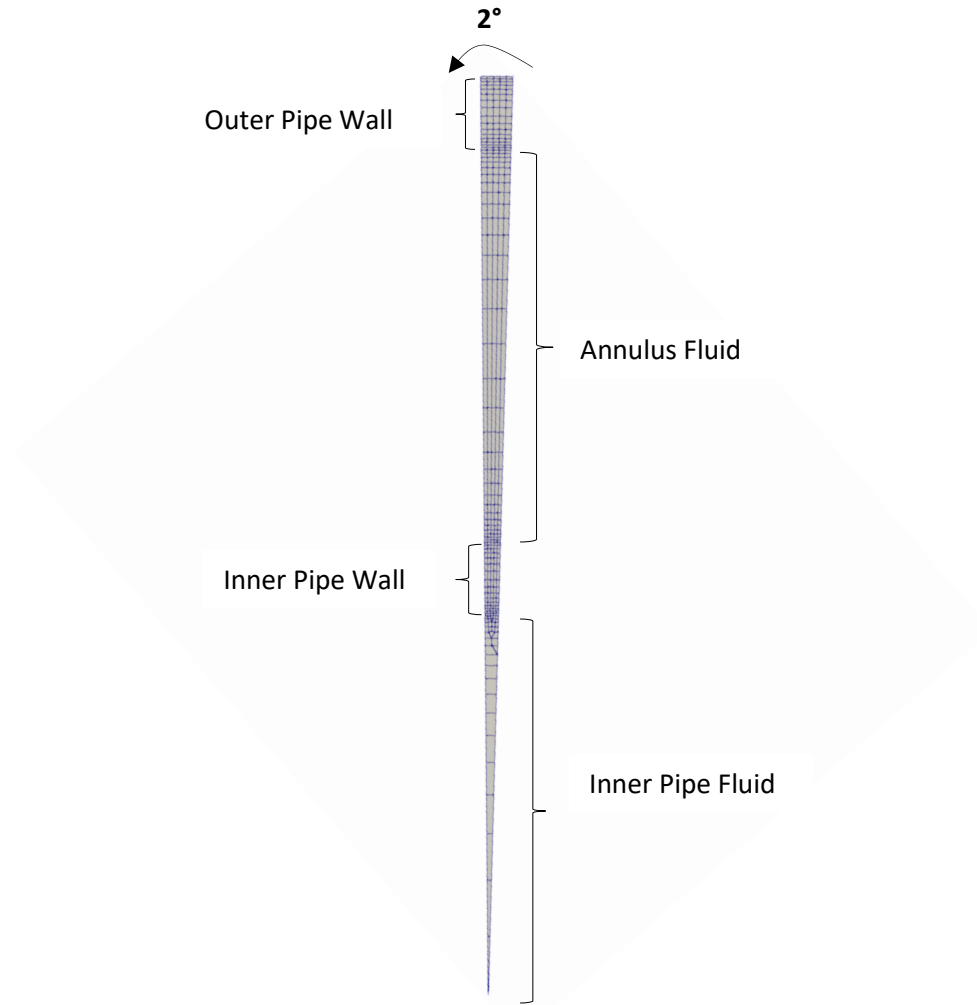


Fig. 3.2 Wedge of the computational grid in axisymmetric plane

OpenFOAM v.5, an open source CFD software, is used to carry out all simulations in this study. This software solves the Navier-Stokes and energy equations that are discretized in the form of cell centered volume method. The semi-implicit method for pressure-linked equation (SIMPLE) algorithm is adopted to do the iterative numerical simulations with SST $k-\omega$ turbulence model due to the existence of separation. The convergence criteria of all governing equations are set to 10^{-6} .

3.3.1 Governing Equations

Mass conservation or continuity equation for the incompressible fluid, water, is as follows:

$$\vec{\nabla} \cdot \vec{\vartheta} = 0 \quad (3.1)$$

The momentum conservation of Navier-Stokes equations in forced convection and incompressible flows is as follows:

$$(\vec{\vartheta} \cdot \vec{\nabla}) \vec{\vartheta} = -\frac{1}{\rho} \vec{\nabla} p + \vec{\nabla} \cdot (\nu \vec{\nabla} \vec{\vartheta}) + \vec{g} \quad (3.2)$$

where p is the pressure, ν is the kinematic viscosity, and \vec{g} is the body on the continuum due to an external force (gravitational acceleration).

Energy Equation:

$$\frac{\partial}{\partial t} (\rho E) + \frac{\partial}{\partial x_i} [u_i (\rho E + p)] = \frac{\partial}{\partial x_j} \left(k_{eff} \frac{\partial T}{\partial x_j} + u_i (\tau_{ij})_{eff} \right) + S_h \quad (3.3)$$

$$(\tau_{ij})_{eff} = \mu_{eff} \left(\frac{\partial u_j}{\partial x_i} + \frac{\partial u_i}{\partial x_j} \right) - \frac{2}{3} \mu_{eff} \frac{\partial u_k}{\partial x_k} \delta_{ij}$$

$$k_{eff} = k + \frac{c_p \mu_t}{Pr_t}$$

where E is the total transported energy, and S_h is the volumetric heat source. $(\tau_{ij})_{eff}$ is the effective deviatoric stress tensor. k_{eff} denotes the effective thermal conductivity, k is the thermal conductivity of the fluid, and Pr_t is Prandtl number.

Transport Equations for the SST k - ω model as per (Zanchini et al. 2010) and (Li et al. 2020):

$$\frac{\partial}{\partial t} (\rho k) + \frac{\partial}{\partial x_i} (\rho k u_i) = \frac{\partial}{\partial x_j} \left(\Gamma_k \frac{\partial k}{\partial x_j} \right) + \tilde{G}_k - Y_k + S_k \quad (3.4)$$

$$\frac{\partial}{\partial t} (\rho \omega) + \frac{\partial}{\partial x_i} (\rho \omega u_i) = \frac{\partial}{\partial x_j} \left(\Gamma_\omega \frac{\partial \omega}{\partial x_j} \right) + G_\omega - Y_\omega + D_\omega + S_\omega \quad (3.5)$$

where Γ_k is the effective diffusivities of k , \tilde{G}_k is the generation of k , Y_k is the dissipation of k due to turbulence, and S_k is the source terms. Also, Γ_ω represent the effective

diffusivities of ω , G_ω denotes the generation of ω , Y_ω is the dissipation of ω , and S_ω is the source terms.

3.3.2 Boundary Conditions

A steady, uniform flow enters either the inner pipe or the annulus between the two pipes with the velocity as per Table 3.1. The effects of center-in and annulus-in flow as well as the inner pipe length are studied at one specific Reynolds number ($Re = 20,000$). Only the part related to the effects of Reynolds number has the velocity differences. The reason for selecting these Reynolds numbers with a considerable difference is to find the overall trend of flow and heat transfer due to the change in the velocity of flow when using different pumping systems with different pumping powers.

According to Table 3.2, the velocity in the inlet is fixedValue, which is a fixed value constraint. The velocity next to a wall is set to noSlip boundary condition which applies the fixedValue constraint of zero velocity, and it is zeroGradient at the outlet port. This boundary condition sets a zero-gradient of a specific parameter from the patch internal field to the patch faces. Also, OutletInlet boundary condition provides a generic inflow with the outflow when there is reverse flow. A specific wall function is set for each turbulent parameter in the fluid-pipe walls. And each plane of the developed wedge provides a cyclic condition between the plane boundaries with wedge constraint. The below equations are used to determine the turbulent properties of SST k- ω . The calculated values are presented in Table 3.3.

Reynolds Number:

$$Re = \frac{\text{Inertia Forces}}{\text{Viscous Forces}} = \frac{\rho U D_h}{\mu} \quad (3.6)$$

where ρ is the density of the fluid, U is the velocity in the inlet, D_h is the pipe hydraulic diameter, and μ is the dynamic viscosity of the fluid.

The turbulent Kinetic energy:

$$k = \frac{3}{2} (UI)^2 \quad (3.7)$$

where U is the velocity in the inlet, and I is the turbulent intensity that is set as 1% in the inlet.

Turbulent length scale:

$$l = 0.5D_h \quad (3.8)$$

Turbulent dissipation rate

$$\omega = (C_\mu)^{-1/4} \frac{\sqrt{k}}{l} \quad (3.9)$$

where C_μ is the empirical constant used in for turbulent flow which is approximately equal to 0.009

The turbulent viscosity:

$$\frac{\mu_t}{\mu} = \frac{\rho k}{\mu \omega} \quad (3.10)$$

Table 3.1 Input parameters of the hydrodynamic simulation tests

	Numerical Models
Material	Water
Density (kg/m ³)	998.2
Thermal conductivity (W/m·K)	0.60
Specific heat (J/kg · K)	4200
Dynamic Viscosity (P)	0.001003
	0.08
Velocity (m/s)	0.4
	0.8
Temperature (K)	303.15

Table 3.2 Boundary conditions parameters

	inlet	outlet	pipe_fluid_interface
U	fixedValue	zeroGradient	noSlip
p	zeroGradient	fixedValue	zeroGradient
T	fixedValue	OutletInlet	Compressible::turbulentTemperatureCoupledBaffleMixed
ε	fixedValue	zeroGradient	epsilonWallFunction
k	fixedValue	zeroGradient	kqRWallFunction
μ	calculated	calculated	nutkWallFunction

Table 3.3 Conditions for SST k- ω

Turbulent parameters			
Reynolds Number	2×10^3	1×10^4	2×10^4
Turbulence Intensity (%)	1	1	1
Turbulent Kinetic Energy (m^2/s^2)	3.6×10^{-5}	6×10^{-4}	2×10^{-3}
Turbulent Dissipation (m^2/s^3)	8.3×10^{-6}	5.6×10^{-4}	3.5×10^{-3}
Turbulence Viscosity Ratio	1.005×10^{-6}	1.005×10^{-6}	1.005×10^{-6}
Turbulence Length Scale (m)	0.0127	0.0127	0.0127

3.3.3 Model Domain

Prior to running the simulations, the input parameters (i.e. the fluid density, viscosity, velocity in the inlet, and turbulent properties) were determined and contributed to the completion of the model setup to study the flow and thermal behavior and some characteristics of it in the coaxial piping configuration without radiation occurrences based on Equations 3.6 to 3.10 that were presented earlier in this chapter. In this study, in addition to simulating Gordon et al.'s (2018) test conditions, two additional models are developed with an increase in the Reynolds number to compare the results based on the increment of Reynolds number. Table 3.1 shows the input parameters of the hydrodynamic simulation for all simulated cases.

3.3.4 Model Verification and Validation

The grid independency test is carried out to determine the mesh size along the stream direction. Given the measured outlet temperature (T_{out}), 5.7×10^5 mesh sizing satisfies the independency to mesh (see Fig. 3.3). Also, the outlet temperature of the simulated model which was 298K was found to be about 0.67% of deviation from the experimental output that was measured to be 300 K by (Gordon et al. 2018).

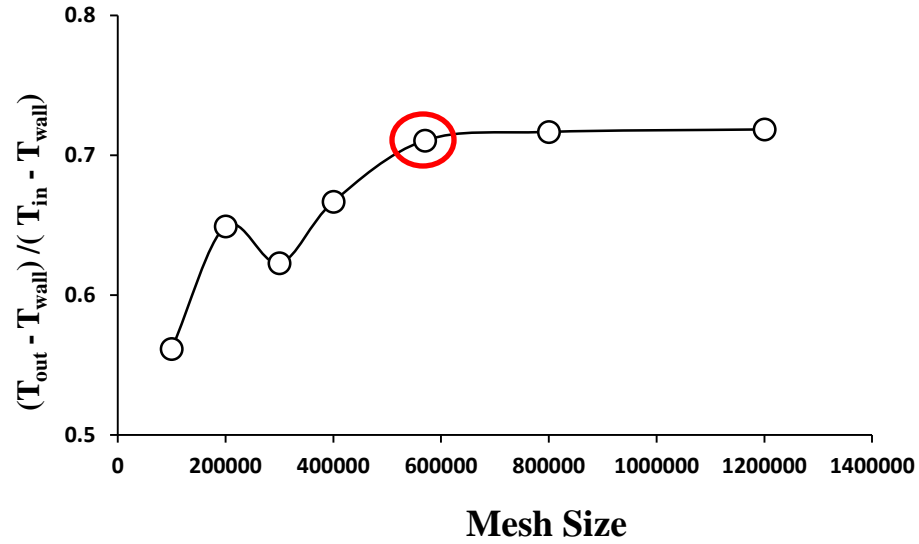


Fig. 3.3 Temperature against mesh sizing

3.4 Results

The results concerning the center-in flow versus the annulus-in flow, the length of the bucket space, as well as the Reynolds number effects on the total pressure loss and the heat transfer are presented as follows:

3.4.1 Center-in vs. Annulus-in Flow Directions

Having both center-in and annulus-in flows into perspective, it is found that the amount of total pressure loss in the case of annulus-in flow is dramatically larger than the center-in flow, however, the heat transfer of the center-in flow is 5.7% smaller. This makes center-in flow systems a more suitable case at the cost of a smaller heat transfer.

Pressure distribution and pressure drop

The way the bottom of the borehole affects the pressure of the flow differs completely when changing the flow inlet from the center pipe to the annulus. When the flow is introduced through the inner pipe or the annulus, the pressure drop in the center-in flow case is less than the pressure drop of the annulus-in flow at the bottom of the borehole (see Fig. 3.4) due to the fact that the flow in the bucket space coming from the center pipe resists to enter the bounded region between the inner pipe and the outer pipe while the incoming flow from in the annulus-in case which is restricted to the bounded region

between the center pipe and the annulus is accompanied by an expansion which leads to a large drop of pressure.

Fig. 3.4-a shows the pressure drop in the inner pipe and the annulus space for both center-in and annulus-in flow directions which is determined based on the value of the mass flow average of the total pressure demonstrated in Eq. 3.11 where ρ is the fluid density, \dot{m} is the mass flow rate of the running fluid, \vec{u} is the velocity vector and A is the area. It is observed that in either of the flow directions, the pressure in the inner pipe drops more than the pressure in the annulus space. Also, comparing both flow directions in Fig. 3.4-b shows that the amount of total pressure loss in the annulus-in flow case is larger than the center-in flow direction. As per Fig. 3.5 which shows the pressure in the bucket space, the reason for a larger total pressure loss for the annulus-in flow is the large drop of pressure when the flow in the bounded region between the inner pipe and the outer pipe is expanded when it reaches the bucket space and finds a way out to the inner pipe. In the case of center-in flow, when the fluid reaches the bucket space, it is restricted to the bounded region between the inner pipe and the outer pipe as it enters downstream, which leads to less pressure drop.

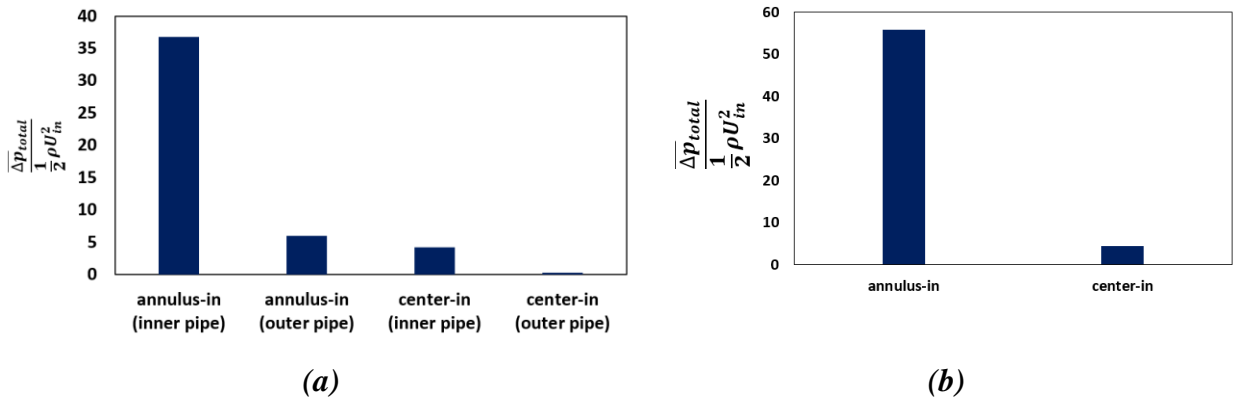


Fig. 3.4 (a) Pressure drop of center-in and annulus-in flows in the inner pipe and the annulus and (b) Total pressure loss coefficient of center-in and annulus-in flows between the inlet and outlet

$$\bar{p}_t^M = \left(\frac{\rho}{\dot{m}}\right) \int_A p_t (\vec{u} \cdot \vec{n}) dA \quad (3.11)$$

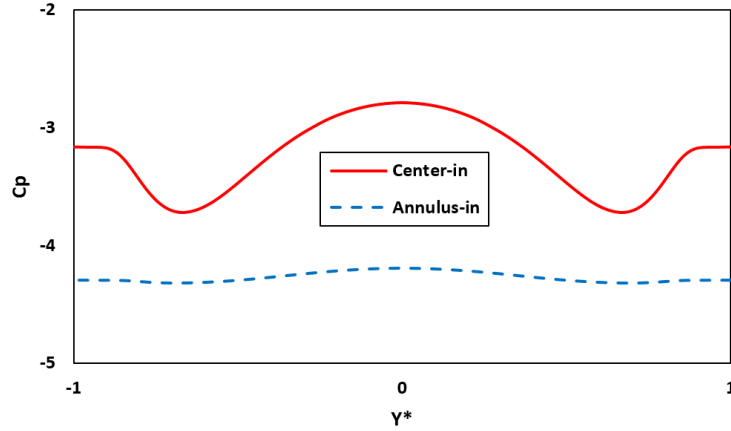


Fig. 3.5 Pressure coefficient ($C_p = \frac{P - P_{in}}{\frac{1}{2}\rho U_0^2}$) of the center-in and annulus-in flow models against end cap walls ($Y^* = Y/D_{io}$)

In the center-in case, once the flow reaches the bottom of the borehole, the pressure begins to increase, and a local peak at the center of the end cap surface is formed (see Fig. 3.6-a). In the bucket space (the space between the inner pipe and the outer pipe end), the pressure gradient which defines the rate and the direction of pressure, increases, especially near the bottom of the borehole corners where the flow return occurs (see Fig. 3.7-a)

When the flow is introduced through the center pipe, the pressure of the return flow in the annulus space increases in the initial downstream distances until about $X / D_h = 3$. From this point until the downstream outlet, there is a reduction of pressure. In the annulus-in case, however, the pressure at the bottom of the borehole in the bucket space is distributed almost uniformly. The uniformity of pressure shown in Fig. 3.6-b as well as the formation of a pair of vortices ring in the bucket space (see Fig. 3.14), which will later be discussed, causes a sharp flow turn toward the inner pipe. The result is a large pressure gradient and a flow separation at the edge of the inner pipe (See Fig. 3.7-b) as well as a large reduction of pressure in the initial downstream distances. As the flow moves along the downstream, the large reduction of pressure alleviates. Thus, there is a gradual decrease of pressure until the outlet.

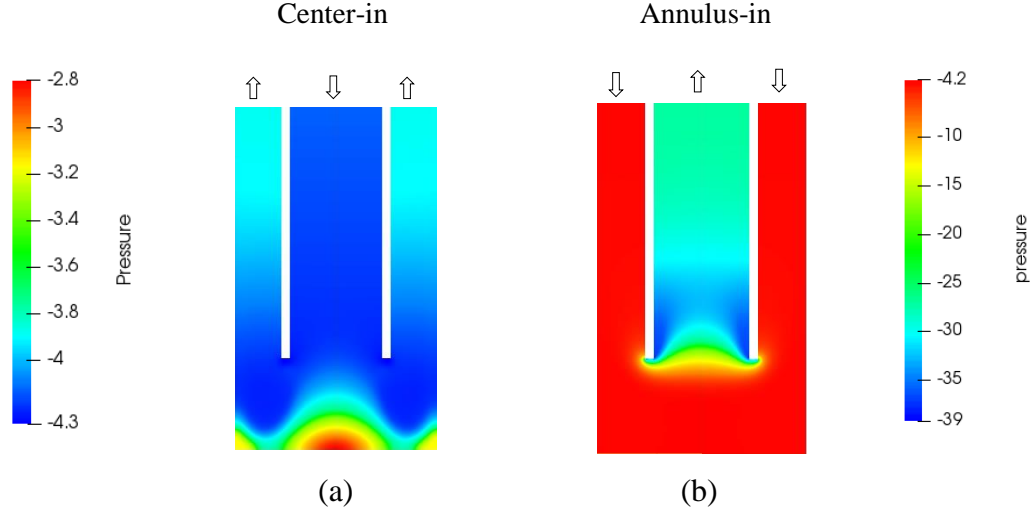


Fig. 3.6 The pressure contours of the center-in and the annulus-in flow at the bottom of the borehole demonstrated in a dimensionless form ($\frac{\Delta P}{\frac{1}{2}\rho U_0^2}$)

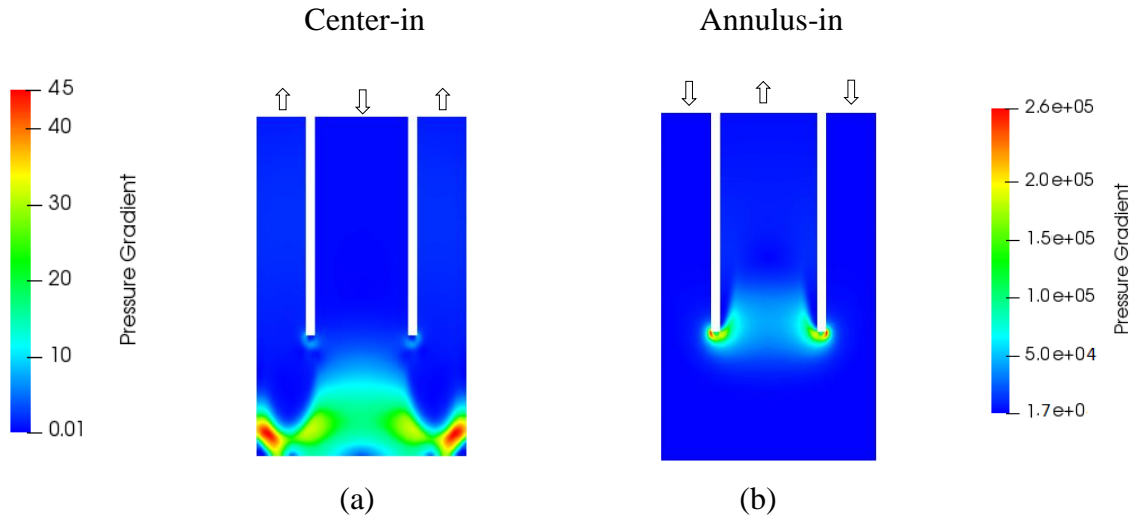


Fig. 3.7 Dimensionless local pressure gradient contours of the center-in and the annulus-in flow at the bottom of the borehole with respect to the inlet pressure gradient.

The pumping power which is defined by the total pressure loss, mass flow rate, and fluid density based on Eq. 3.12 shows that even with equal velocities in the inlet, the center-in flow case requires less pumping power compared to the annulus-in flow, because it has less total pressure loss as the cross sectional area of the running fluid in the inlet surface of the annulus is larger than the inner pipe surface. Therefore, as the center-in flow requires less pumping power at equal hydraulic diameters and initial velocities, another geometrical

characteristic, i.e. the position of the center pipe in relation to the end cap surface may be one parameter in enhancing the performance of the borehole which will be discussed later in this chapter.

$$W_{pump} = \frac{\Delta P_{total} \times \dot{m}}{\rho} \quad (3.12)$$

Heat transfer

To determine the energy flow per unit area on the end cap, heat flux is calculated based on Eq. 3.13 and shown in Fig. 3.8. The heat flux pattern in both center-in and annulus-in flows is almost the same. For both cases, there is a reduction of heat flux from the cap corners as we move toward the center. However, the heat flux of the center-in flow demonstrates about 4.5% better heat transfer performance compared to the annulus-in case.

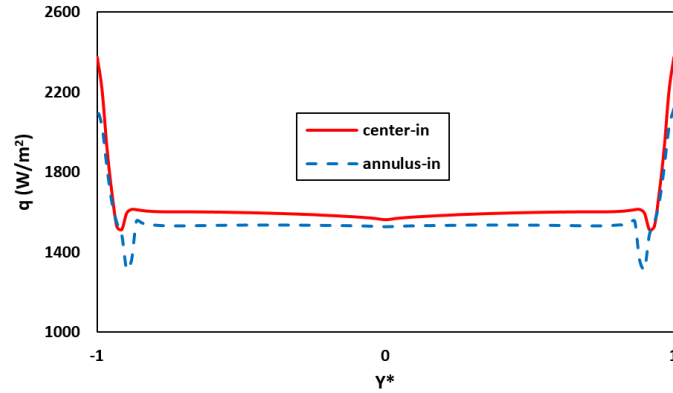


Fig. 3.8 Pipe wall heat flux against the end cap surface ($Y^* = Y/D_{10}$)

Fig. 3.9-a shows the heat flux along the pipe and the end cap surface. It is found that the heat flux on the end cap surface for the center-in flow is about 4.2% better than the annulus-in flow, however, the heat flux on the outer pipe surface of the annulus-in flow is about 7.1% better than center-in flow. Also, the total heat flux shown in Fig. 3.9-b of the annulus-in flow indicates almost 3% betterment of heat flux compared to the center-in flow. This betterment can also be observed when comparing the enthalpy of both center-in and annulus-in cases based on Eq. 3.14. The results shown in Fig. 3.10 shows about 5.7% improvement of the overall heat transfer of the annulus-in flow compared to the center-in flow.

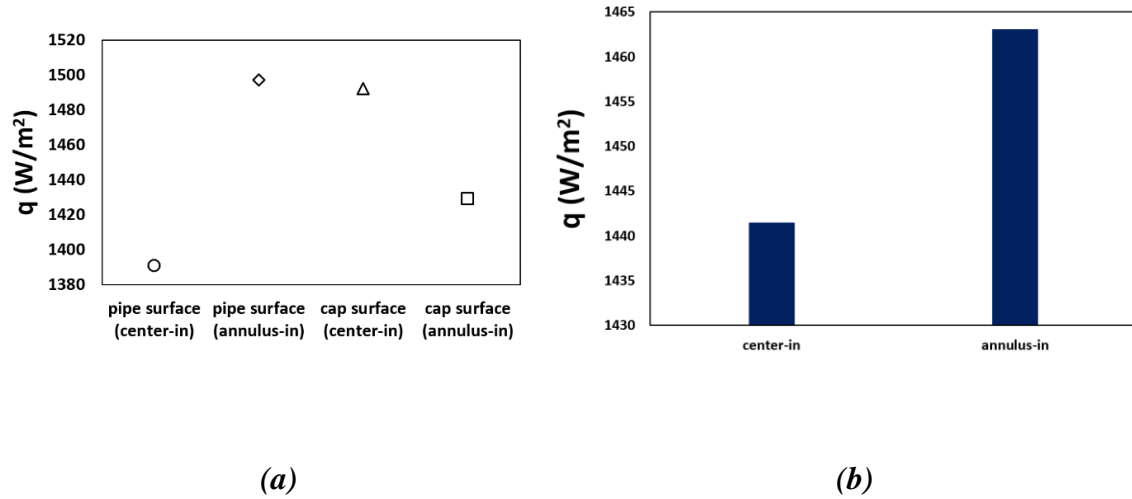


Fig. 3.9 (a) Averaged Heat flux along the pipe and the end cap surfaces for the center-in and annulus-in flow directions. And (b) Total heat flux for the center-in and annulus-in flow directions

$$q = (T_a - T_p) \times (1.0/h + \text{totalSolidRes}) \quad (3.13)$$

where q is the heat flux per unit area, T_a is the constant outer pipe wall, T_p is the interface temperature, h is the heat transfer coefficient and totalSolidRes is the sum of thermal resistance

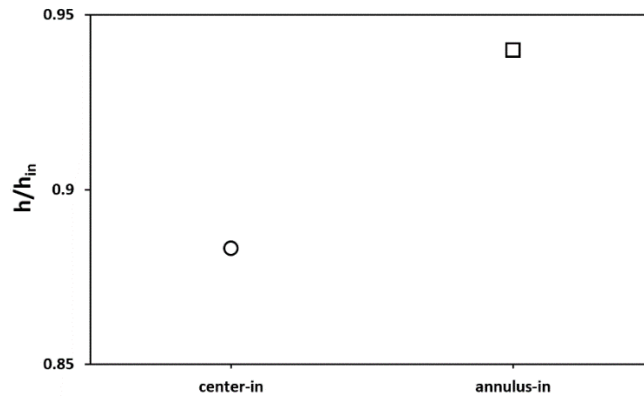


Fig. 3.10 Total heat transfer in the cases of center-in and annulus-in dimensionless by the inlet enthalpy

$$h = c_p \cdot \Delta T \quad (3.14)$$

where h is the enthalpy, c_p is the specific heat, and ΔT is the temperature difference

The local rate of heat transfer is presented in its normalized form on the end cap surface based on Eq. 3.15 as follows.

$$Nu = \frac{h_c}{k} D_h \quad (3.15)$$

where h_c is the convection coefficient, k is the thermal conductivity, and D_h is the hydraulic diameter.

The hydraulic diameter for the center-in flow will be the inner diameter of the center pipe and the hydraulic diameter of the concentric annulus-in flow determined by the subtraction of the inner diameter of the outer pipe (D_{io}) and the outer diameter of the inner pipe (D_{oi}) that is shown in Eq. 3.16 according to (Iry and Rafee 2019), (Morchio and Fossa 2019, and Gordon et al. 2017).

Concentric annulus:

$$D_h = \frac{4 \times A}{p} = \frac{4 \times (\pi/4) \times (D_{io}^2 - D_{oi}^2)}{\pi \times (D_{io} + D_{oi})} = D_{io} - D_{oi} \quad (3.16)$$

The results in Fig. 3.11-a show that the Nusselt number has some drops at some points for the center-in and annulus-in flows in the coaxial pipes with a flat end cap. The reasons for these drops are expected due to the onset and/or termination of streamline cells and the stagnation point which makes minimum friction on those spots (which will be discussed later in this study). Comparing the Nusselt number of both flow directions shows that the center-in flow is approximately 2.4 times larger than the annulus-in flow on the bucket space surface at the bottom of the borehole. In Fig. 3.11-b, however, the Nusselt number on the outer pipe surface shows that unlike the end cap, the Nusselt number of the annulus-in flow is on average about 2.5 times larger than the center-in flow. But the average Nusselt number of the pipe surface shows that the Nusselt number of the center-in flow is still larger than the annulus-in flow (1.2 times larger).

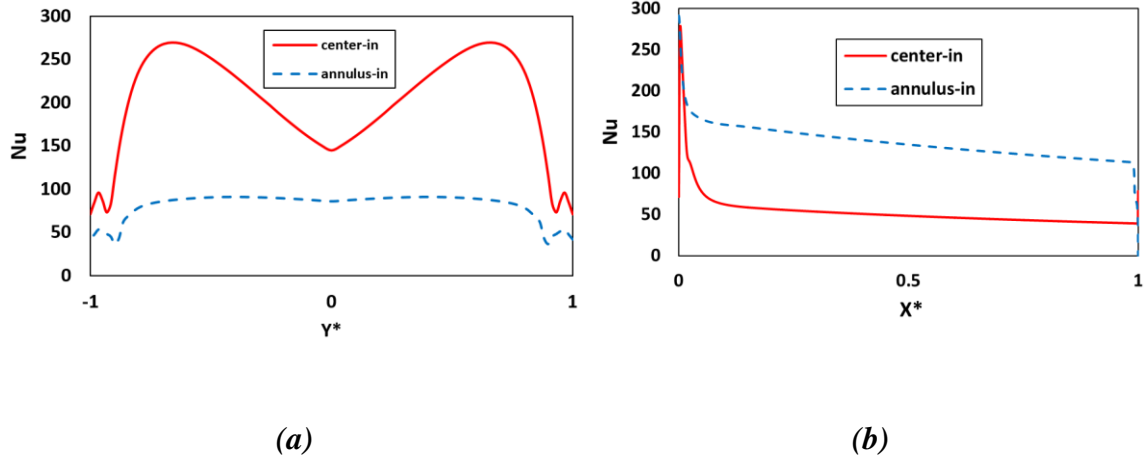


Fig. 3.11 Nusselt number of the center-in and annulus-in flow (a) on the flat-end cap ($Y^* = Y/D_{io}$) and (b) along the pipe ($X^* = X / X_{max}$)

Friction

The uniform distribution of shear rates on pipe walls in the upstream is disturbed as the fluid runs into the return space. The consequence can be observed in Fig. 3.12 where there is a symmetrical distribution of wall friction on the caps regardless of the flow direction. The minimum value of friction coefficient occurs on the end cap wall center due to the symmetry of flow motion, the stagnation point, and the separation that happen at the mid-point. The two other minimum points shown in Fig. 3.12, are also due to the separation and an onset of streamlines rotation that is demonstrated in the streamlines figure (see Fig. 3.14). The largest shear rate values occur on end cap when the flow is introduced from the inner pipe, however, in the vicinity of the cap center, friction coefficient values are in the same range as annulus-in flow. The authoritative studies indicate that the Nusselt number and the coefficient of friction have a direct relation which satisfies the comparison between the friction and Nusselt number of this study.

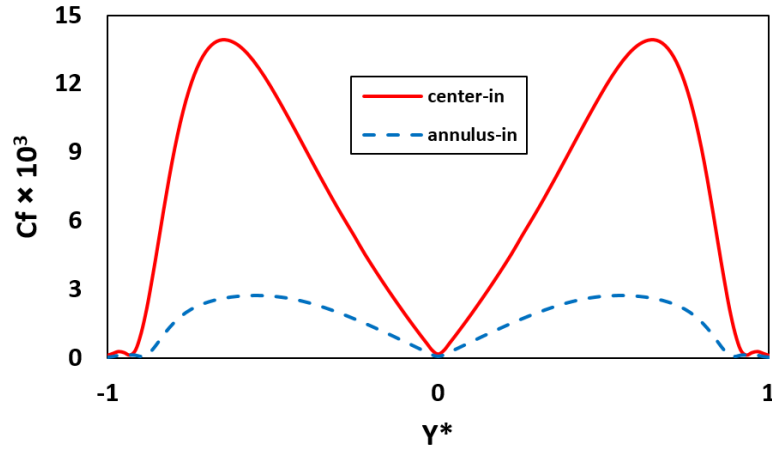


Fig. 3.12 Friction coefficient of center-in and annulus-in flows on the end cap surface ($Y^* = Y/D_{io}$)

Velocity, vorticity, and turbulent kinetic energy

As shown in Fig. 3.13-a, the fully developed turbulent flow travels within the center pipe. The velocity peak of the fully developed turbulent flow starts to diminish in the bucket space under the effect of the pressure and separation that occurs on the end cap surface from the bucket shaped space at the bottom of CBHE, making a concave velocity profile near the end cap surface. The enhancement of the fluid velocity occurs on the outer wall, so the flow with the maximum momentum shifts toward the outer pipe wall in the entrance region of the annulus. Bearing the temporary velocity peak on the sides near the outer pipe wall which is due to the pressure gradient (explained earlier in Fig. 3.6), the flow turns toward the annulus entrance resulting in a pressure drop and a large turbulent kinetic energy that is due to the expansion of flow through the annulus (see Fig. 3.14-a, and Fig. 3.16-a). The boundary layer separation of flow along with the pressure gradient induces the rotating recirculation which results in the generation of a ring of streamlines that is observed in Fig. 3.14-a, and the vorticity in Fig. 3.15-a.

Fig. 3.13-b shows the velocity distribution contour of the annulus-in flow at the bottom of the CBHE. It is observed that when the flow passes through the concentric annulus, the flow in the upstream and in the vicinity of the inner pipe wall takes a larger momentum due to the large pressure gradient as per Fig. 3.6-b that occurs at the edge of

the inner pipe and the pressure drop as the flow expands into the bucket-shaped space and turns towards the inner pipe. The edge of the inner pipe causes a separation of boundary layer. This recirculation towards the inside of the inner pipe wall turns into some obvious defined streamlines (see Fig. 3.14-b) and a large turbulent kinetic energy as per Fig. 3.16-b on the inside of the center pipe entrance. The vortices generation constrains the incoming flow, from the annulus to the inner pipe, which along with the large pressure of in the bucket-space bring about the maximum flow momentum inside the entrance of the center pipe. Also, the fluid viscosity and no-slip boundary conditions on the walls along with the flow turn, generate another ring of streamlines at the bottom of the bucket-shaped space.

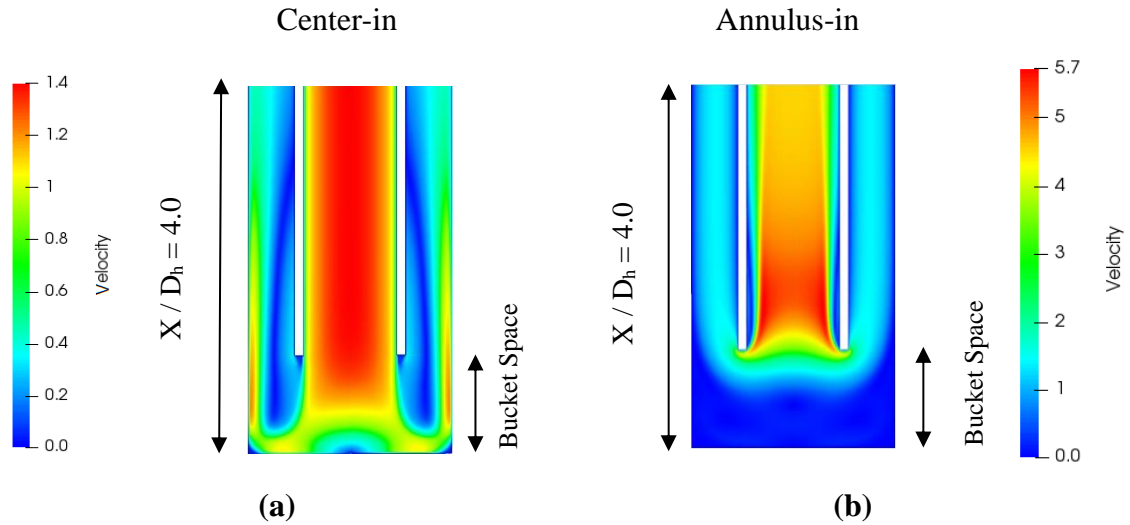


Fig. 3.13 Velocity distribution of center-in and annulus-in flow directions at the bottom of the coaxial pipes with flat-end and curved-end caps.

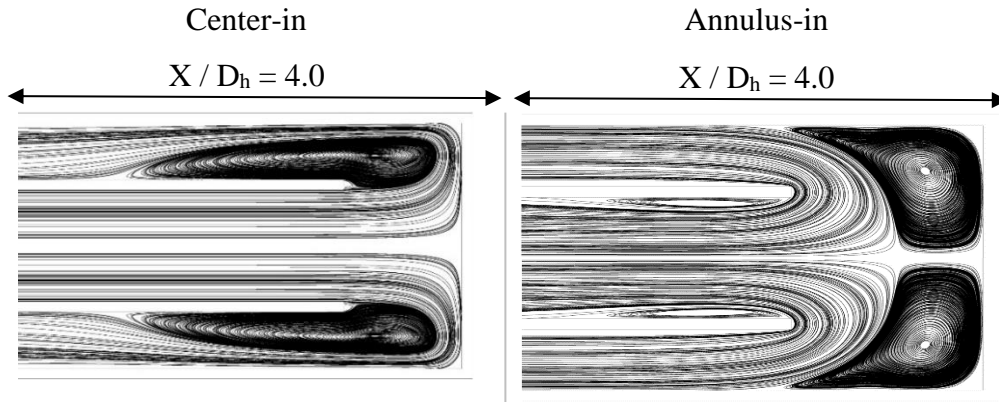


Fig. 3.14 Flow streamlines at the bottom of the coaxial BHEs for flat end caps in center-in and annulus-in flow directions

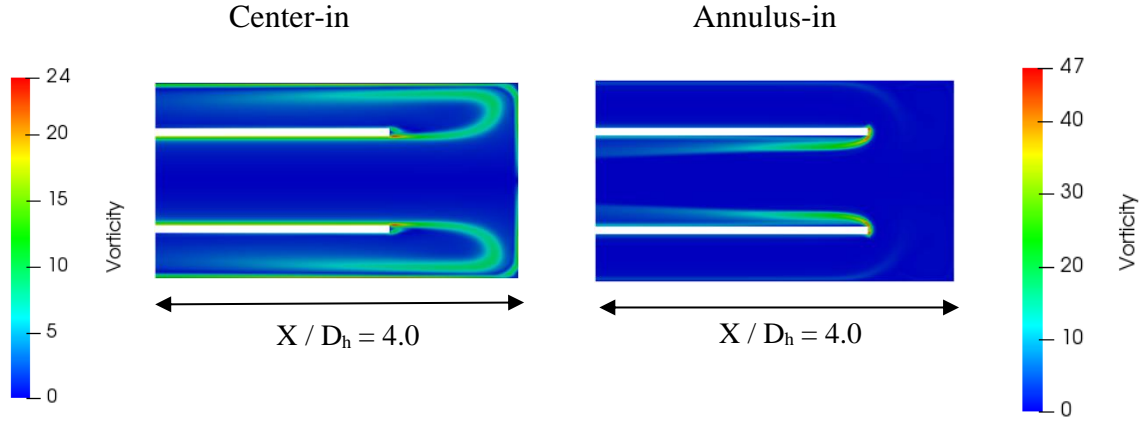


Fig. 3.15 Normalized vorticity contours of center-in and annulus-in flow directions

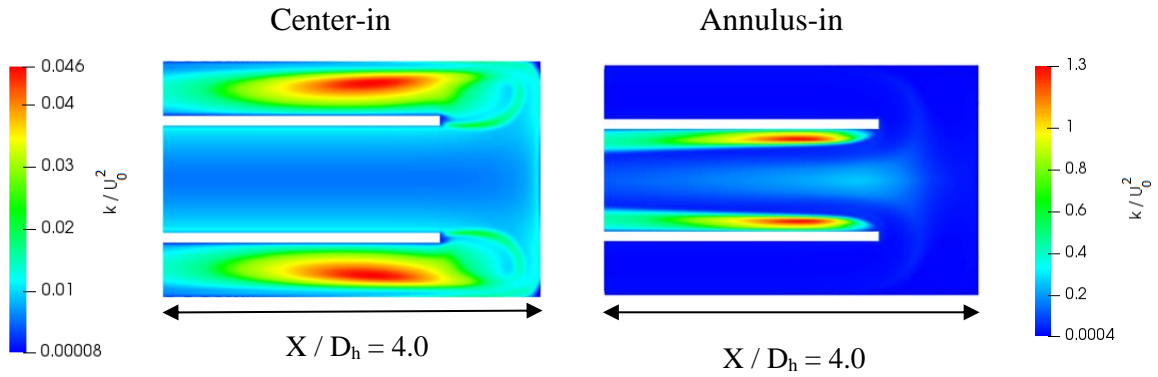


Fig. 3.16 Turbulent kinetic energy distribution contours of center-in and annulus-in flow directions

3.4.2 Bucket space length

It would be interesting to see to what extent the bucket space length, the gap between the inner pipe and the end of the outer pipe, provides the best performance possible. As such, three bucket space lengths have been selected to observe how much the flow and heat transfer are impacted. The location of the bucket space at the bottom of the coaxial pipes is shown in Fig. 3.17, and the bucket space lengths of $X / D_h = 0.6$, 1.0 , and 1.6 are selected. The results show that the bucket space length of $X / D_h = 1.0$, has the minimum total pressure loss. Hence, any change in the bucket space length (a longer or a shorter bucket space length) increases the total pressure loss of the system. It also enhances the total heat transfer which makes it important to consider a balance between the pressure drop and heat transfer due to the change bucket space length.

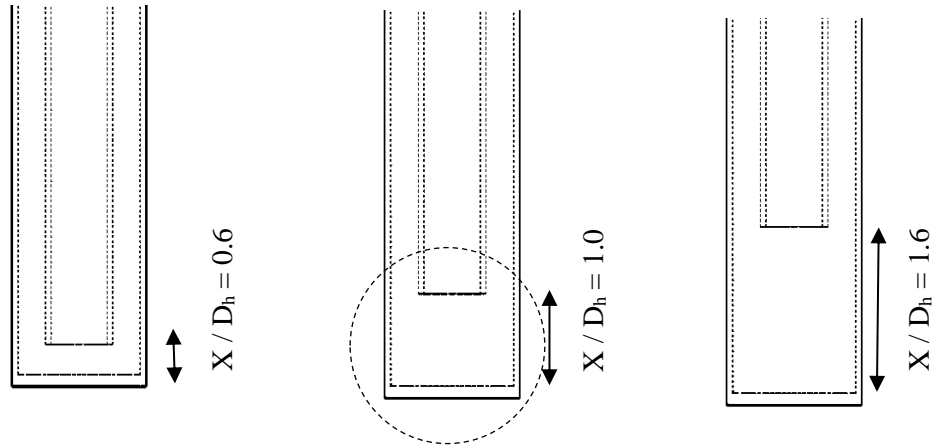


Fig. 3.17 Schematic diagram of the inner pipe in relation to the bottom of the CBHE (bucket space)

Therefore, the bucket space length of $X / D_h = 1$ is found to be the most efficient among other simulated cases. This means that the position of center pipe in relation with the end cap must be taken into account

One important factor to consider the efficiency of a borehole heat exchanger would be the total pressure loss that directly impacts the required pumping power. The measures for the selection of a proper heat exchanger are to overcome the total pressure losses associated with the borehole length as well as the pressure drops that every single flow passage causes. As it is shown in Fig. 3.18, it can be inferred that the total pressure loss decreases when the bucket space length decreases up to a length which provides the least total pressure loss and thus the least pumping power. From this point, if the length of the bucket space is shortened, the total pressure losses increase which results in the enhancement of the required pumping power. Considering the losses in the center pipe, bucket space and the annulus region at equal test and boundary conditions, the system with the bucket space length of $X / D_h = 1$ requires the least pumping power in the inlet at equal flow rates based on Eq. 3.12. Meaning that there is a length that provides the minimum pumping power. As a result, further increase or decrease of the bucket space length enhances the pressure drop and subsequently the pumping power. So the position of the center pipe in relation with the end cap must be taken into account so as to minimize the

total pressure loss. However, a balance between the improved heat transfer and the reduction of total pressure losses needs to be taken into consideration so as to minimize the total pressure losses which is going to be discussed later in this study.

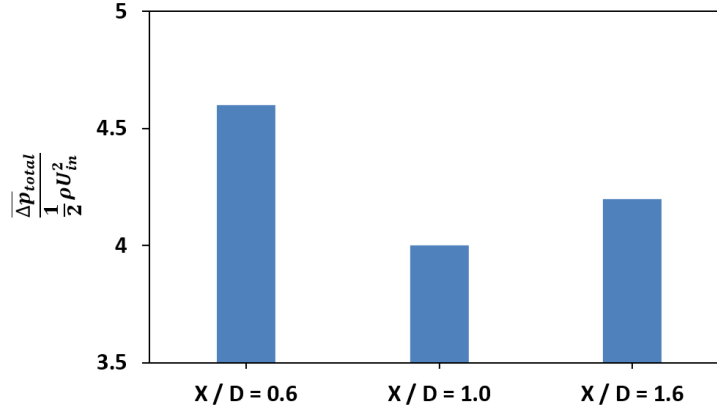


Fig. 3.18 Dimensionless total pressure loss in the coaxial system based on change in the bucket space length.

One consequence of the inner pipe displacement would be on the wall friction coefficient. No significant change was observed except the spots where the flow return occurs on the end cap wall. In those spots, the fluid through the shortest bucket space ($X/D_h = 0.6$) bears the most friction. After this, the most friction belongs to the longest bucket space ($X/D_h = 1.6$), meaning that there is not a direct relation between the wall friction and the inner pipe length because the least wall friction occurs when the inner pipe length in relation to the bottom of the borehole is $X/D_h = 1.0$ (see Fig. 3.19)

It is clear that the spots where the fluid returns or where there is a boundary layer separation, indicate the formation of vortices, from where the friction drops to the minimum value possible. The equal trend of the friction has a direct relation with the wall heat transfer demonstrated in its dimensionless form of Nusselt number shown in Fig. 3.20. However, unlike the wall friction, and Nusselt number, the pressure has an opposite impact on the pipe wall, meaning that the pressure enhancement at one spot reduces increases the velocity which leads to the increase of the heat transfer on that region, and where there is a heat transfer increase, indicates higher velocity as a result of pressure reduction (see Fig. 3.21). In the studied cases, if selecting the bucket space length of $X/D_h = 0.6$ instead of

$X/D_h = 1.0$, 4.2% improvement of Nusselt number is achieved at the cost of 15% of total pressure loss at the bottom of borehole. The balance between the total heat transfer and the loss coefficient is particularly significant. As a result, installing the inner pipe's position in relation with the bottom of the borehole can create a balance between the improved heat transfer and reduction of total pressure losses.

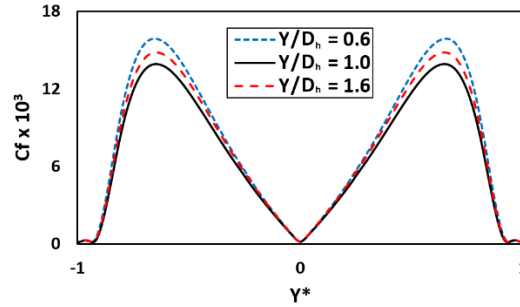


Fig. 3.19 Wall friction coefficient on the end cap surface ($Y^* = Y/D_{io}$) based on the change in the bucket space length

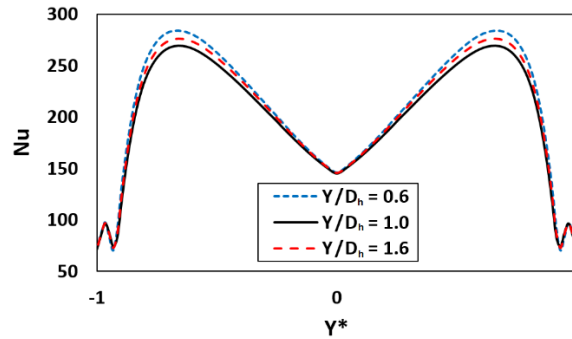


Fig. 3.20 Nusselt number against the end cap ($Y^* = Y/D_{io}$) based on the change in the bucket space length

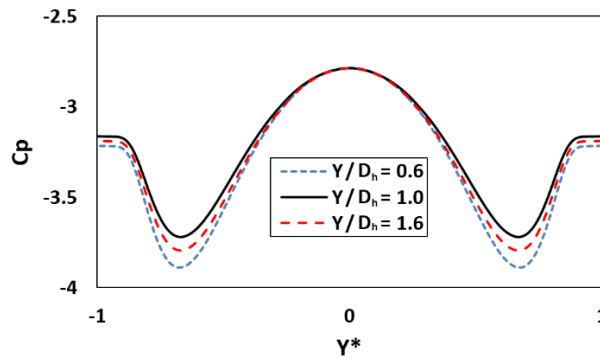


Fig. 3.21 Pressure coefficient on the end cap surface ($Y^* = Y/D_{io}$) based on the change in the bucket space length

3.4.3 Reynolds number effects

Having studied the incoming flow direction and the bucket space length, there is room to see how the fluid behaves in flows with different Reynolds numbers. Three Reynolds numbers have been selected to carry out this study. One is the Reynolds number of the experimental study by (Gordon et al. 2018) ($Re \approx 2 \times 10^3$), one is the Reynolds number by which the above study was performed ($Re \approx 2 \times 10^4$), and one Reynolds number in between ($Re \approx 10^4$). The reason for selecting these Reynolds numbers with a considerable difference is to find the overall trend of flow and heat transfer due to the change in the inlet velocity of flow when using different pumping systems with different pumping powers. The findings regarding the increase of Reynolds number indicate that there is a growth in heat transfer when increasing the Reynolds number at a cost of a larger total pressure loss and that no significant improvement of heat transfer occurs at excessive Reynolds number enhancement.

The heat transfer results show that the heat flux and the total enthalpy increases with an increase of Reynolds number (see Fig. 3.22-a and Fig. 3.23-a). It would seem that further increase of Reynolds number decreases the rate of heat transfer augmentation. Also the gradient of heat transfer in the outer pipe decreases when there is an increase in the Reynolds number of flow. Meaning that there is a Reynolds number from which further increase of Reynolds number does not alter the heat flux and enthalpy. In Fig. 3.22-b and Fig. 3.23-b, however, achieving that specific Reynolds number happens sooner than the pipe along the annulus.

The reduction of the heat exchange rate with the Reynolds number augmentation is still increasing the flow rate and pressure, thus, the pumping power increases continuously. To avoid excessive pumping power for little betterment of heat transfer in the CBHE system, achieving to an optimal Reynolds number which brings about a better resident time for heat transfer provides information on the best possible pumping power and heat pump selection.

Meanwhile, the increase of Nusselt number based on the Reynolds number increment shows that Reynolds number impacts the growth of convective heat transfer

coefficient prominently on both the end cap and the annulus walls, and makes a negative gradient of Nusselt number along the annulus which grows in magnitude (Fig. 3.24).

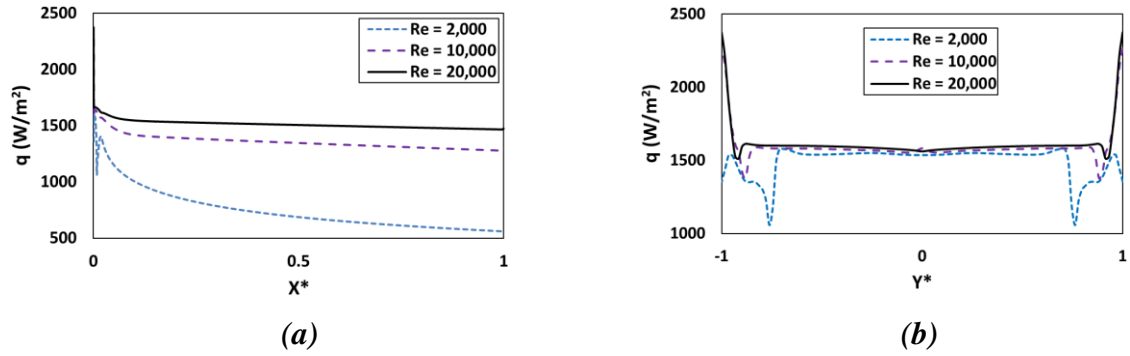


Fig. 3.22 Heat flux along (a) the annulus wall and (b) end cap surface ($Y^* = Y/D_{i0}$)

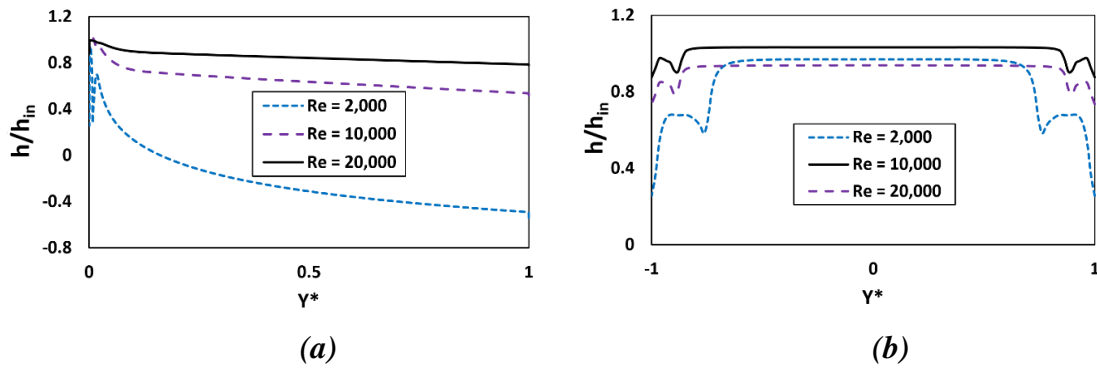


Fig. 3.23 enthalpy (a) along the pipe ($X^* = X / X_{max}$) and (b) end cap surface ($Y^* = Y / D_{i0}$)

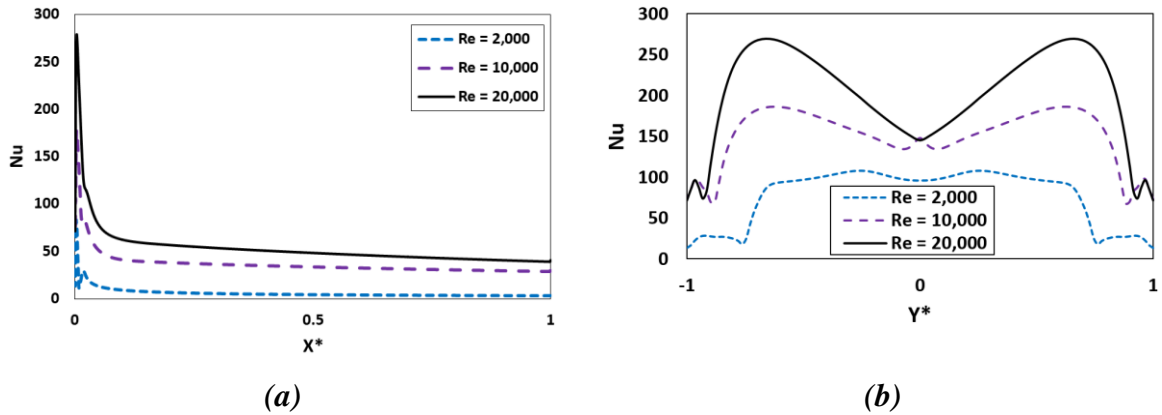


Fig. 3.24 Nusselt number along (a) the annulus wall and (b) end cap surface ($Y^* = Y/D_{i0}$)

The friction that happens on the end cap surface shows that the Reynolds number of the flow has a counter impact on friction coefficients. Therefore, as the Reynolds number of flow increases, the shear rate effects become less severe (Fig. 3.25-a). This phenomenon is noticeable, particularly, when the flow is to return in the vicinity of the center of the end cap surface (Fig. 3.25-b). In the annulus region, however, except the initial distances which is magnified in Fig. 3.25-a, the flow makes a uniform friction on the fluid-pipe wall with larger magnitudes compared to the friction on the end cap surface.

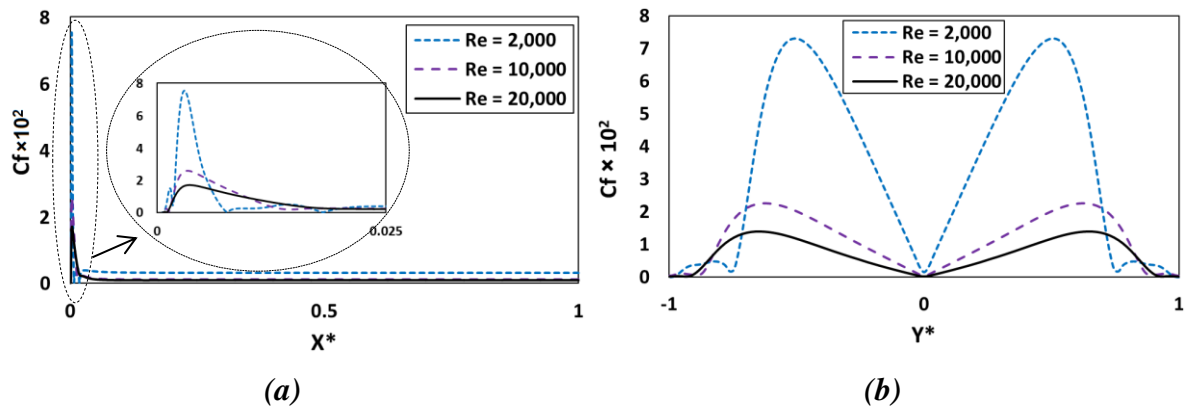


Fig. 3.25 Friction coefficient along (a) the annulus wall and (b) the end cap surface

While comparing the pressure coefficient of the three simulated flows in the annulus region, it was found that the largest pressure on the end cap occurs when the Reynolds number of the flow is 2×10^3 . In the annulus region, also, the pressure coefficient of the three flows drops until the exit port (Fig. 3.26). However, when the Reynolds number increases, the total pressure loss decreases. Also, Fig. 3.27 demonstrates the pressure drop of the inner pipe and the outer pipe of all the simulated flows in one glance. The results show that the pressure drop in the inner pipe is larger than the pressure drop in the outer pipe (annulus region), and this amount of pressure drop decreases when increasing the Reynolds number. There is a dramatic difference between the pressure drop of the inner pipe and the annulus region when there is a lower Reynolds number. And this pressure difference decreases as the Reynolds number of flow increases. This can also be observed in the total pressure loss of the system based on Fig. 3.28 that includes the inner pipe, outer pipe, and the bucket space.

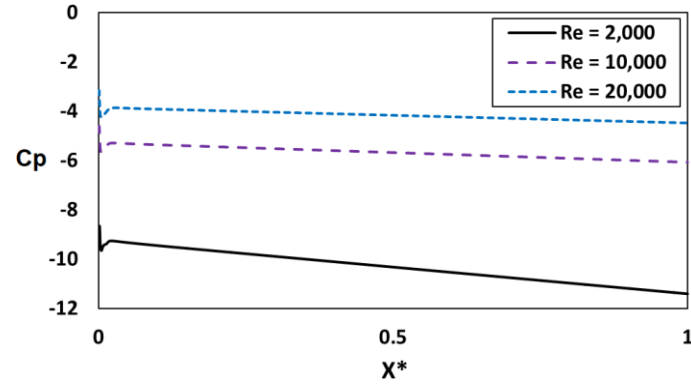


Fig. 3.26 Pressure coefficient of three Reynolds numbers against the wall ($X^* = \frac{L}{D_h}$) along the annulus

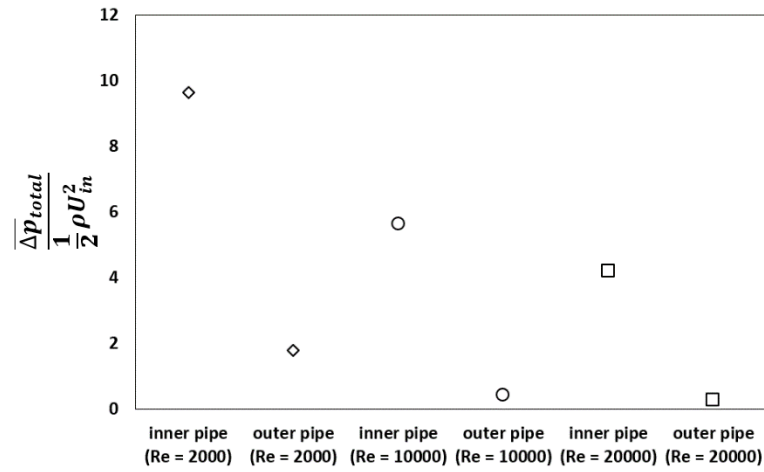


Fig. 3.27 Pressure drop coefficient in the inner pipes and the outer pipes considering three Reynolds numbers.

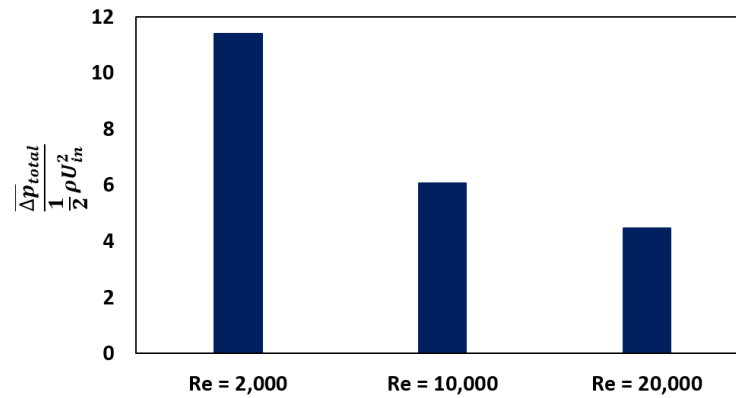


Fig. 3.28 Total pressure loss of the system considering three Reynolds numbers

3.5 Conclusions

Comparing the center-in and annulus-in flows at $Re = 2 \times 10^4$ shows that the center-in flow has a better performance in terms of total pressure loss in the system, although the total heat transfer of the annulus-in flow is about 5.7% better.

A short and a long bucket space need a large pumping power. Also, an improvement of heat transfer is achieved for a short bucket space at the cost of a high total pressure loss in the system. So there is a length that provides the minimum pumping pressure, meaning that installing the center pipe in a position that causes the least total pressure loss needs to be taken into account. In the studied cases, we could reduce the total pressure loss by 15% via changing the inner pipe length, however, this is achieved with about 4% of the total heat transfer reduction.

Since the increment of Reynolds number increases the total pressure loss of the system and reduces the total heat transfer, a balance between the harvested or rejected heat and the cost of a large pumping pressure need to be made, because no significant improvement of heat transfer happens when there is excessive increase of Reynolds number. There is a Reynolds number that provides the best heat transfer on the fluid-pipe interface. The knowledge about the best Reynolds number of the flow in the CBHE may contribute to selecting a proper pumping system and cut the costs associated with it.

Nusselt number increases on the pipe-fluid interface along the annulus when increasing the Reynolds number. Considering the wall flux parameters including the convective heat transfer and the wall shear rates, it can be inferred that there is a Reynolds number from which the surface heat flux and the wall frictions are not affected by the further increase of Reynolds number. Excessive increase of Reynolds number reduces the pressure drop in the inner pipe and the annulus, however, this happens at the cost of a large pumping power and no significant improvement of total heat transfer. As a result, a Reynolds number that brings about a reasonable heat transfer and a small pressure drop must be selected.

3.6 References

- Cvetkovski, C. G., S. Reitsma, T. Bolisetti, and D. S.-K. Ting. 2014. "Ground Source Heat Pumps: Should We Use Single U-Bend or Coaxial Ground Exchanger Loops?" *International Journal of Environmental Studies* 71(6): 828–39.
- Gordon, D., T. Bolisetti, D. S.-K. Ting, and S. Reitsma. 2018. "Experimental and Analytical Investigation on Pipe Sizes for a Coaxial Borehole Heat Exchanger." *Renewable Energy* 115: 946–53.
- Iry, S., and R. Rafee. 2019. "Transient Numerical Simulation of the Coaxial Borehole Heat Exchanger with the Different Diameters Ratio." *Geothermics* 77: 158–65.
- Li, C., Y. Guan, R. Yang, X. Lu, W. Xiong, A. Long. 2020. "Effect of Inner Pipe Type on the Heat Transfer Performance of Deep-Buried Coaxial Double-Pipe Heat Exchangers." *Renewable Energy* 145: 1049–60.
- Pan, A., L. Lu, P. Cui, and J. Jia. 2019. "A New Analytical Heat Transfer Model for Deep Borehole Heat Exchangers with Coaxial Tubes." *International Journal of Heat and Mass Transfer* 141: 1056–65.
- Song, X., R. Zheng, G. Li, Y. Shi, G. Wang, J. Li. 2018. "Heat Extraction Performance of a Downhole Coaxial Heat Exchanger Geothermal System by Considering Fluid Flow in the Reservoir." *Geothermics* 76: 190–200.
- Song, X., G. Wang, Y. Shi, R. Li, Z. Xu, R. Zheng, Y. Wang, J. Li. 2018. "Numerical Analysis of Heat Extraction Performance of a Deep Coaxial Borehole Heat Exchanger Geothermal System." *Energy* 164: 1298–1310.
- "Wedge." SimScale. <https://www.simscale.com/docs/simulation-setup/boundary-conditions/wedge/> (December 22, 2019).
- Yekoladio, P. J., T. Bello-Ochende, and J. P. Meyer. 2013. "Design and Optimization of a Downhole Coaxial Heat Exchanger for an Enhanced Geothermal System (EGS)." *Renewable Energy* 55: 128–37.
- Zanchini, E., S. Lazzari, and A. Priarone, 2010. "Improving the Thermal Performance of Coaxial Borehole Heat Exchangers." *Energy* 35(2): 657–66.
- Van der Zwaan, B., and F. Dalla Longa. 2019. "Integrated Assessment Projections for Global Geothermal Energy Use." *Geothermics* 82: 203–11.

CHAPTER 4 – Conclusions and Future Work

4.1 U-bend borehole heat exchangers:

Curvature ratio effects:

- For the flow at $Re = 600$, however, the increase of the bend curvature ratio results in a consistent decrease of total pressure losses. This means that the increase of curvature ratio reduces the amount of total pressure loss to a certain point.
- At $Re = 6 \times 10^4$, there is a Dean number from which further increase or decrease of the curvature ratio, increases the total pressure loss. As a result, the curvature ratio must be focused when designing a U-bend system.
- The flow at a low Reynolds number has a better total heat transfer due to a higher residence time. However, this betterment of heat transfer happens at the cost of a high total pressure loss. Also, selecting the right bend curvature can contribute to improving the performance of the U-bend system.

Reynolds number and U-bend length:

- The increase of Reynold number decreases the outlet temperature. Also, at high Reynolds number, the outlet temperature takes less effect from the Reynolds number augmentation.
- In the heating mode of operation, the increase in the U-bend length increases the temperature in the outlet of the U-bend system as well as the amount of heat that is extracted. However, the outlet temperature is decreased when increasing the Reynolds number and that results in the enhancement of the heating rate.

4.2 Coaxial borehole heat exchanger

- Comparing the center-in and annulus-in flows at $Re = 2 \times 10^4$ shows that the center-in flow demonstrates a better performance in terms of total pressure loss in the system, although the total heat transfer of the annulus-in flow is about 5.7% better.
- A short and a long bucket space require a large pumping power due to the increase of pressure drop, and no significant improvement of heat transfer is achieved as a result of change in the bucket space length. Hence, there is a length that provides the most efficient pumping power.
- Nusselt number increases on the pipe-fluid interface along the annulus with the increase of Reynolds number. Also, it can be inferred that there is a Reynolds number from which the surface wall heat flux and the total heat transfer are not affected by the further the increase of Reynolds number of the flow.
- Since the increment of Reynolds number reduces the total pressure loss of the system and increases the total heat transfer, a balance between the harvested or rejected heat at the cost of a large pumping pressure need to be made.

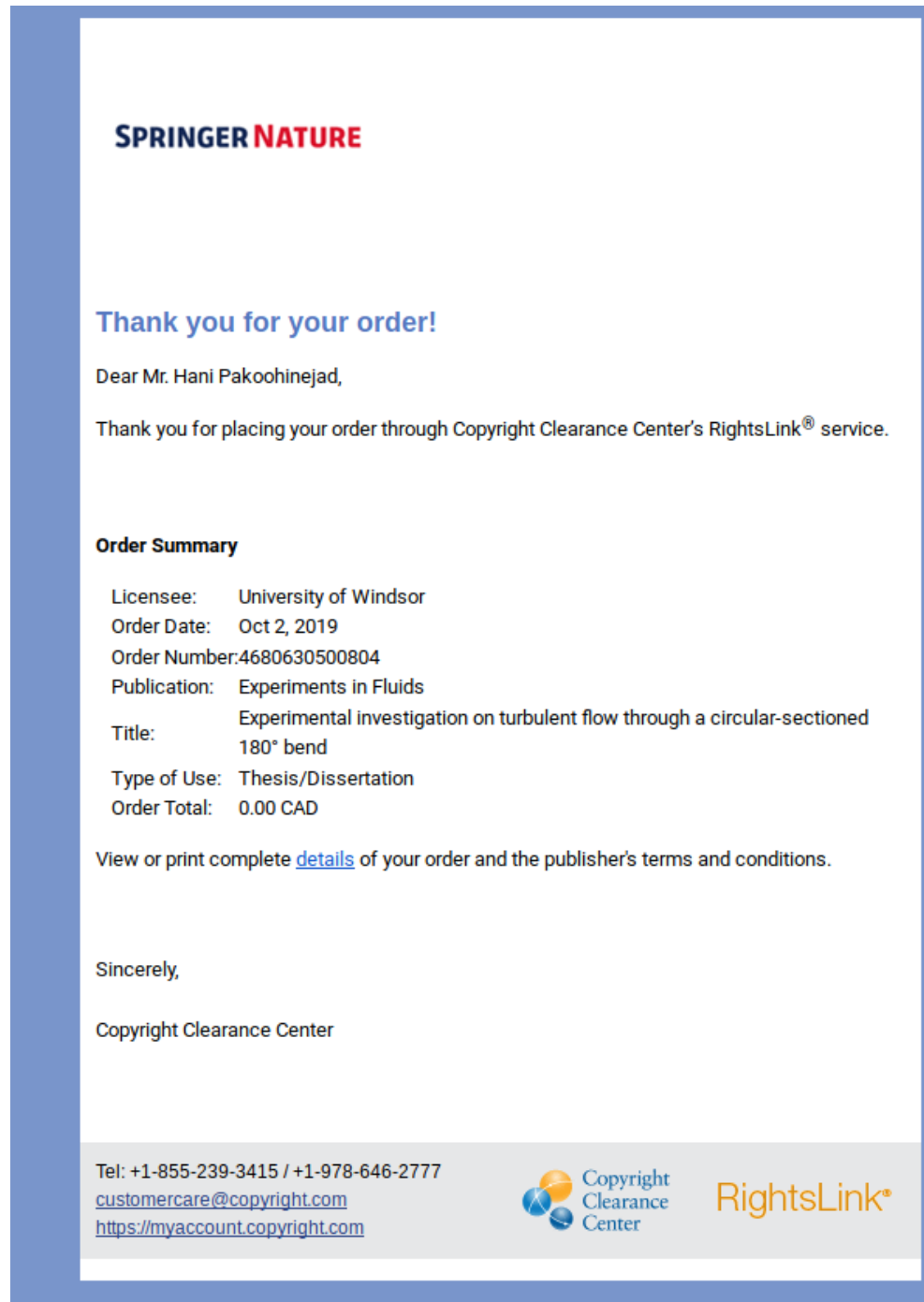
4.3 Future Work

- A study delving into increasing the outlet temperature at a reduced pipe length
- A numerical study on a deep U-bend and coaxial borehole heat exchanger
- A Comparative study between the U-bend and coaxial borehole heat exchangers

APPENDICES

Appendix A

Reprinting with Permission for validating my numerical simulation in chapter 2 of this thesis.



VITA AUCTORIS

NAME: Hani Pakoohinejad

PLACE OF BIRTH: Bandarabbas, Iran

YEAR OF BIRTH: 1990

EDUCATION: Shahid Nematih High School, Karaj, Iran, 2008

Azad University, B.A.Sc., Tehran, Iran, 2013

University of Windsor, M.A.Sc., Windsor, ON, 2020